



**Microturbine Turbojets: Experimental
Evaluation of Commercially Available Engines**

THESIS

Richard A. DePaola III, 2d Lt, USAF
AFIT/DS/ENY/20-M-259

**DEPARTMENT OF THE AIR FORCE
AIR UNIVERSITY**

AIR FORCE INSTITUTE OF TECHNOLOGY

Wright-Patterson Air Force Base, Ohio

DISTRIBUTION STATEMENT A
APPROVED FOR PUBLIC RELEASE; DISTRIBUTION UNLIMITED.

The views expressed in this document are those of the author and do not reflect the official policy or position of the United States Air Force, the United States Department of Defense or the United States Government. This material is declared a work of the U.S. Government and is not subject to copyright protection in the United States.

AFIT/DS/ENY/20-M-259

MICROTURBINE TURBOJETS: EXPERIMENTAL EVALUATION OF
COMMERCIALY AVAILABLE ENGINES

THESIS

Presented to the Faculty
Department of Aeronautics and Astronautics
Graduate School of Engineering and Management
Air Force Institute of Technology
Air University
Air Education and Training Command
in Partial Fulfillment of the Requirements for the
Degree of Master of Science in Aeronautical Engineering

Richard A. DePaola III, B.S.

2d Lt, USAF

March 2020

DISTRIBUTION STATEMENT A
APPROVED FOR PUBLIC RELEASE; DISTRIBUTION UNLIMITED.

AFIT/DS/ENY/20-M-259

MICROTURBINE TURBOJETS: EXPERIMENTAL EVALUATION OF
COMMERCIALY AVAILABLE ENGINES

Richard A. DePaola III, B.S.
2d Lt, USAF

Committee Membership:

Fred R. Schauer, PhD
Chair

Marc D. Polanka, PhD
Member

Brian T. Bohan, PhD
Member

ADEDJI B. BADIRU, PhD
Dean, Graduate School of Engineering and Management

Table of Contents

	Page
Abstract	vi
Acknowledgements	vii
List of Figures	viii
List of Tables	xvi
I. Introduction	1
1.1 Research Motivation	1
1.2 Microturbine Technology	3
1.3 Research Objectives	4
1.3.1 Primary Research Objective	4
1.3.2 Supplemental Research Objective: #1	5
1.3.3 Supplemental Research Objective: #2	6
II. Literature Review	7
2.1 Introduction	7
2.2 Brayton Cycle Turbojets	7
2.3 Inlet & Nozzle	10
2.4 Compressor	12
2.4.1 Centrifugal Compressor Velocity Triangles	18
2.4.2 Thermodynamics & the Euler Pump Equation	21
2.4.3 Rotor Backsweep	25
2.4.4 Calculation of Compressor Slip	27
2.4.5 Dimensionless Analysis	31
2.4.6 Specific Speed and Specific Diameter	39
2.4.7 Diffuser Performance	45
2.5 Combustor	50
2.5.1 Equivalence Ratio & Fuel Fraction	52
2.5.2 Thermal Distortion	53
2.6 Turbine	56
2.7 Engine Performance	59
2.8 Instrumentation	62
2.8.1 Thrust Stand Fundamentals	62
2.8.2 Temperature: Thermocouples	64
2.8.3 Thermocouple Corrections	68
2.8.4 Kiel Tube	71

	Page
III. Experimental Methodology	76
3.1 Published Engine Performance	76
3.2 Facility: AFRL's Small Engines Research Lab (SERL)	
Test Stand 5	81
3.3 Thrust Stands	83
3.3.1 Thrust Stand Calibration	89
3.4 Instrumentation	100
3.4.1 Data Acquisition System	101
3.4.2 Mass Air Flow Sensor	102
3.4.3 Internal Instrumentation: Temperature and	
Pressure	106
3.5 Uncertainty Analysis	111
IV. Results	113
4.1 Overall Performance	113
4.1.1 Thrust and Mass Air Flow	114
4.1.2 Fuel Consumption	123
4.2 Component Performance	127
4.2.1 Compressor	127
4.2.2 Combustor	134
4.2.3 Turbine	139
4.3 Performance Potential	146
4.4 Effects of Instrumentation on Engine Performance	153
4.5 Same-Make, Same-Model Engine Performance	
Variability	154
V. Conclusions	158
5.1 Primary Research Objectives	159
5.2 Supplemental Research Objectives	160
5.3 Future Work	161
5.4 Concluding Remarks	164
Bibliography	165

Abstract

The Air Force commonly finds itself employing expensive defensive systems against inexpensive weapons. In an effort to leverage industry to remedy this imbalance, commercially available microturbine turbojets have been identified as a potential alternative to special-order, military-grade systems. Compared to the status quo, commercially available engines have the potential to provide mission-capable systems at an order of magnitude reduction in cost.

This research provides an assessment of the performance currently available from commercial microturbine turbojets and represents the first industry-wide investigation into this class of engine by AFRL's SERL. Four commercial engines of the same thrust class were evaluated for overall and component-level performance. In addition to providing an evaluation of existing systems, the maximum potential performance for a commercial turbojet was predicted based on the component-level evaluations. This analysis indicated that a commercial turbojet could have comparable thrust performance to a similarly sized military-grade engine. Based on the components surveyed, it seems unlikely that commercial microturbine engines will be able to achieve the specific fuel consumption rates of military-grade engines without improvements to the compressors found in commercial turbojets.

To support the conclusions of this research, two supplemental research objectives regarding experimental methods were pursued: (1) an assessment of the effects of instrumentation on microturbine engine performance and (2) the quantification of performance variability in same-make, same-model engines. It was found that the instrumentation did not degrade engine performance and that engine performance could vary by 10% in same-make, same-model commercial microturbine turbojets.

Acknowledgements

First and foremost, I'd like to thank my family for their support throughout this program. I'd also like to thank the team down at ISSI for lending their experience and technical expertise, especially Brian Sell, Nicholas Grannan, and Kaitlyn Brendlinger. Time spent working with them was invaluable for the entire research effort. Thanks to my advisor, Fred Schauer, for providing an opportunity to explore experimental research with AFRL. My experiences at the labs will be surely be a unique experience for me through my Air Force career. Thanks to my committee for their advice and guidance, a resource of which I could never have had enough. Finally, thanks to the friends made at Wright-Patterson AFB. Your friendship will undoubtedly be the most valuable aspect of this experience.

Richard A. DePaola III

List of Figures

Figure		Page
1	Microturbine turbojet engines: (a) Hamilton Sundstrand TJ-50 used on the ADM-160 MALD, (b) commercially available, civilian engine.	2
2	Cutaway of a commercially available, microturbine turbojet.	3
3	Brayton Cycle overlaid with turbojet station numbering. The green line indicates the energy available for propulsion in the exhaust.	8
4	CT Scan of Engine B indicating locations of each engine component.	10
5	Nozzle intake streamlines at different flight conditions [24]	11
6	Relative boundary layer increase in a multi-stage axial compressor.	13
7	Illustration of tip losses on an axial compressor.....	14
8	Effects of relative tip clearance on compressor overall adiabatic efficiency. Appended from Ref.[32].	15
9	Effects of relative tip clearance on stage static pressure ratio. Appended from Ref.[32].	15
10	Meridional View of a Centrifugal Compressor [17].	17
11	Inducer velocity diagrams at the (a) hub and (b) tip. Note: although no swirl was depicted in this diagram, the same tendency occurs for the case of uniform swirl.	19
12	Velocity Triangle of Flow at the Inducer.	20
13	Velocity diagram of the flow exiting a centrifugal compressor.	20
14	Compressor pressure ratio curve divided into infinitesimal pressure gains for derivation of polytropic efficiency.	22

Figure	Page
15	Exponential dependency of compressor pressure ratio for the centrifugal compressor on tip speed. Assumes $\epsilon = 0.8$ 24
16	Compressor exit velocity triangles: (a) Radial rotors, (b) Backswept rotors. 25
17	Effects of Backsweep Angle on Compressor Pressure Ratio. 27
18	Empirical Slip Factor Results. Each Curve represents a unique backsweep angle, β . Each of the three graphs represents a distinct number of blades, Z [29]. 30
19	Compressor adiabatic efficiency decrement vs. Reynolds Number at compressor inlet [18]. 38
20	Balje Diagram showing the effect of variations in specific speed [7]. 40
21	Centrifugal compressor application in aircraft engine based on specific speed regimes [23] [35]. 40
22	Original Cordier Diagram relating specific speed and specific diameter to contours of empirically derived adiabatic efficiency [8] [12]. 42
23	General Cordier Diagram illustrating the peak efficiency line highlighting the N_s range appropriate for centrifugal compressors. Appended from [22]. 43
24	Experimental results from Rodgers's 1980 report showing the correlation between specific speed and impeller polytropic efficiency. Original Ref: [33]. Appended Ref: [43]. 44
25	Station Numbering used for compressor analysis overlaid on: (a) engine CT scan, (b) photograph of diffuser. Both images are of Engine D. Station Numbering from [18]. 45

Figure	Page
26	Empirical Static Pressure Recovery Coefficients taken in an applied setting (i.e. within an engine) compared to data from a highly instrumented lab setting. Illustrates high degree of uncertainty associated with diffuser measurements [11]. 47
27	Vaneless Diffusers: (a) Constant Width, (b) Pinched. 48
28	Vaned Diffusers: (a) Channel or Wedge, (b) Airfoil. 49
29	Illustration of air partitioning in an annular, microturbine combustor. Adapted from Gieras and Stańkowski [13]. 50
30	Streamlines through the combustor with color contours of velocity magnitude indicating flame-holding region. Adapted from Gieras and Stańkowski [13]. 51
31	Axial view of a cross section of the flow within the combustor showing radial thermal distortion. Adapted from Gieras and Stańkowski [13]. 54
32	Turbine adiabatic efficiency related to specific speed and specific diameter [2]. Solid lines indicate maximum possible efficiency. Dashed lines indicate average efficiency. 58
33	Turbine Rotors (a) Airfoil Nomenclature, (b) Strength-to-weight ratio vs. temperature for typical turbine materials. Materials: (1) Al alloy, (2) Ti alloy, (3) Wrought Ni alloy, (4) High-strength Ni alloy, (5) Single-crystal superalloy. Ref: [25]. 59
34	Thrust per frontal area for military-grade expendable turbojets [16]. Published by Hamilton Sundstrand after releasing their TJ-50 for the ADM-160 MALD. 60
35	Carpet Plot showing turbojet design space. 61
36	Typical thermocouple junction configurations [30]. 65
37	Thermocouple response time for variations in junction type and size. Measurements made in water [31]. 67
38	Six sources of heat transfer along a thermocouple. [48] 69

Figure	Page
39	Thermal distortion sensitivity to number and location of probes [10]. 71
40	G. Kiel’s propped “total-head meter” [19]. 73
41	Modern Kiel Tube. 73
42	Kiel Tube Thermocouple [4]. 73
43	Flowpath through a standard, axial-flow turbojet. Flowpath overlaid on a CT scan of Engine B. 78
44	CT scans of Engines A and C, both standard, axial-flow turbojets. 78
45	Flowpath through a reverse-flow turbojet. Flowpath overlaid on a CT scan of Engine D. 79
46	Microturbine turbojet turbines: (a) Axial turbine from Engine B, (b) Radial turbine from Engine D. 80
47	SERL’s 5-Stand Floor Plan 82
48	Photograph of the control room identifying equipment needed during testing. 84
49	Pre-existing, air-bearing thrust stand. 85
50	Air-bearings used to support pre-existing thrust stand. 85
51	Installation of new, flexure-based thrust stand. 86
52	Flexure Thrust Stand Side View: (a) Photograph, (b) Same view with annotations. 87
53	Close-up of the load cell connection between the floating frame and base. 88
54	Correction of air-bearing thrust stand calibration issues: (a) pre-existing calibration setup, (b) corrected calibration setup. 91
55	Proper calibration process for the air-bearing thrust stand. (These diagrams will be appropriately colored later) 92

Figure	Page
56	Calibration results for the air-bearing thrust stand..... 93
57	Uncertainty development. Error given in (a) lbs and (b) % of applied load. 93
58	Calibration setup for flexure-based thrust stand: side-view..... 94
59	Alignment of linear actuator with thrust axis: (a) establishment of thrust axis and offset, (b) use of plumb to align linear actuator with thrust axis. 96
60	Flexure-based thrust stand calibration load cell connection alignment: (a) side-view of attachment, (b) vertical alignment of load cell connection with engine mount. 96
61	Vertical alignment of load cell using washer to shim connection between load cell and engine mount..... 97
62	Raw Data used to Calibrate Flexure Thrust Stand..... 98
63	Raw Data used to Calibrate Flexure Thrust Stand..... 99
64	Quantification of uncertainty due to hysteresis. 100
65	DAQ. 102
66	MAF connected to Engine B using additively manufactured adapter. 103
67	(a) 3" Slot Style Pro-Tube MAF by Pro-M Racing, (b) Pro-M 92 High Performance MAF with Inlet and Flow Straightener 104
68	Calibration Data from MAF manufacturer overlaid with trendline. Trendline is based only on data that lies within the bounds of engine performance. 105
69	Error of MAF Calibration Curve against Calibration Data presented as: (a) Percentage of the Manufacturer's calibration mass flow rate and (b) mass flowrate (kg/s)..... 105
70	Instrumentation diagram overlaid on CT scan of Engine B. Thermal profile of turbine inlet conditions is appended from Ref. [13] 107

Figure	Page
71	Thermocouple positioned in front of NGV, illustrating relatively large size of the thermocouple to the passage size. 109
72	Pitot Tube and Thermocouple at nozzle exit plane. 110
73	Measured corrected thrust compared to the manufacturer's published performance data. 115
74	Frontal Area (Engine D) 119
75	Thrust Per Frontal Area. Data from the four engines tested is overlaid on early 2000's state of the art microturbine turbojets. Appended from [16] 119
76	Experimental results for corrected thrust and corrected mass air flow for all four engines. 121
77	Specific thrust for all four engines. 121
78	Overall engine efficiency based on jet power. H.S. TJ-50 calculations based on data from Ref. [16]. 122
79	Measured corrected fuel consumption compared to published data. 124
80	Corrected fuel consumption for all four engines. 125
81	Experimental results for corrected specific fuel consumption for all four engines: (a) full operating range, (b) near design point. 126
82	Original Cordier Diagram overlaid with measured compressor performance from each engine [8]. 129
83	Compressor polytropic efficiency with annotations indicating diffuser type. 130
84	Compressor Overall Pressure Ratio with annotations indicating number of blades (including splitters). 132
85	Prediction of diffuser pressure drop via empirical slip factor correlation. 133
86	Stability of thermocouple measurements at turbine inlet. 135

Figure	Page
87	Uncertainty of thermocouple measurements at turbine inlet: (a) error bars indicate thermocouple accuracy, (b) error bars indicate 2 standard deviations of the five second data sample average to determine temperature at each engine speed. 136
88	Turbine Inlet Temperature for Engine B measured over multiple experimental tests at same probe location. 137
89	Turbine Inlet Temperature for Engine C measured over at two probe locations simultaneously. 138
90	Turbine flow maps indicating choked nozzle guide vanes. 139
91	Relationship between corrected mass flow rate and choked turbine 141
92	Relationship between mass flow rate and corrected mass flow rate for various turbine inlet total pressures and total temperatures. 142
93	Turbine polytropic efficiency based on measurements of nozzle exit total pressure and temperature, fuel fraction, and the total pressure at Station 3. 143
94	Carpet Plot of Engine A annotated with Military Performance Specifications. 148
95	Carpet Plot of Engine B annotated with Military Performance Specifications. 148
96	Carpet Plot of Engine C annotated with Military Performance Specifications. 149
97	Carpet Plot of Engine D annotated with Military Performance Specifications. 149
98	Overall performance comparison between the commercially available engines of this research and the military-grade HS TJ-50. Highlighted component performance values were used for determining the performance potential for commercially available engines. 151

Figure	Page
99	Carpet Plot of the potential performance of commercially available engines based on the best measured component performance of Engines A, B, C and D. 152
100	Effects of Instrumentation on Thrust: (a) Full Range of Operation, (b) Magnified View Near Design Point. 153
101	Effects of Instrumentation on Fuel Consumption: (a) Full Range of Operation, (b) Magnified View Near Design Point. 154
102	Performance variation in same-make, same-model engines (Engine B): (a) Corrected thrust, (b) Corrected fuel consumption. 156
103	Performance Variation in Same-Make, Same-Model Engines: Specific Fuel Consumption: (a) Full Range of Operation, (b) Near Design Point. 156

List of Tables

Table	Page
1	Basic Dimensions for Turbomachines 35
2	Typical Ranges for Turbine Design Parameters..... 57
3	Typical thermocouple calibrations and thermal ranges based on type. Data from Ref. [30]..... 68
4	Engine Geometry. 77
5	Notable published engine specifications for the four turbojets tested. *Fuel Consumption Data for Engine B published at 105 kRPM. 77
6	Compressor impeller dimensions using compressor station numbering. 80
7	Engine Weights (N). 81
8	Flexure Thrust Stand Calibrations. 98
9	Instrument specifications. 108
10	Measured vs. Published Thrust. 116
11	Trendlines relating corrected thrust (N) to corrected engine speed (% of design speed) for each engine. 116
12	Measured vs. Published: Engine Weight & T/W. 117
13	Thrust per frontal area, T/A. 118
14	Measured vs. Published Fuel Consumption. *Off-design point. 124
15	Trendlines relating corrected fuel mass flow rate (kg/s) to corrected engine speed for each engine. 124
16	Performance comparison of same-make, same-model engines (Engine B). 157

MICROTURBINE TURBOJETS: EXPERIMENTAL EVALUATION OF COMMERCIALY AVAILABLE ENGINES

I. Introduction

1.1 Research Motivation

Microturbine technology has been under development since the early 1970s. Nearly twenty years later, the first remotely-controlled aircraft was flown using a microturbine turbojet. Since then, the majority of microturbine research has been focused on power generation. The customer base for microturbine turbojets was extremely limited, but research in this field persisted in pursuit of distributed power generation grids, combined heating and power generation, and the employment of smaller and lighter auxiliary power units (APUs). Without commercial industry increasing demand for microturbine aircraft engines, the market for these engines had been driven primarily by the military. This small and specialized demand for high-performance, high-reliability engines resulted in expensive products manufactured in limited supply.

Historically, unmanned aircraft have primarily been propelled by reciprocating engines, but the recent growth of the civilian UAV market has created a demand for improved propulsion systems. When compared to reciprocating engines, gas turbines have higher thrust to weight ratios (T/W), are more reliable because they have fewer moving parts, and run on safer fuels [45]. The specifications and price-tags of military microturbine engines were generally not appropriate for civilian applications. Enabled by precision machining becoming more available and affordable, manufacturers began developing inexpensive microturbine engines to satisfy the civilian demand. This

created a new class of engine that lies somewhere between the hobby-class and the military-class. The development comes at a time when the Department of Defense is scrutinizing its budget to ensure effective utilization of its resources.

After nearly two decades of continuous, asymmetric warfare, Air Force leadership has placed an emphasis on the economics of war. At the Dubai International Air Chiefs Conference, Chief of Staff Gen. David L. Goldfein spoke to this point:

The cost-curve right now, today, is somewhat in the adversary's favor. . .It costs us far more to defend that it does for them to attack. . .[We're taking] very sophisticated weapons and shooting down very unsophisticated weapons that are attacking. . .We [need to] flip that [14].

This comment was representative of a branch-wide emphasis on improving stewardship of U.S. resources in pursuit of a more lethal Air Force. The civilian market for commercially available microturbines may provide an avenue for reducing costs while maintaining operational capability. This would be accomplished by replacing specialized, small-order, military-grade engines such as the Hamilton Sundstrand TJ-50 in Fig. 1a, with relatively inexpensive, commercially available engines, such as the engine in Fig. 1b.

In order for the U.S. Air Force to take advantage of this market, the performance of commercially available engines must meet mission requirements. This research



Figure 1. Microturbine turbojet engines: (a) Hamilton Sundstrand TJ-50 used on the ADM-160 MALD, (b) commercially available, civilian engine.

seeks to establish an understanding of the performance available from commercially available microturbine by evaluating four engines of this class and comparing them to a comparable military-grade engine, the Hamilton Sundstrand TJ-50.

1.2 Microturbine Technology

Microturbines are defined as any gas turbine producing between 30 and 330 kW of power [42]. Like any gas-turbine generator, these systems are power dense and offer lightweight, compact solutions for power-generation demands. While the small size of these systems is one of their most unique and attractive features, it creates unique design complications that are negligible in larger gas-turbine systems. Small passages increase the role of viscous forces and force critical components to operate in unusually low Reynolds Number flows. A cut-away of a microturbine turbojet is provided in Fig. 2 to illustrate engine layout and to provide a gauge for component sizes. Short

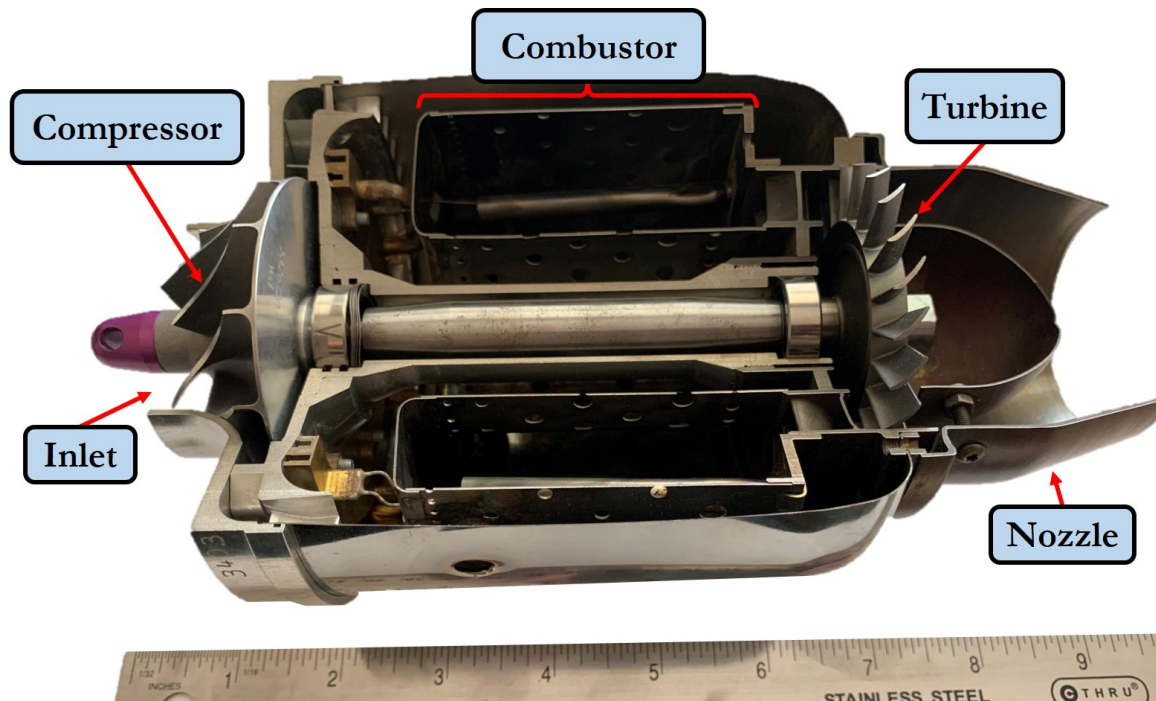


Figure 2. Cutaway of a commercially available, microturbine turbojet.

turbomachinery radii necessitate shaft speeds in excess of 100,000 RPM in order to achieve appreciable compression by the compressor and power extraction by the turbine. Restrictions on engine length demand short combustors. This design constraint results in incomplete combustion and in combustion efficiency values comparable to those of 1970s aircraft engines [24]. In addition to these issues, the sophisticated systems responsible for the ever-increasing performance of full-size, gas-turbine engines (e.g., fuel-atomization, bearing-lubrication, film-cooling, etc.) are often too small to be scaled proportionally to a microturbine engine. These issues coalesce into a challenging design problem further constrained by the need to compete economically with other well-developed small engines (i.e. reciprocating engines) vying for customers in the UAV industry.

1.3 Research Objectives

1.3.1 Primary Research Objective.

The primary research objective was to determine the potential performance for commercially available turbojets based on current market availability. To accomplish this, four engines were evaluated for overall and component-level performance. Overall performance provides an indication of performance that is currently available from a commercial-off-the-shelf (COTS) engine. Metrics used to gauge overall performance included mass air flow through the engine (\dot{m}_0), thrust-to-weight ratio (T/W), thrust-per-frontal-area (T/A), specific thrust (F/\dot{m}_0), and specific fuel consumption (S).

While overall engine evaluation provided insight into the performance that is currently available from a COTS engine, measuring component performance allowed for an assessment of the potential performance of commercially available turbojets. This potential was predicted by creating a theoretical model of an engine comprised of the

best performing components measured from any of the four engines tested. Metrics used to evaluate component performance included the overall pressure ratio (OPR) generated by the compressor, the Turbine Inlet Temperature (TIT), the corrected mass flow rate through the choked turbine throat, and turbomachinery efficiencies.

While manufacturers will typically publish some of these parameters, it is necessary to test for all performance metrics. These engines are not regulated like their larger counterparts. In the past, the Air Force Small Engines Research Laboratory (SERL) has found that published performance metrics for reciprocating engines were commonly not replicated in the lab. When available, published values were compared to measured performance. Between the four engines tested, overall and component performance were compared to identify design choices that were realized as significant variations in performance. In support of the primary research objectives, two supplemental research objectives were identified due to current gaps in understanding regarding the experimentation of microturbine engines.

1.3.2 Supplemental Research Objective: #1.

The first supplemental research objective was to investigate the effects of instrumentation on engine performance. Due to the small size of these engines, overall and component performance is inhibited by viscous forces that are relatively large when compared to full scale engines. Additionally, turbomachinery is very sensitive to distortions in the flow it ingests. Therefore, the inclusion of instruments to measure flow rates and gas properties inside the engine may significantly alter engine performance which would lead to measurements and analysis that were not truly representative of engine performance. Quantifying any deviation between instrumented and stock engine performance aided in determining repeatability and in designing future test plans.

1.3.3 Supplemental Research Objective: #2.

The second research objective was to determine the variability in performance that could be expected between same-make, same-model engines. Due to the relatively inexpensive price of these engines, it is likely that their manufacturing process does not include rigorous quality control. The trade off between highly-repeatable manufacturing and cost often favors reducing manufacturing expenses for these engines. As SERL's first attempt at investigating this issue for microturbine turbojets, two engines of the same-make, and same-model were tested for deviations in performance.

II. Literature Review

2.1 Introduction

In this chapter, a review of the literature available for micro-gas turbine engines is presented. This chapter begins with a discussion on the Brayton cycle which governs the ideal process by which gas turbine engines operate, Section 2.2. This transitions into identifying and describing the fundamental components required for a turbojet to operate on the Brayton Cycle. Section 2.3 briefly discusses the role of the inlet and nozzle. Section 2.4 provides information regarding compressors. Since the compressor is a critical component in determining engine performance, this component will be covered in more depth than others. This class of engine primarily is driven by centrifugal compressors so discussion is focused accordingly. Thermodynamic and dimensionless analysis techniques for compressors are presented as well. Section 2.5 provides information prevalent to the combustors used in microturbine turbojets. Section 2.6 presents techniques that discuss turbine performance. Section 2.7 provides overall performance metrics for expendable turbojets. After this, the chapter transitions to research conducted to determine appropriate experimental techniques. Section 2.8 covers thrust stand fundamentals, thermocouple fundamentals and corrections, and the use of Kiel Tubes to determine total properties.

2.2 Brayton Cycle Turbojets

Gas turbines operate on the Brayton Cycle. In the ideal case, the four processes constituting this cycle are: (1) isentropic compression, (2) constant pressure combustion, (3) isentropic expansion, and (4) constant pressure heat removal [24]. These four steps are illustrated in the T-S diagram presented in Figure 3. For a process to truly be considered a cycle, the same fluid must begin and end at the same state.

For a turbojet engine, the exhaust gases are not recycled back into the engine intake. Since the atmosphere contains a large enough quantity of air to supply the engine air at a reliable and constant state and the hot exhaust is returned to the atmosphere (heat rejection), the gas turbine engine can be modeled as a cycle. While utilizing an ideal cycle can be helpful in establishing a basic understanding of engine operation or in preliminary engine design, it is necessary to understand and incorporate the losses that occur in real engine operation into an engine cycle model if one wants

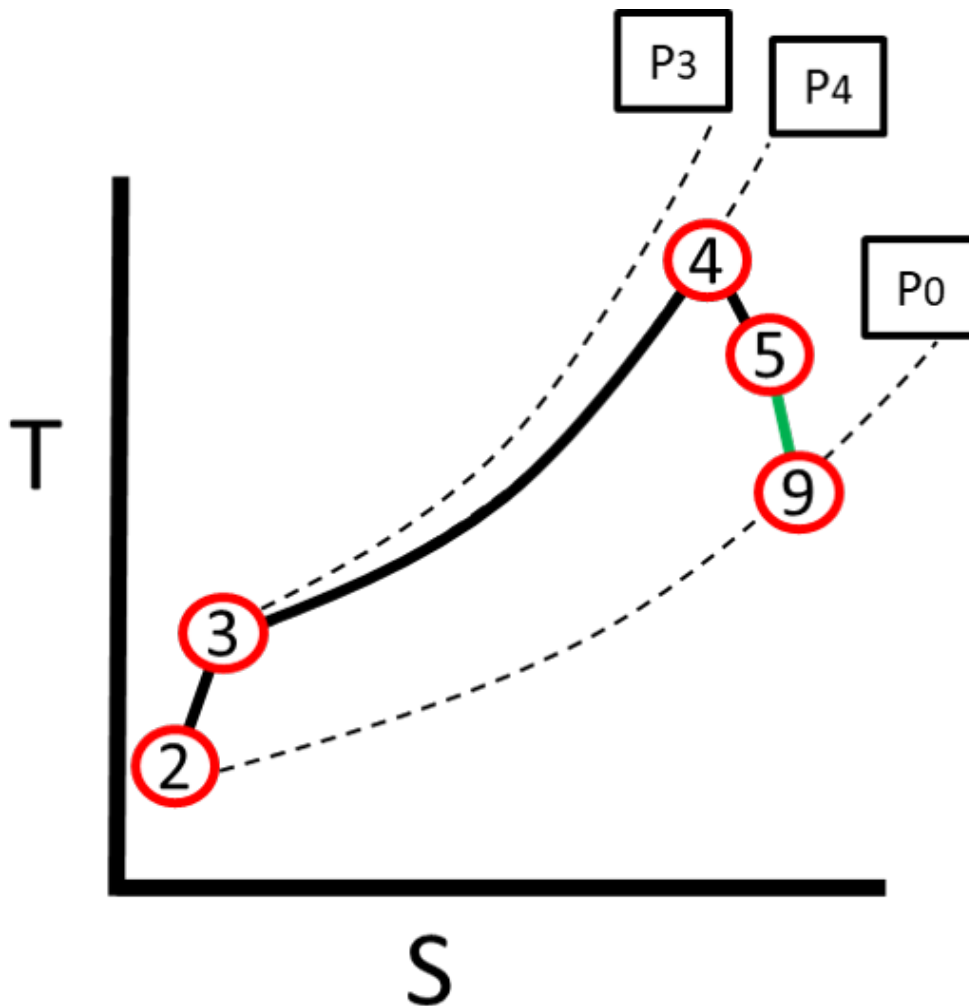


Figure 3. Brayton Cycle overlaid with turbojet station numbering. The green line indicates the energy available for propulsion in the exhaust.

to truly understand real engine operation. Figure 3 illustrates how the real Brayton Cycle (solid lines) of a turbojet engine deviates from its idealization (dashed lines); mainly, this calls for recognizing the rise in entropy across engine turbomachinery imparting or extracting work from the flow and a pressure drop that occurs through the combustion process [24].

Gas turbine generators are used as the power plant in a variety of aircraft engines. Due to this, the gas turbine generator of an engine is often referred to as the engine core. Turbojets, the simplest gas turbine engine, allow the hot exhaust of the gas turbine generator to expand and accelerate to atmospheric conditions, producing a reactionary thrust force. Other types of engines such as a turbofan or turboprop use part of the power generated by the engine core to power a fan or propeller to produce thrust. Regardless of how the energized exhaust gases are used, the engine cores serve the same function: production of hot, energized exhaust gases. For this reason, it is common for a manufacturer to save time and money by using an existing engine core design in several different engine configurations [24]. Therefore, conclusions regarding the turbojets tested in this research will be pertinent to microturbine turbofans or turboshafts as well.

Although many modern gas turbine engines are complex machines with many components, the foundation of gas turbine engine operation is fairly straightforward and requires few components. The five components necessary for a turbojet are: (1) the inlet, (2) the compressor, (3) the combustor, (4) the turbine, and (5) the nozzle. The layout of these components in a standard axial flow turbojet is provided in Figures 2 and 4. The same station numbering was used in Figures 3 and 4. In addition to identifying the role of each component, the important design decisions that drive specific component performance will be reviewed in this chapter.

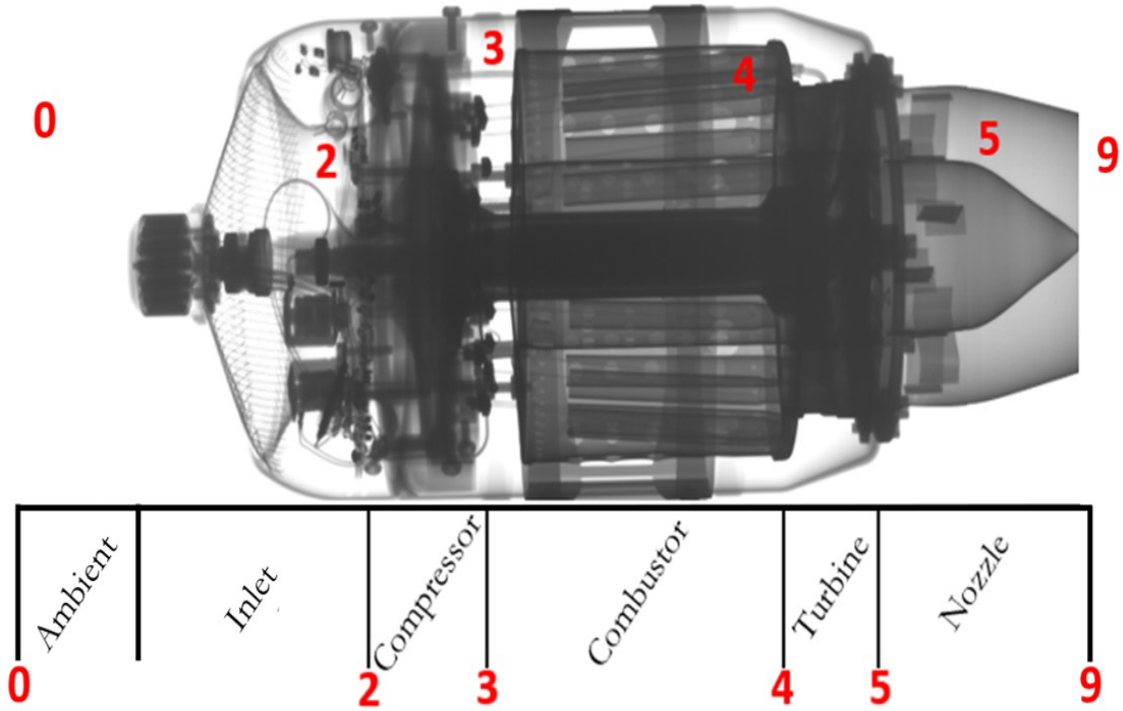


Figure 4. CT Scan of Engine B indicating locations of each engine component.

2.3 Inlet & Nozzle

The inlet of the engine is the first component to interact with the ambient fluid. The inlet has two roles: (1) efficiently supply air into the engine, and (2) if necessary, slow the flow to a velocity appropriate for the compressor [24]. When operating at high flight speeds, a sufficient amount of air is typically supplied purely from vehicle motion. At static or low speed operation, the engine must pull stagnant air through itself without the aid of a relative airspeed providing fresh air to the engine. The streamlines of air being ingested by engines moving slower, at, or faster than the inlet design condition are shown in Figure 5. All tests in this research were conducted on a static thrust stand. There was no forced air, and the engines ingested quiescent flow. Therefore, the streamlines into the inlet will look like the far left condition of Figure 5. Inlets operating in this regime can incur increased pressure loss due to the

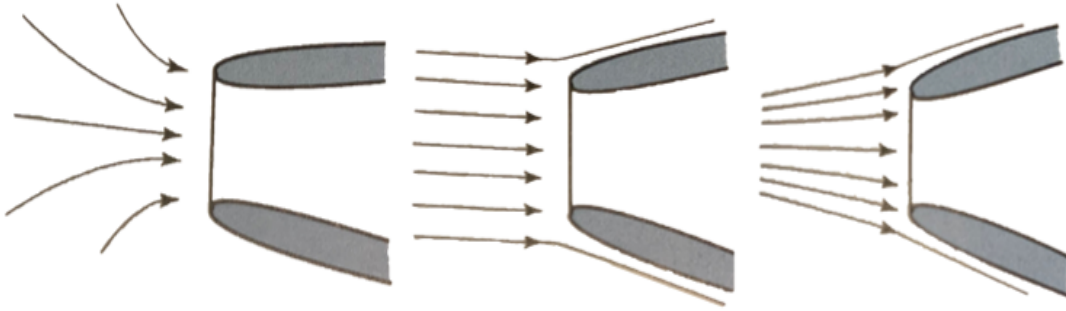


Figure 5. Nozzle intake streamlines at different flight conditions [24]

flow path around the lip of the inlet [26]. Generally, these losses are only significant for inlets with sharp leading edges. However, there is the potential that the thrust generated on the static stand will be lower than in-flight performance due to increased pressure loss across the inlet.

Opposite of the inlet, the nozzle is the last component to interact with the flow. While generally very simple in design, the nozzle's role in gas-turbine propulsion system is crucial. The nozzle is used to straighten and accelerate the flow, converting the remaining internal energy into kinetic energy. Recalling that the acceleration of fluid through the engine is the source of propulsive force, it is easily understood that while not as complex as the combustion chamber or turbomachinery of the gas-turbine engine, the nozzle is a vital engine component.

When modeling inlets and nozzles, total temperature is assumed to be constant since no work is being done within these components. Total pressure, on the other hand, decreases through these components. Total pressure ratios of 0.98 have been used to model microturbine turbojet inlet performance [20]. Regarding nozzle performance, a nozzle pressure ratio of 0.95 was assumed [24]. Additionally, it was assumed that $P_0/g \approx 1$.

2.4 Compressor

The second component to interact with the flow is the compressor. This tends to be the most crucial component to engine performance. The role of the compressor is to increase the density of the air entering the combustion chamber to facilitate a more efficient combustion of fuel [24]. Increasing air density increases the number of energetic particles acting as reactants in the combustion reaction. Since temperature is a function of the ratio of fuel to air, increasing mass air flow rate increases the amount of fuel that can be added without increasing the temperature. Therefore, higher pressure ratios allow for more energy to be added to the flow during combustion without exceeding critical temperatures based on the structural limits of the combustor and turbine. Engine operation is typically limited by the maximum compression that the compressor is capable of producing or by the melting point of engine components downstream of the combustor. There are two primary categories of compressors used in gas turbine engines: (1) axial compressors and (2) centrifugal compressors [24].

The axial compressor is the most common compressor style used in large gas turbine engines. When discussing compressors, the two primary metrics used for describing performance are the Overall Pressure Ratio (OPR) and efficiency. OPR represents the ratio of total pressure at the compressor exit to total pressure at the compressor inlet. A single-stage axial compressor has a relatively low compression ratio when compared to a single-stage centrifugal compressor. However, axial compressors can easily be combined in series to produce high overall pressure ratios (OPR). Many modern engine cores utilize large, multi-stage axial compressors that are able to achieve compression ratios up to 30. When axial compressor stages are put into series, the cross sectional area of each subsequent compressor stage must be smaller than that of the stage upstream of it. A diagram of a multistage axial compressor is seen in Figure 6. In order to maintain appropriate flow velocity through the compres-

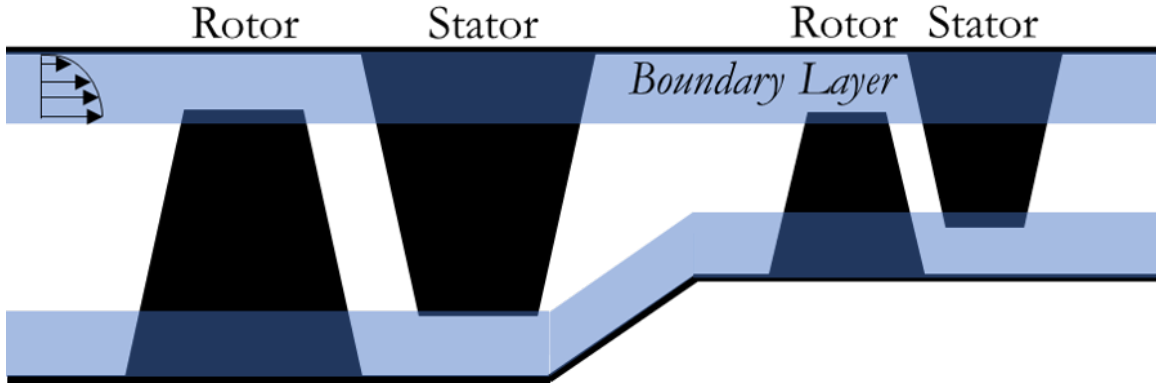


Figure 6. Relative boundary layer increase in a multi-stage axial compressor.

As the passage size must decrease as the pressure increases, the passage sizes in the compressor become small, the compressor blades begin to ingest more and more of the boundary layer off the outer casing. This increase in relative size of the boundary layer results in a radial pressure distortion for the inlet of the compressor stage. The increase in the size of the boundary layer relative to the total cross sectional area of the flow is illustrated in Figure 6.

Ariga et al. found that increasing the radial pressure distortion causes significant decrease in efficiency and unfavorable effects on the surge margin on a given compressor [1]. Several axial compressor stages would be needed to replicate the pressure ratio developed by a single centrifugal compressor. It can be inferred from the findings of Ariga et al. that a multi-stage axial compressor would suffer greater efficiency losses due to the increased relative-size of the boundary layer than would a single-stage centrifugal compressor.

Although a multi-stage axial compressor currently provides the highest overall pressure ratios, they are relatively fragile and prone to tip losses. Tip losses are the result of the airflow moving against the pressure gradient developed by the compressor. This phenomenon is illustrated in Figure 7.

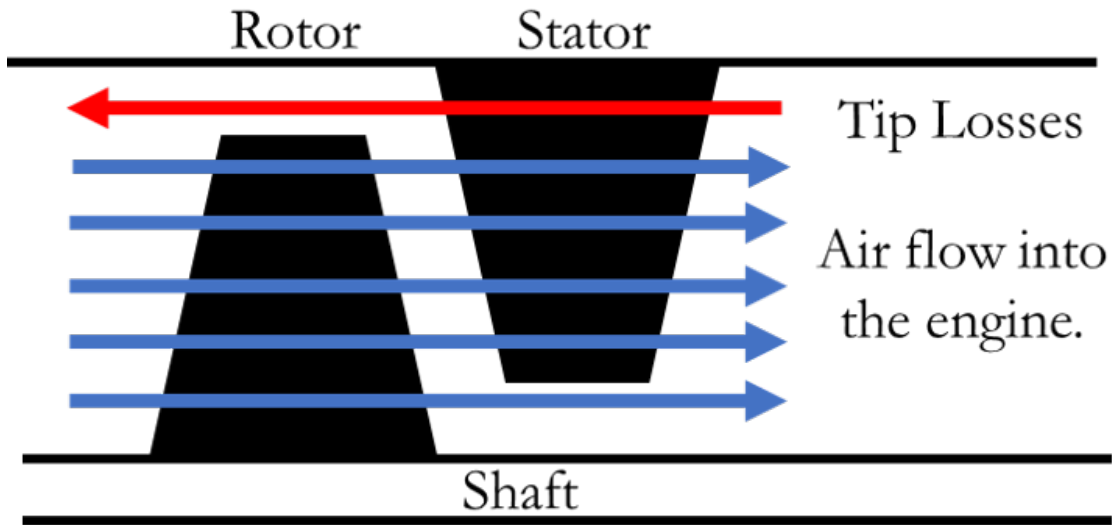


Figure 7. Illustration of tip losses on an axial compressor.

The compressor rotor blades are able to impart energy into the flow that forces it against the positive pressure gradient. Ideally, there would be no space and no contact or friction between the casing and the rotors. At high operation speeds, compressor rotors will deform due to centrifugal stresses. To prevent failure due to this elongation of the rotors, space is required between the rotor tip and the compressor outer casing. Within this space, rotors are not actively forcing air downstream, and non-ideal backflow develops as shown in Figure 7. These issues are only exacerbated when the compressor is scaled down to a size appropriate for a microturbine. This increase in tip losses stems from the relative size of the clearance compared to the blade increasing as the turbomachinery is downsized [15]. Pampreen tested the effects of variations in relative tip clearance on a four-stage axial compressor; the results are provided in Figures 8 and 9. For Pampreen’s study, the difference in tip clearance between the compressors was on the order of 0.005 inches and the tip clearance for each stage was 1-3% of the span of the blades. Figure 8 indicates a 2% decrease in overall compressor adiabatic efficiency between the two compressors. Since this performance

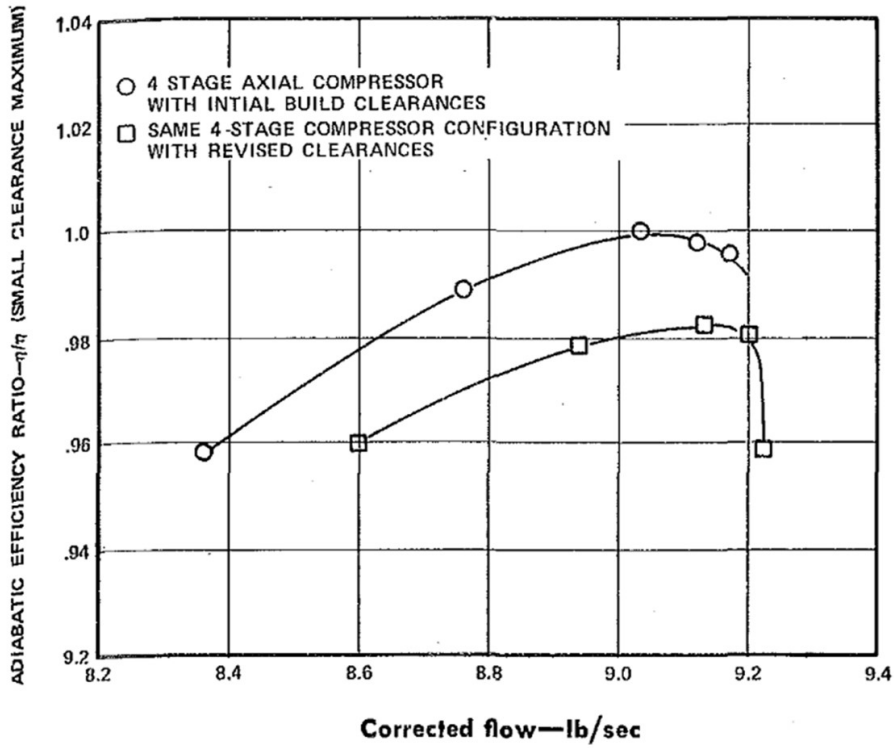


Figure 8. Effects of relative tip clearance on compressor overall adiabatic efficiency. Appended from Ref.[32].

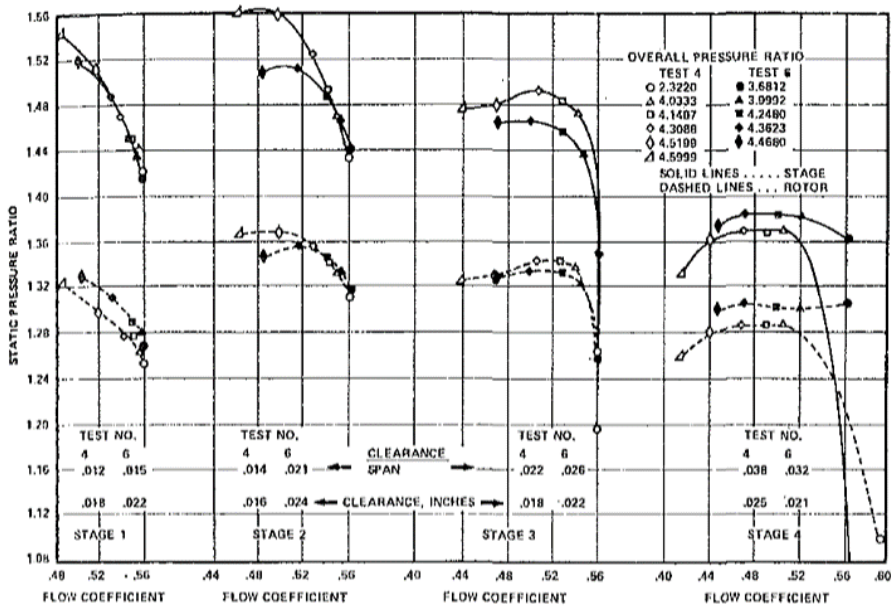


Figure 9. Effects of relative tip clearance on stage static pressure ratio. Appended from Ref.[32].

degradation was attributed to the 1-3% increase in relative tip clearance, this provides an indication of the sensitivity of compressor performance to tip clearance. In Figure 9, Pampreen's data indicates a decrease in static pressure recovery for each stage due to increasing relative tip clearance. According to this data, the latter stages were more sensitive to tip clearance than the stages upstream.

These problems pose significant issues for small axial compressors. Centrifugal compressors, on the other hand, are not as sensitive to tip clearance losses [24]. This advantage motivates many microturbine engineers to employ single-stage centrifugal compressors rather than cascades of axial stages in their designs.

For micro-gas turbine engines, centrifugal compressors are far more common than the axial compressors that are found in larger turbine engines. This is due to a lower sensitivity to the aforementioned downscaling issues. In addition to being more effective at small sizes, they offer significantly higher pressure ratios for a single stage compressor which reduces the number of components and complexity of the engine. Contrary to the typical axial compressor, a centrifugal compressor moves air outward radially. This is the natural tendency of the air traveling through rotating turbomachinery. Taking advantage of this natural tendency enables the higher single stage pressure ratios found in centrifugal compressors when compared to axial compressors. Being able to complete desired pressure ratio within a single stage is key for micro-gas turbine engines because it reduces system complexity, weight, and cost while increasing reliability.

The centrifugal compressor, a diagram of which is shown in Figure 10, is composed of three pieces: (1) the shroud, (2) the impeller, and (3) the diffuser. The impeller is a set of channels divided by rotating guide vanes (also known as rotors) that transfers shaft power to the fluid. The shroud is the outer wall of the compressor that keeps fluid within the component. Finally, fluid exiting the compressor travels through the

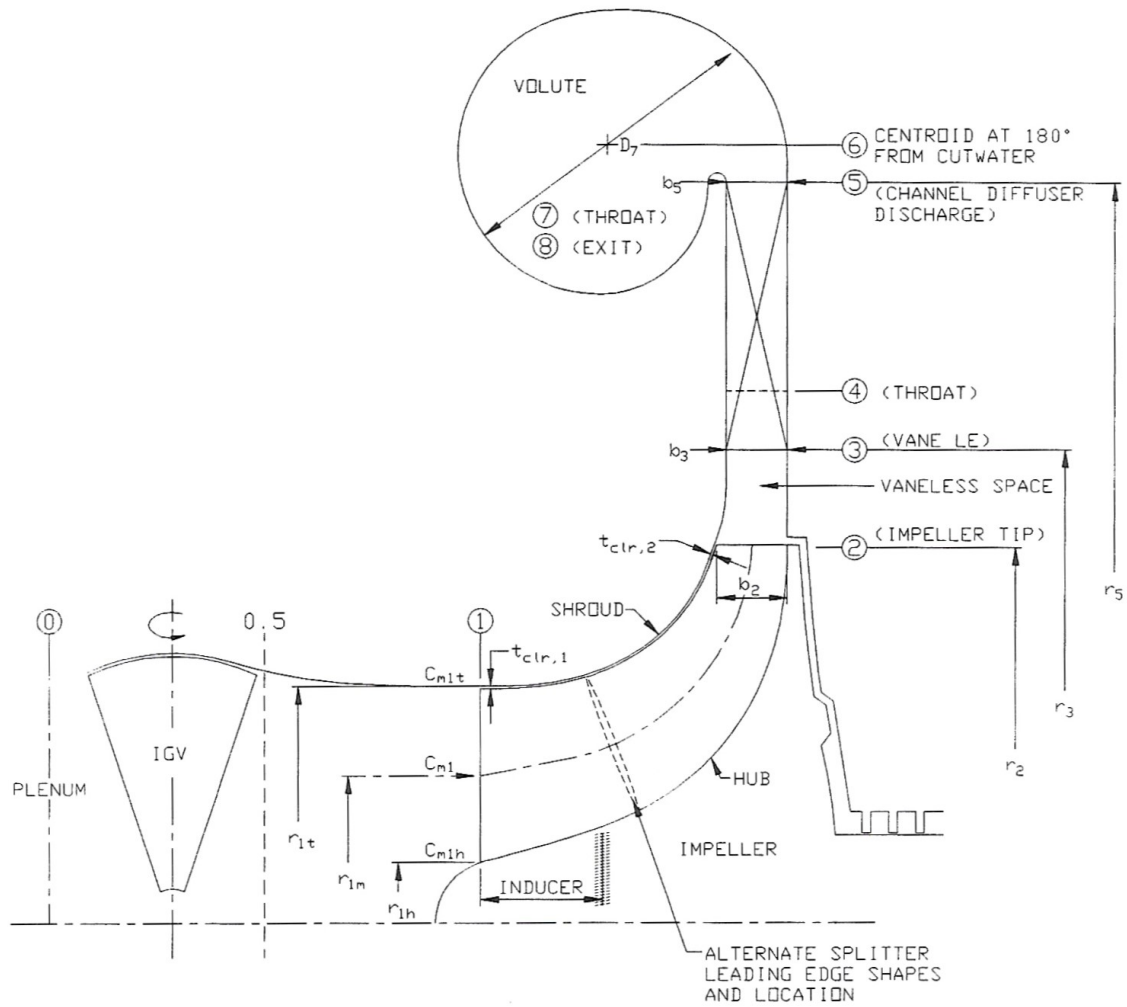


Figure 10. Meridional View of a Centrifugal Compressor [17].

diffuser which slows the fluid, decreasing the dynamic pressure and increasing the static pressure [17].

The shroud can either be attached to or separate from the impeller. When the impeller and shroud are both a single piece, the impeller is referred to as a shrouded impeller. Likewise, when the shroud is a separate piece from the impeller, and there is a gap between the impeller tip and the shroud, the impeller is referred to as an unshrouded impeller. In regard to the unshrouded impeller, the casing that surrounds the impeller is still referred to as the shroud, though the impeller itself is not a

shrouded impeller. Shrouded impellers are typically more efficient because they are not affected by tip clearance losses since the impeller blades are fixed to the shroud. However, the additional material fixed at the tip of the impeller significantly reduces the structural operating limits of the device [39]. Lower rates of rotation correspond to lower pressure rises. While the state of the art unshrouded centrifugal compressor is capable of pressure ratios on the order of 10:1 pressure gain, the shrouded impeller is limited to pressure gains of about 3:1 [39]. Since high OPRs are crucial for Brayton-Cycle performance, gas-turbine engine designers typically accept tip clearance losses for the higher pressure ratios associated with unshrouded impellers. It should be noted that the 10:1 pressure ratios are only achieved by significantly larger centrifugal compressors than are employed in microturbine turbojets. For the compressors found in these engines, pressure ratios of 5-6 are considered very high performance.

The impeller is the rotating component of the compressor. Responsible for transferring shaft power into the fluid, most of thermodynamic properties of fluid traveling through the compressor can be directly related to the impeller. The leading edge of the compressor is referred to as the inducer, named so due to its role in drawing (inducing) fluid flow through the compressor. By moving flow at the front of the impeller, the inducer causes a rise in dynamic pressure and decrease in static pressure at the tip of the impeller, creating a static pressure gradient between the free stream flow and the higher speed flow accelerated by the inducer and drawing fluid through the compressor. To better understand compressor flow physics, it is useful to consider the component velocity diagrams.

2.4.1 Centrifugal Compressor Velocity Triangles.

The velocity diagram for flow traveling through the inducer is shown in Figure 12. The incidence angle, i , is the angle of attack seen by the compressor blade:

$$i = \beta_b - \beta \quad (1)$$

In order to avoid compressor blade stall, the blade angle of the inducer, β_{1b} , must be designed to match the inducer relative flow angle, β_1 . The flow angle is driven by the relative velocity of the approaching air, W_1 , and blade velocity, U_1 [17]. Comparable velocity triangles for the compressor exit are provided in Figure 13. Typically, the velocity component tangential to the compressor is related to the compressor tip speed via the slip factor, ϵ :

$$\epsilon = C_{\theta 2}/U_2 \quad (2)$$

This assumption simplifies centrifugal compressor analysis by representing unknown fluid velocities in terms of easily measurable tip speeds. Section 2.4.4 provides more details on slip factor and the methods used to calculate it.

It is important to note that since rotor speed is a function of rate of rotation and radius, $U = \omega r$, for a given inlet flow, assuming the flow is uniform across the entire cross sectional area, β will be lower at the hub and than at the tip [24]. This concept can be easily visualized in the velocity diagrams of Figure 11.

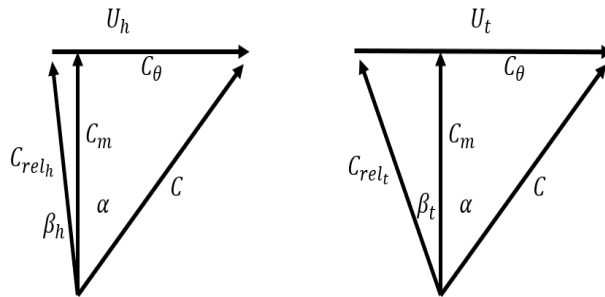


Figure 11. Inducer velocity diagrams at the (a) hub and (b) tip. Note: although no swirl was depicted in this diagram, the same tendency occurs for the case of uniform swirl.

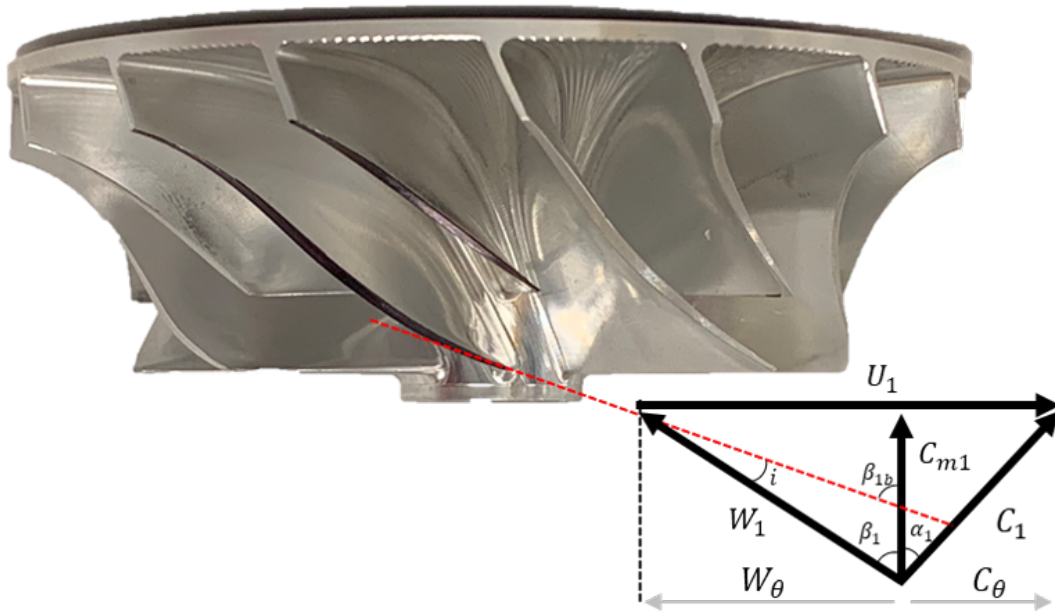


Figure 12. Velocity Triangle of Flow at the Inducer.

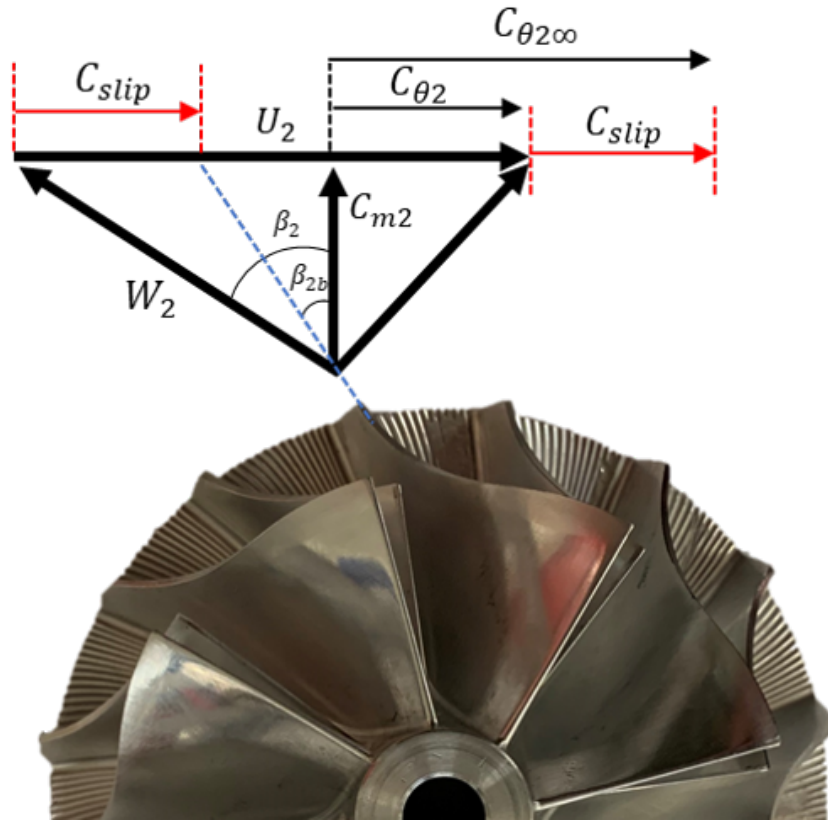


Figure 13. Velocity diagram of the flow exiting a centrifugal compressor.

2.4.2 Thermodynamics & the Euler Pump Equation.

Turbomachinery performance is often described using the Euler pump equations which relate the work done by the turbomachinery to the enthalpy before and after the component as shown by Equation 3 [24]:

$$\dot{W} = \dot{m}\Delta h_t = \dot{m}\omega(r_e v_e - r_i v_i) \quad (3)$$

Since none of the engines considered in this study have inlet guide vanes, it is acceptable to assume that the inlet velocity has zero swirl, $v_i = 0$. Along with assuming a calorically perfect gas, this allows for a useful simplification of this equation:

$$c_p \Delta T_t = \omega r_e v_e \quad (4)$$

Recognizing that $\omega r_e = U_t$ and recalling Equation 2, the total temperature change can be written in terms of the rotor tip speed and the slip factor:

$$\Delta T_t = \frac{\epsilon U_t^2}{c_p} \quad (5)$$

Compressor performance is measured by two figures of merit: (1) the pressure rise across the component, and (2) the efficiency with which that pressure rise occurs. In any gas turbine engine, useful energy that could be used for thrust must be used to drive the compressor. Therefore, the efficiency with which the compressor is able to achieve the desired pressure ratio is an important parameter in maximizing thrust. There are two popular ways of characterizing efficiency: (1) adiabatic efficiency, η , and polytropic efficiency, e [2]. The adiabatic efficiency of a compressor is given by the ratio of the ideal amount of energy needed to drive the desired pressure change to the actual amount of energy needed as shown by Equation 6:

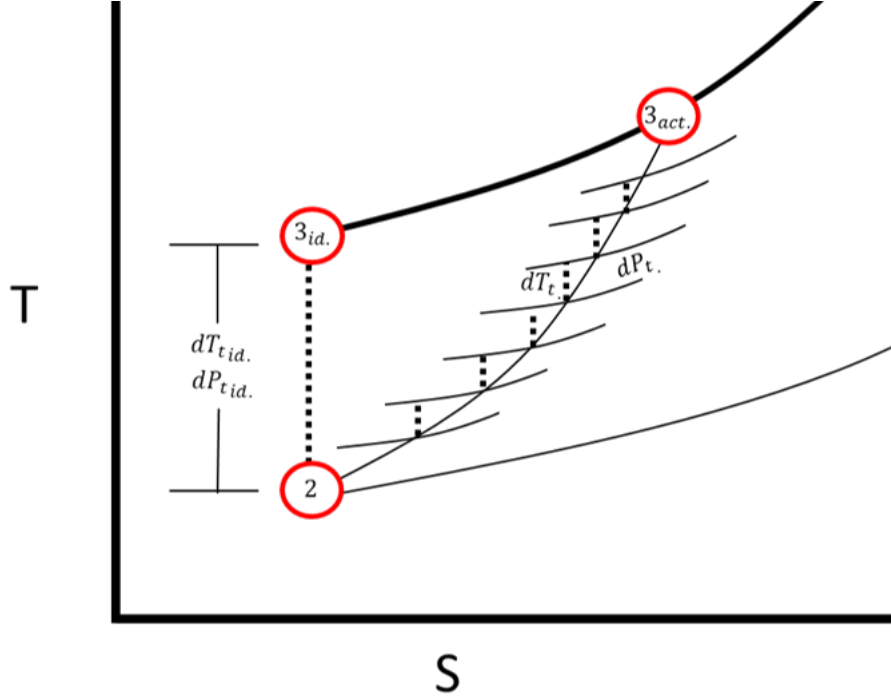


Figure 14. Compressor pressure ratio curve divided into infinitesimal pressure gains for derivation of polytropic efficiency.

$$\eta_c = \frac{\dot{W}_{ideal}}{\dot{W}_{actual}} = \frac{h_{t3i} - h_{t2}}{h_{t3} - h_{t2}} \quad (6)$$

By assuming the air interacting with the compressor is a calorically perfect gas and recognizing the isentropic change in pressure as the ideal case, Equation 6 can be written in terms of total temperature and total pressure ratios, shown in Equation 7:

$$\eta_c = \frac{\pi_c^{(\gamma-1)/\gamma} - 1}{\tau_c - 1} \quad (7)$$

The adiabatic efficiency defined in equation 6 is sensitive to the pressure ratio produced [3]. For a performance metric independent of the size of the pressure ratio, the polytropic efficiency, e_c , is used. The polytropic efficiency is defined by considering an infinitesimally small pressure changes (shown in Figure 14) and integrating between the compressor inlet and exit conditions. A brief derivation of the polytropic efficiency

is useful in developing an understanding of the differences between isentropic efficiency and polytropic efficiency.

$$e_c = \frac{(dh_t)_{ideal}}{(dh_t)_{actual}} \quad (8)$$

The ideal change in enthalpy can be solved for by starting with the Gibb's Equation. Since this is the ideal process, it is isentropic and therefore $ds = 0$. By employing the Ideal Gas Equation of State, the total density can be rewritten in terms of total pressure, total temperature and the Gas Constant, R . This development is shown in Equations 9.

$$(T_t ds)_{id.} = (dh_t)_{id.} - \frac{1}{\rho_t} dp_t \quad \longrightarrow \quad (dh_t)_{id.} = \frac{1}{\rho_t} dp_t \quad \longrightarrow \quad (dh_t)_{id.} = \frac{RT_t}{p_t} dp_t \quad (9)$$

Determining an expression for the actual change in enthalpy relies on knowing that the change in enthalpy of a gas of known composition is totally dependent on the change in temperature experience by the gas. Rewriting the constant pressure specific heat of the gas in terms of the ratio of specific heats and R , a useful form of the actual change in enthalpy is reached, shown in Equations 10.

$$(dh_t)_{id.} = c_p dT_t \quad \longrightarrow \quad (dh_t)_{id.} = \left(\frac{\gamma - 1}{\gamma} \right) R dT_t \quad (10)$$

These expressions for the ideal and the actual change in enthalpy are substituted into the definition of compressor polytropic efficiency from Equation 8. Integration between the compressor inlet and exit conditions yields a useful form of the equation for polytropic efficiency, shown in Equation 11.

$$e_c = \int_2^3 \frac{\frac{RT_t}{p_t} dp_t}{\left(\frac{\gamma-1}{\gamma}\right) R dT_t} \rightarrow \boxed{e_c = \frac{\gamma - 1}{\gamma} \frac{\ln(P_{t3}/P_{t1})}{\ln(T_{t3}/T_{t1})}} \quad (11)$$

Solving the Euler Pump Equation for T_{t3} and substituting that expression into Equation 11 allows for the pressure ratio across the compressor to be determined as a function of the slip factor, the tip radius, the rate of rotation, and the polytropic efficiency as shown in Equation 12 [24]:

$$\pi_c = \left(1 + \frac{\epsilon U_t^2}{g_c c_p T_{t1}}\right)^{\frac{\epsilon c \gamma}{\gamma-1}} = \left(1 + \frac{\eta_c \epsilon U_t^2}{g_c c_p T_{t1}}\right)^{\frac{\gamma}{\gamma-1}} \quad (12)$$

Upon inspection of Equation 12, it is apparent that the pressure ratio across the centrifugal compressor increases exponentially with tip speed. The significance of this observation can be observed in Figure 15.

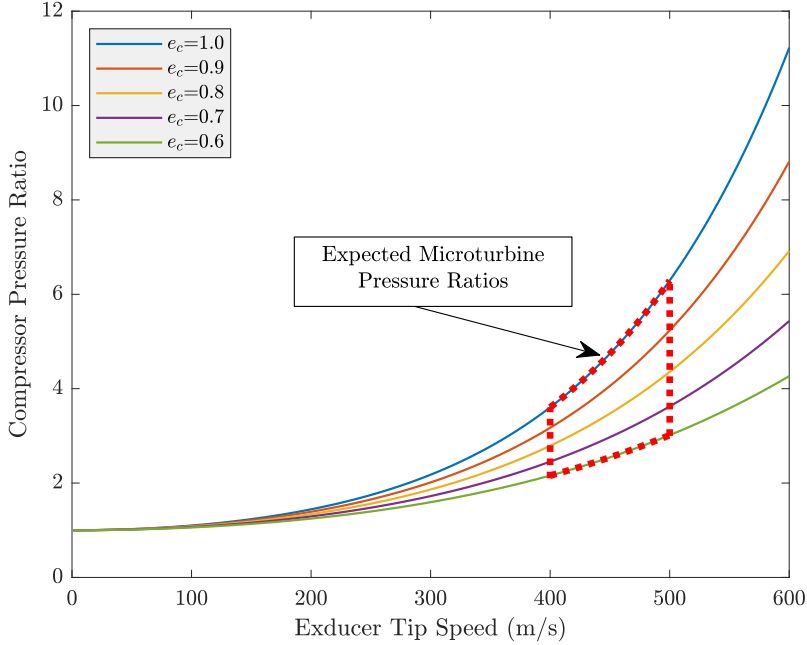


Figure 15. Exponential dependency of compressor pressure ratio for the centrifugal compressor on tip speed. Assumes $\epsilon = 0.8$.

2.4.3 Rotor Backsweep.

This section reviews the thermodynamic effects of employing rotor backsweep in a centrifugal compressor. Generally, backsweep reduces theoretical thermodynamic performance but increases aerodynamic stability. Since compressor instability can reduce engine performance and potentially cause engine failure, microturbine turbojets typically utilize backswept rotors. Compressor instabilities were not encountered in this research. Therefore, this section only seeks to provide the background necessary to understand and to quantify the thermodynamic effects of backswept rotors and does not address compressor stability.

The fundamental differences in performance of radial and of backswept rotors is best visualized via comparison of velocity triangles, as shown in Figure 16. For this comparison, the flow rate and the compressor power are conserved. Conserved flow rate necessitates that C_{m2} is equivalent for (a) and (b). According to the Euler Pump

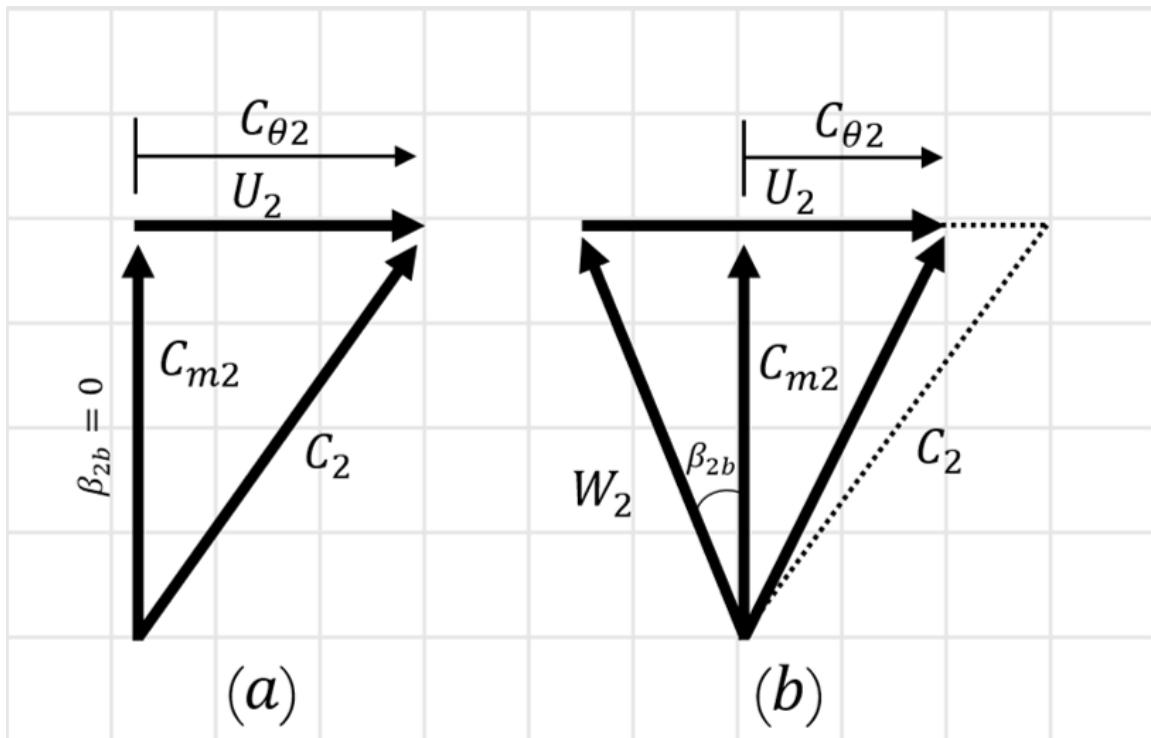


Figure 16. Compressor exit velocity triangles: (a) Radial rotors, (b) Backswept rotors.

Equation, seen in Equation 13, conservation of power is indicated by equivalence of the product, $U_2C_{\theta 2}$,

$$\Delta h_t = U_2C_{\theta 2} - U_1C_{\theta 1} \xrightarrow{C_{\theta 1}=0} \boxed{\Delta h_t = U_2C_{\theta 2}} \quad (13)$$

The thermodynamic effects of this change in geometry become apparent by analyzing the velocity triangles. First, increasing backsweep angle a decrease in the swirl velocity, $C_{\theta 2}$, relative to the tip speed U_2 [18]. Therefore, to do a given amount of work, an impeller with backswept blades will need to spin faster than an impeller with radial blades assuming all other impeller geometry is kept constant (i.e. blade count, radius, etc.). For the sake of illustration, consider the velocity triangles of two impellers generating the same amount of work, Figure 16. Impeller (a) has radial blades, while Impeller (b) has blades with a backsweep angle of β_{2b} . The work done by both impellers is given by the velocity product, $U_2C_{\theta 2} = 9$. For Impeller (a), there is no backsweep; therefore, $U_2 = C_{\theta 2} = 3$. When considering the impeller with backswept rotors, (b), $C_{\theta 2}$ is reduced to 2. Therefore, in order to conserve power, U_2 must increase to 4.5. The reduction in exit swirl velocity is realized as a steeper pressure ratio to flow curve as illustrated in Figure 17. In the context of this report, compressors are operating at very high speeds, so it should be expected that increased backsweep angle will reduce pressure ratio.

The second notable conclusion to draw from Figure 16 is related to the magnitude of the absolute velocity of the flow exiting the compressor, C_2 . For high flow rates, the velocity magnitude is larger exiting (a) the compressor with radial rotors than it is exiting (b) the compressor with backswept rotors. In (b), the dashed lines represent an overlay of (a). Since the velocity exiting the compressor is lower, the flow has to be slowed down less in the diffuser. Therefore, a compressor with backswept rotors will have a higher adiabatic efficiency than a compressor with radial rotors [17].

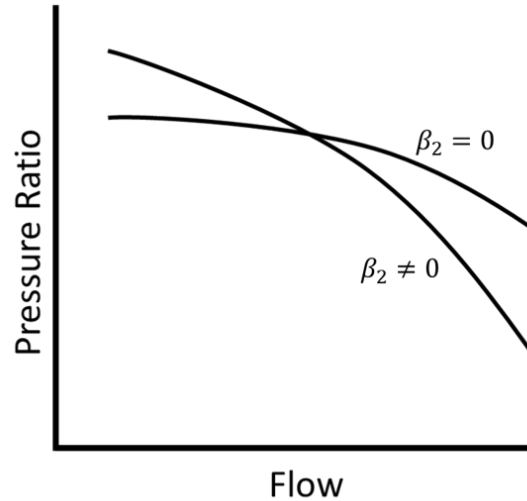


Figure 17. Effects of Backsweep Angle on Compressor Pressure Ratio.

Increasing speed and backsweep angle to increase efficiency is limited by increased centrifugal loads and the ensuing potential for structural failure. The compressors found in microturbine engines are fairly similar to those found in automotive turbochargers [15]. Most turbochargers have maximum tip speeds of 400-550 m/s due to structural limitations [6]. In addition to altering the velocity triangles and theoretical thermodynamics of the compressor, backsweep angle is very influential in determining the compressor slip.

2.4.4 Calculation of Compressor Slip.

Understanding the slip velocity of the compressor allows the flow velocity to be related to the impeller velocity and greatly simplifies calculations. The slip velocity, illustrated in Figure 13, is defined by Equation 14. An interesting theoretical derivation is found in Appendix B of Ref. [22]. Commonly, a dimensionless parameter, the *slip factor*, is used to relate compressor slip to some known geometrically defined velocity. The application of turbomachinery across many unique industries and fields has produced a wide range of nomenclature and representations of similar concepts.

There are many definitions of slip factor, the most common are presented below:

$$\text{Slip Velocity [18]:} \quad C_{slip} = C_{\theta 2\infty} - C_{\theta 2} \quad (14)$$

$$\text{Slip Factor Definition \#1 [18]:} \quad \sigma = 1 - (C_{slip}/U_2) \quad (15)$$

$$\text{Slip Factor Definition \#2 [18]:} \quad \sigma' = C_{\theta 2}/C_{\theta 2\infty} \quad (16)$$

$$\text{Slip Factor Definition \#3 [24]:} \quad \epsilon = C_{\theta 2}/U_2 \quad (17)$$

In 1973, an extensive collection of empirically derived compressor slip factors was gathered and presented by Noorbakhsh [29]. Japikse consolidated this data and produced the charts shown in Figure 18 to visualize the effects of variations in backsweep angle for compressors of a given number of blades. The compressors used by Noorbakhsh to gather this data were all designed for pump applications. As proven by Figure 18, slip factor is dependent on impeller geometry. Therefore, if an empirical correlation is to be used to determine slip factor, it is important that the correlation be derived from a data set similar to the intended application. While the data in Figure 18, will not be directly useful in determining slip factor for a microturbine compressor, the relationships it visualizes will persist. First, slip factor is constant through regions of low flow rates. This is visualized as the horizontal sections of each curve. Second, increasing blade angle results in a decrease in slip factor. As illustrated by Figure 16, increasing backsweep angle causes a decrease in $C_{\theta 2}$. This decrease in tangential velocity would be represented as an increase in σ' if slip velocity stays constant for a given flow. Finally, by comparing the three charts in Figure 18, it

can be seen that an increase in the number of blades, Z or n , is generally accompanied by an increase in σ' .

Many researchers have suggested correlations to determine slip factor. The most universally accepted estimation of slip factor was proposed by Busemann in 1928 [5] [47]. A simpler empirical correlation was proposed by Wiesner in 1967 which aligned well with the results of Busemann [47]. The Wiesner slip factor correlation is still used today as a benchmark against which new correlations are compared [17]. Several slip factor correlations are presented below [17]:

$$\text{Wiesner: } \sigma = 1 - \frac{\sqrt{\sin\beta_{2b}}}{Z^{0.70}} \quad (18)$$

$$\text{Mattingly: } \epsilon = 1 - \frac{2}{n} \quad (19)$$

$$\text{Stanitz: } \sigma' = 1 - 0.315\left(\frac{2\pi}{Z_R} \sin\phi_2\right) \quad (20)$$

$$\text{Balje: } \sigma' = \frac{Z_r}{Z_R + 6.2\left(\frac{r_1}{r_2}\right)^{2/3}} \quad (21)$$

$$\text{Pfleiderer: } \sigma' = \frac{1}{1 + \frac{3.6}{Z_R} \frac{1}{1 - (r_{1m}/r_2)^2}} \quad (22)$$

$$\text{Stechkin: } \sigma' = \frac{1}{1 + \frac{2}{3} \frac{\pi}{Z_R}} \quad (23)$$

$$\text{Amsler: } \sigma' = 1.0 - 1.25 \frac{C_{m2}}{U_2} \pi^2 \frac{b_2}{(2r_2)} \quad (24)$$

$$\text{Yadav and Misra: } \sigma' = 1 - \frac{0.855\pi^2 C_{m2}}{Z_R U_2} \quad (25)$$

References [17], [47], and [49] all provide comparisons of empirical and theoretical slip factor correlations including the context in which they were derived. Reference [46] provides details on the application of slip factor to off-design conditions.

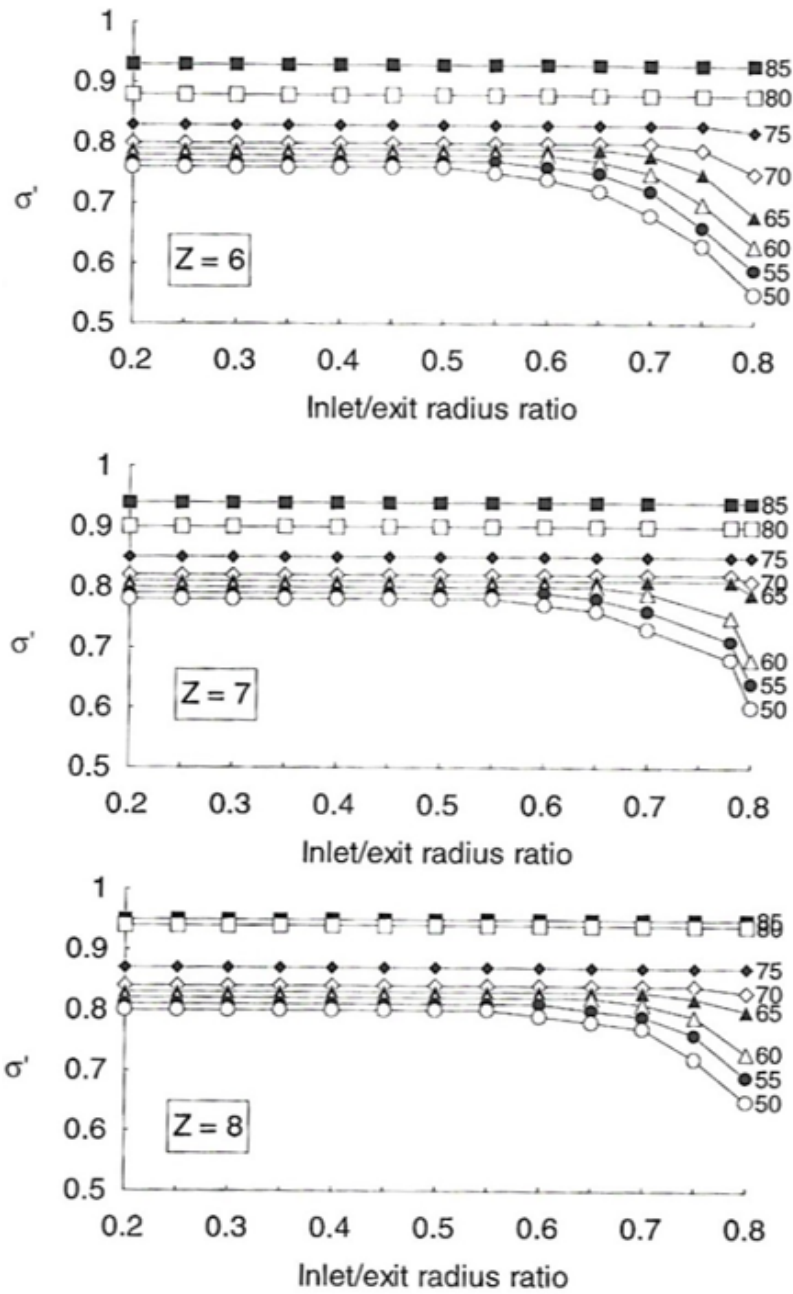


Figure 18. Empirical Slip Factor Results. Each Curve represents a unique backsweep angle, β . Each of the three graphs represents a distinct number of blades, Z [29].

2.4.5 Dimensionless Analysis.

Japikse, a leader in centrifugal compressor technology since the 1980s, states that one of the most common methods for engineering design, especially within turbomachinery, is to start with an existing design that has similar properties to what is desired in the new application and to reduce or increase the size of that component until it fits the new application [17]. A valuable tool, this design methodology allows an engineer to quickly re-engineer a known design for a new applications. However, as Japiske and many others in the field of turbomachinery point out, this technique has its limitations, especially when attempting to miniaturize components to the level necessary for incorporation to micro-gas turbines. Small turbomachinery components are plagued by physical losses that limit their ability to maintain the same performance as their larger counterparts. In his work testing the centrifugal compressor of a JetCat P-200, Grannan cites three physical phenomenon as the primary drivers of increased losses in small turbomachinery: (1) an increase in the relative tip losses on the compressor and turbine, (2) an increase in the relative size of the boundary layer along passage walls compared to the entire flow, and (3) a decrease in Reynolds number, indicating an increase in viscous forces present in the flow [15].

In his survey of the design limitations of micro-gas turbines, Braembussche also enumerates three major sources of the losses associated with micro-turbomachinery [43]. Like Grannan, he cites the significance of a change in Reynolds Number and links this to the relatively large boundary layers found in micro-turbomachinery. Additionally, he claims that the small size and close proximity of engine components allow for significant conductive heat transfer to occur between components, deteriorating the performance of engine components, especially the compressor. Finally, Braembussche identifies the manufacturing limitations of engines of this size. The

tolerances necessary to reduce the tip clearance losses referred to by Grannan are too tight for typical manufacturing to produce reliably.

Braembussche states that in order for the scaling method proposed by Japiske to be used correctly, relevant parameters must be conserved. In order to preserve the efficiency of turbomachinery when scaling, Braembussche claims the three parameters which must be conserved are: (1) velocity triangles, (2) Mach Number, and (3) Reynolds Number [43]. The conservation of velocity triangles between designs can be achieved through a balance of on the design flow speed, rate of rotation, and geometry. Before discussing the Mach Number and Reynolds number, it is useful to recall that the Euler Turbomachinery Equations relate the enthalpy change across a piece of rotating turbomachinery to the outer radius and the rate of rotation, as shown by Equation 26. The Mach Number, given for turbomachinery by Equation 27, can therefore be written as a function of enthalpy change and inlet conditions (reflected by the speed of sound in the denominator).

$$\Delta H = \omega^2 R_2^2 \quad (26)$$

$$M = \frac{\omega R_2}{\sqrt{\gamma RT}} = \sqrt{\frac{\Delta H}{\gamma RT}} \quad (27)$$

This relationship shows that Mach Number can be conserved while maintaining the amount of work done by the compressor simply by trade-offs between rate of rotation and compressor size. The same cannot be said regarding Reynolds Number, defined for turbomachinery in Equation 28.

$$Re \equiv \frac{\rho}{\mu} \omega R_2^2 = \frac{\rho}{\mu} R_2 \sqrt{\Delta H} \quad (28)$$

Upon inspection of Equation 28, it is apparent that the Reynolds Number is a function of both the enthalpy change, the compressor radius, and the fluid properties. Assuming operation in the same fluid, this indicates that when scaling a compressor, both efficiency and enthalpy change across the stage cannot be conserved. In order to keep Reynold Number constant, the change in enthalpy across the turbomachinery must change to account for the change in size [43]. Though incomplete, these parameters begin to reveal the utility of non-dimensional analysis when working with turbomachines.

When comparing turbomachinery components, it is often useful to work in terms of dimensionless parameters. Important component parameters are found to be strongly linked to dimensionless properties. The Buckingham Pi Theorem offers a means of creating the dimensionless parameters necessary for turbomachinery analysis. Balje states that there are eight variables that affect turbomachinery performance: (1) Speed, (2) Diameter, (3) Volumetric Flow Rate, (4) Density, (5) Head, (6) Viscosity, (7) Power, and (8) Compressibility. Each parameter plays an important role in turbomachinery performance [2], and each must be represented in a system of related dimensionless terms if their effects on turbomachinery performance are to be used as points of comparison between various designs.

The Buckingham Pi Theorem is commonly used to create dimensionless groupings of variables so that similitude can be considered between various manipulations of a given design. Consideration of similitude is commonly seen in applications such as wind tunnel testing in which a smaller model is used to represent a larger design. This theorem is equally useful in establishment of dimensionless groupings, called dimensionless terms or dimensionless products, to be used in turbomachinery design. The wide range of turbomachine applications, from the hyraulic turbines used in the Hoover Dam to the small turbomachinery in the turbojets studied in this report can

be compared by using dimensionless terms. The Buckingham Pi Theorem decomposes each physical variable into its basic dimensions and then uses this representation of the variables to create a set of dimensionless groupings known as *Pi terms*, Π . The number of Pi terms needed to describe the system is dependent on the number of *physical variables* affecting the system, k , and the number of *basic dimensions* that constitute the physical variables. This set of dimensionless quantities offers a means of comparing the effects of individual parameters.

In the field of fluid dynamics, there are three basic dimensions: (1) mass, M , (2) length or distance, L , and (3) time, t [28]. Force can replace mass as a basic dimension because it is related to mass as a function of length and time. The analysis in this text will be conducted using the $M L t$ system of basic dimensions. In some instances, temperature, T , is included as a fourth basic dimension [28]. For this reason, the time dimension which is commonly represented as T will be represented as t . Moran describes the process for solving for dimensionless products using the Method of Repeating Variables. Below is an abbreviated version of the process outlined by Moran [28]:

- Step 1.** Determine the relevant physical variables.
- Step 2.** Determine the basic dimensions that constitute each physical variable.
- Step 3.** Determine the number of Pi terms needed to evaluate similitude.
- Step 4.** Select r of the physical variables to be the repeating variables. The basic dimensions must be represented by all (but not each) of the repeating variables.

Step 5. Create Pi terms by multiplying each non-repeating variable by all of the repeating variables. Each of the repeating variables is raised to an exponent. These exponents are manipulated to ensure that the product is dimensionless.

The five dimensionless Pi terms for turbomachines developed using the Buckingham Pi Theorem are presented in Table 1. As an example, the flow coefficient, ϕ , a common dimensionless term used for turbomachinery analysis, is derived using this method. This term is often seen as a ratio of the meridional velocity at the compressor inlet to the tip speed at the compressor exit, $\phi = u_1/U_t$, as shown by Balje and by Mattingly [2] [24]. As an example, this term will be derived via the Buckingham Pi Theorem. Steps 1 and 2 are represented by the **Physical Parameter** and the **Basic Dimension** columns of Table 1, respectively.

Step 3. As stated earlier, there are eight physical dimensions used to describe turbomachines. Therefore, $k = 8$, $r = 3$, and the number of dimensionless products required is $p = 5$.

Step 4. Identify ρ , D , and N as the repeating variables.

Table 1. Basic Dimensions for Turbomachines

Physical Parameter	Symbol	Basic Dimensions	Dimensionless Pi terms
Speed	N	t^{-1}	Repeating Variable
Diameter	D	L	Repeating Variable
Density	ρ	ML^{-3}	Repeating Variable
Volumetric Flow Rate	Q	L^3t^{-1}	$\phi = \frac{Q}{ND^3} \propto \frac{u_1}{U_t}$
Head	H	L^2t^{-2}	$\psi = \frac{H}{D^2N^2}$
Viscosity	μ	$ML^{-1}t^{-1}$	$Re = \frac{\rho DN^2}{\mu}$
Power	\dot{W}	ML^2t^{-3}	$C_P = \frac{\dot{W}}{\rho N^3 D^5}$ or $\frac{\Delta h_t}{h_{t1}}$
Compressibility	E	$ML^{-1}t^{-2}$	$M = \frac{ND}{a}$

Step 5. The flow coefficient is a dimensionless term representing the Volumetric Flow, Q . Therefore, the dimensionless product will be in the form:

$$\rho^a D^b N^c Q \quad \longrightarrow \quad (M^a L^{-3a}) (L^b) (t^c) (L^3 t^{-1}) \quad (29)$$

By representing the variables in this expression in terms of basic dimensions, the exponents of like-terms can be collected and set to zero to ensure a dimensionless product:

$$M : a + 0 = 0 \rightarrow a = 0 \quad (30)$$

$$t : -c - 1 = 0 \rightarrow c = -1 \quad (31)$$

$$L : -3a + b + 3 = 0 \rightarrow b = -3 \quad (32)$$

Using these exponents, the dimensionless Pi term (the flow coefficient) can be expressed in terms of the repeating variables and the volumetric flow rate.

$$\Pi = \phi = \frac{Q}{ND^3} \quad (33)$$

This representation of the flow coefficient is agreeable with the publications of Logan [22]. This representation is proportional, but not equivalent to the expressions for flow coefficient given by Balje and by Mattingly, $\phi = u1/U_t$ [2] [24]. One disadvantage to the use of dimensionless terms is their susceptibility to proportional scaling issues. Thus, it is important to understand what field and context in which the dimensionless parameter is being used.

A more physical derivation of the flow coefficient is useful in understanding how it can be used as a metric for normalizing mass air flow rate. The flow coefficient is a

normalization of the velocity through the compressor via the tip speed. Through the continuity equation, the velocity is related to the mass air flow rate via Equation 34:

$$c_m = \frac{\dot{m}_0}{\rho A_2} \quad (34)$$

where A_2 is the cross sectional area at the leading edge of the inducer. Accounting for the shaft, A_2 is given by:

$$A_2 = \frac{\pi}{4} (OD_2^2 - ID_2^2) \quad (35)$$

If corrected values for mass flow rate and engine speed are used, density becomes a constant, and the relationship for ϕ scales proportionally with the ratio of mass air flow rate to engine speed, as shown in Equation 36:

$$\phi = \left(\frac{1}{\rho A_{f2} r_{t2}} \right) \frac{\dot{m}_0}{N} \quad \longrightarrow \quad \phi \propto \frac{\dot{m}_{0,c2}}{N_{c2}} \quad (36)$$

From this, plotting ϕ against engine speed provides a normalized mass flowrate that can be used to compare design without interference of geometry and sizing.

The other four Pi terms can be determined through similar analysis. Reassuringly, the dimensionless terms representing viscosity and compressibility are the familiar Reynolds Number and Mach Number. When analyzing compressors, Reynolds Number is considered at the component inlet stagnation conditions [18]. Figure 19 shows the relationship between efficiency decrement and compressor inlet Reynolds Number. Efficiency decrement is a measure of the adiabatic losses in the compression process. As indicated by the trends in Figure 19, adiabatic efficiency decrement is inversely proportional to Reynolds Number such that $(1 - \eta) \propto -0.164Re$ for $Re \leq 3.0E6$ [32]. Compressors operating at Re exceeding this threshold are relatively insensitive to changes in Re .

In order to write the Pi term for compressibility as the Mach Number, the relationship between the Elasticity Modulus of a fluid, E , and the speed of sound must be understood to be $a = \sqrt{E/\rho}$. The dimensionless product for head is oftentimes referred to as the stage loading coefficient or the work factor. Since head is equivalent to work, the stage loading coefficient can be written in terms of total enthalpy or total temperature [2] [24].

$$\psi = \frac{H}{N^2 D^2} \propto \frac{g_c \Delta h_t}{U_t^2} = \frac{g_c c_p \Delta T_t}{U_t^2} \quad (37)$$

Once again, the two representations are proportional but not equivalent. In this case, this difference stems from the tip speed being a function of the radius and the Buckingham Pi representation being a function of diameter. In neither of these expressions is there a constant factor of 4 to account for this difference between D^2 and r^2 .

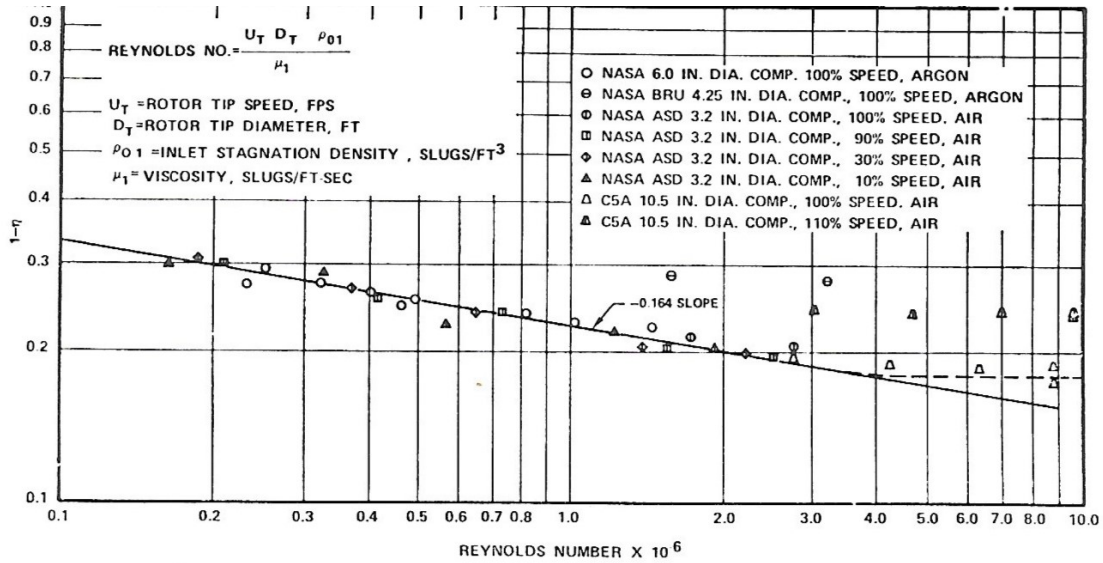


Figure 19. Compressor adiabatic efficiency decrement vs. Reynolds Number at compressor inlet [18].

2.4.6 Specific Speed and Specific Diameter.

Other useful dimensionless quantities can be made via combinations of the five Buckingham Pi Terms for turbomachines, shown in Table 1. Two such combinations of Pi terms are of significant importance: specific speed and specific diameter. One of the most significant design parameters for turbomachinery design, the specific speed is characteristic of the meridional profile of the turbomachinery. Given by a proportion of the flow coefficient and loading coefficient, the specific speed can be calculated using Equation 38 [33]:

$$N_s = k \frac{\phi^{0.5}}{\psi^{0.75}} \quad (38)$$

where k is a constant that varies depending on units system and application and where ϕ and ψ are the stage loading coefficient and flow coefficient. For the nondimensional specific speed, k is simply unity [33].

The appropriate specific speed of the compressor is dependent on the application. The specific speed of centrifugal compressors typically ranges from 0.5-2.0. The specific speed of an axial flow compressor is much higher, ranging from 1.5-20 [22]. This relationship between specific speed and compressor shape is illustrated in Figure 20. Rodgers narrows the classification of centrifugal compressors by prescribing specific applications for centrifugal compressors within aircraft engines based on specific speed, shown in Figure 21 [23] [35]. Here, Rodgers presents a relationship between specific speed and efficiency, a concept that can be expanded using the specific diameter dimensionless term.

Cordier found that the maximum efficiency for any piece of turbomachinery is related to specific speed and specific diameter, shown by the empirically derived Cordier Diagram in Figure 22. Cordier found that for a given specific speed, there is a specific diameter that produces the maximum efficiency for that turbomachine.

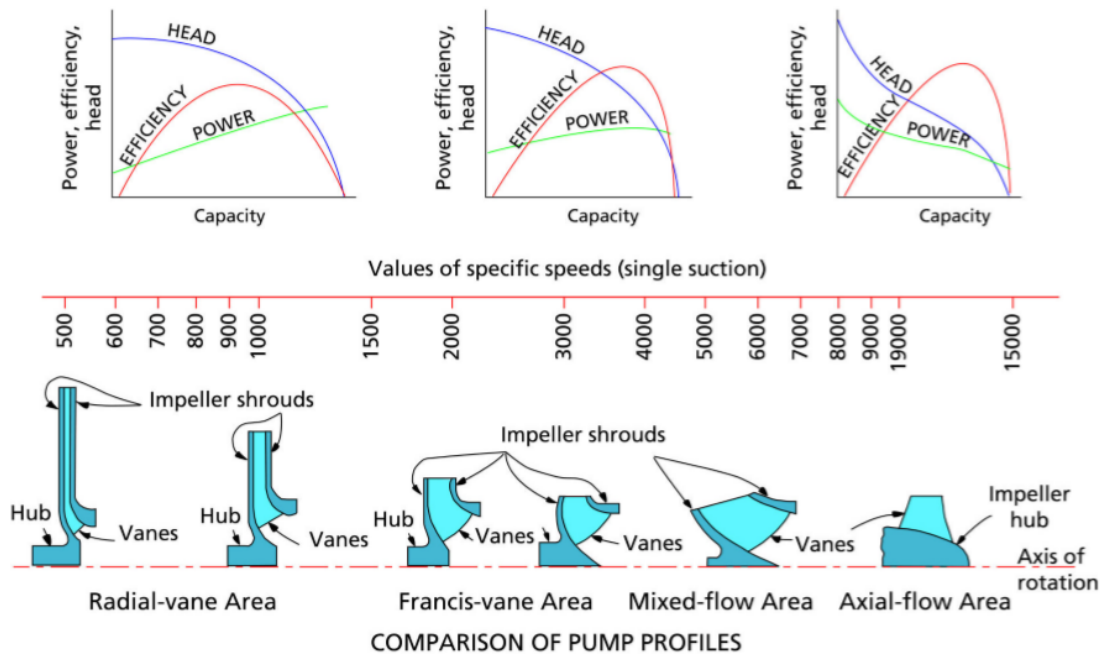


Figure 20. Balje Diagram showing the effect of variations in specific speed [7].

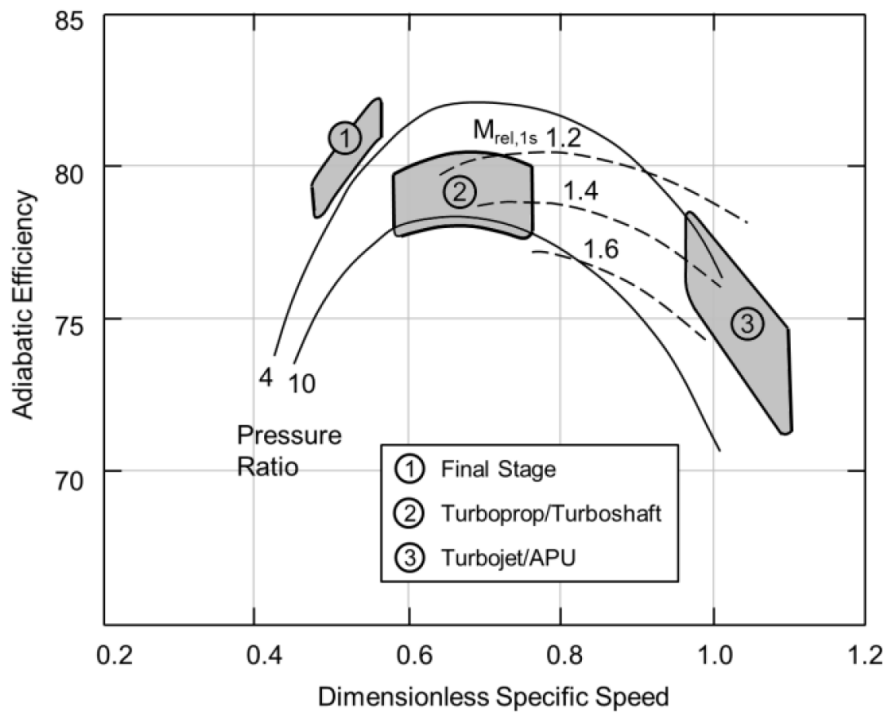


Figure 21. Centrifugal compressor application in aircraft engine based on specific speed regimes [23] [35].

Like specific speed, the specific diameter of a turbomachine can be determined as a product of the flow coefficient and the work factor, as shown by Equation 39:

$$D_s = \frac{\psi^{0.25}}{\phi^{0.5}} \quad (39)$$

Cordier's findings were expanded upon and eventually condensed to the Cordier Line. The Cordier Line is a useful design tool because it allows for efficiency to be estimated based on compressor geometry, speed and flow rates. Logan provided ranges of specific speed that aligned with different types of turbomachines. The range of specific speed appropriate for centrifugal compressors is appended to the Cordier Line in Figure 23. According to the Cordier Line, in order to maximize efficiency, centrifugal compressors should have specific diameters on the range $2 \leq d_s \leq 5.5$. In Section 4.2, the Cordier Line is used to motivate isolating compressor performance from diffuser performance in future work.

By identifying the desired application, a centrifugal compressor can be designed by using the specific speed as a similarity parameter. In the same manner that matching the Reynolds number between two cases is used to create similar viscous conditions, matching the specific speed creates ensures similar thermodynamic and flow conditions between compressors. Fundamentally, the specific speed is a relationship between the tip speed, the meridional (axial) velocity, and the work done by the impeller. The constant used to scale is just for the sake of achieving speed values that are related to the given application (i.e. pump vs. compressor, English vs. Metric units, etc.) Due to the strong dependency of the impeller thermodynamic effects on the impeller geometry, especially the radii throughout the impeller, the specific speed is commonly said to be indicative of the meridional shape of the impeller. Recall the meridional view of a centrifugal compressor shown in Figure 10.

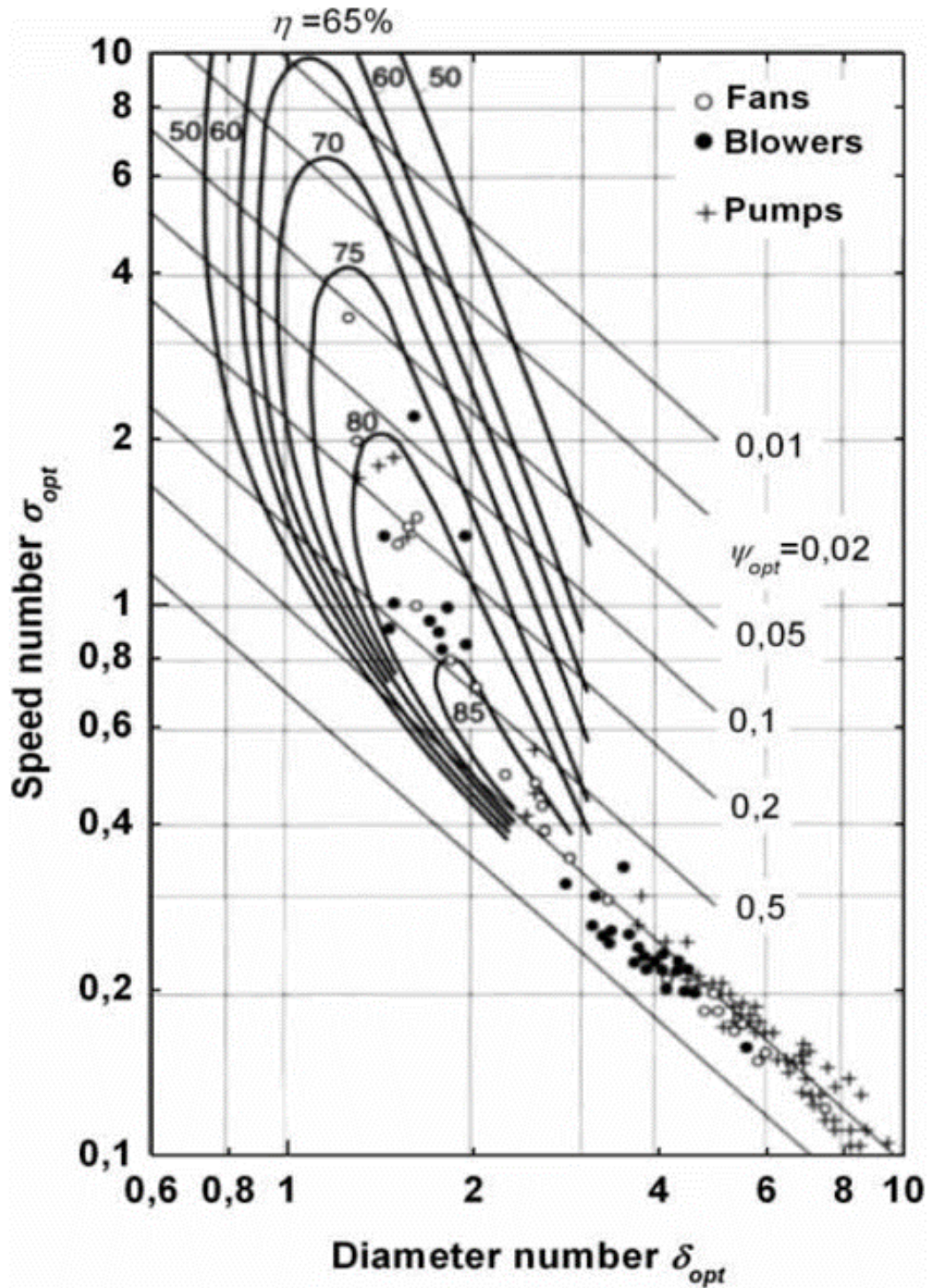


Figure 22. Original Cordier Diagram relating specific speed and specific diameter to contours of empirically derived adiabatic efficiency [8] [12].

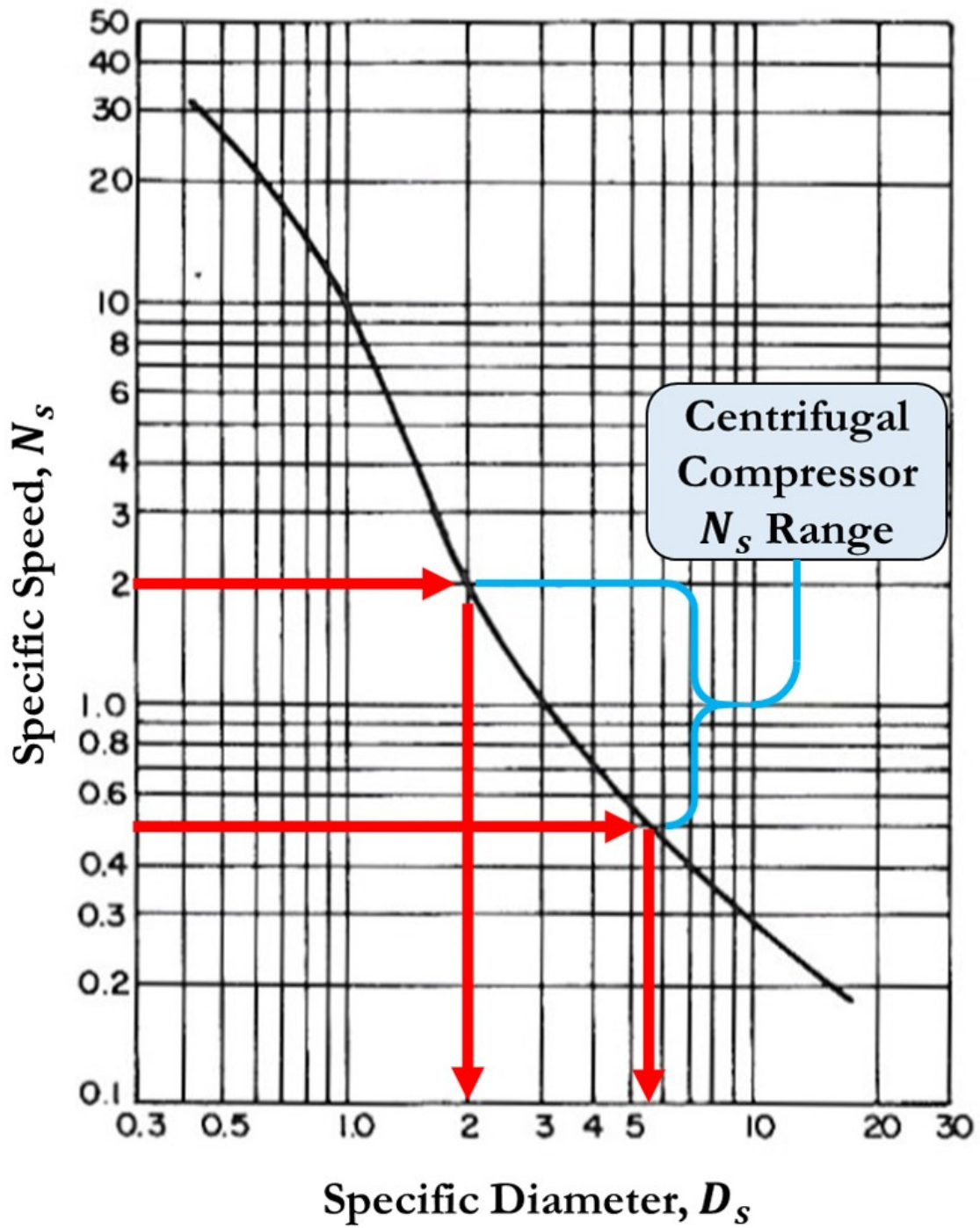


Figure 23. General Cordier Diagram illustrating the peak efficiency line highlighting the N_s range appropriate for centrifugal compressors. Appended from [22].

In 1980, Collin Rodgers briefed the significance of specific speed on impeller design to the NATO Advisory Group for Aerospace Research and Development. His work is still used in modern centrifugal compressor research as shown in Ref.'s [17], [23], and [43]. His primary conclusion in this report, the correlation between specific speed and impeller polytropic efficiency, can be visualized by the results of his experiments shown in Figure 24.

With this information, Rodgers showed that compressor polytropic efficiency was closely related to specific speed. Compressor efficiency was relatively insensitive to variations in relative flow angles at the compressor exit [33]. While blade exit angle does not have a direct effect on efficiency, it does have an effect on the amount of work done which affects work factor, ψ . Recall Equation 38 which shows that specific speed is a function of ψ .

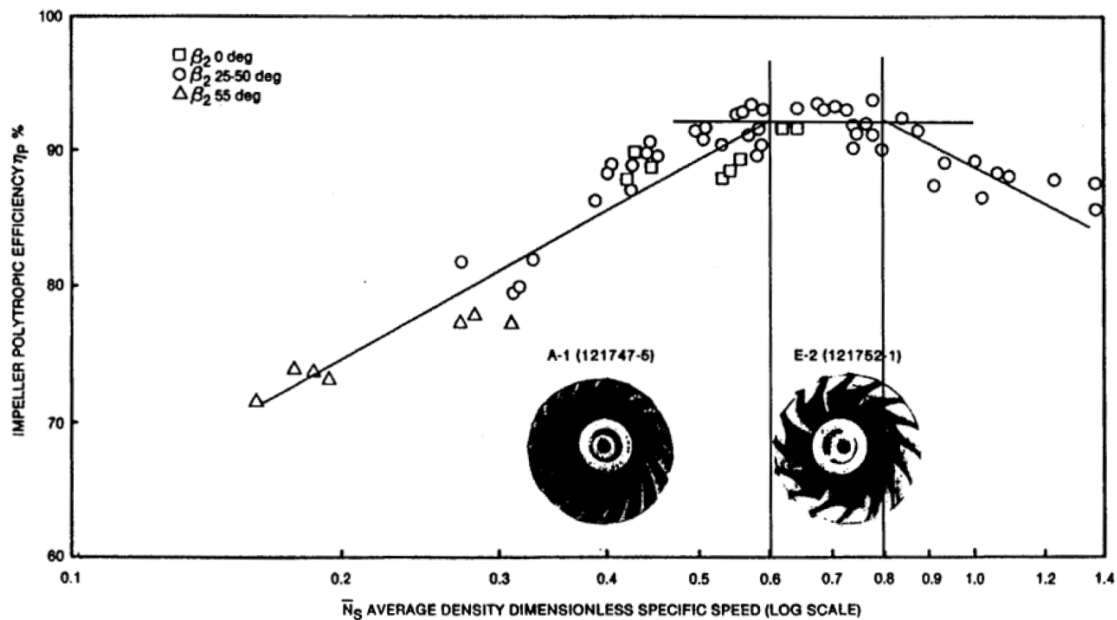


Figure 24. Experimental results from Rodgers's 1980 report showing the correlation between specific speed and impeller polytropic efficiency. Original Ref: [33]. Appended Ref: [43].

2.4.7 Diffuser Performance.

The final compressor component is the diffuser. Responsible for slowing the flow and converting dynamic pressure into static pressure, the diffuser is crucial for preparing the incoming air for combustion. Figure 25 provides two views of microturbine diffusers overlaid with compressor station numbering. The first two stations are best shown in Figure 25a. Station 1 is located at the leading edge of the compressor inducer. Station 2 is located at the tip of the compressor exducer and the beginning of a vaneless diffuser. The next three stations are more easily visible in Figure 25b. Station 3 represents the end of the vaneless diffuser and the beginning of a vaned diffuser. Station 4 represents the throat of the vaned diffuser, and Station 5 represents the exit of the vaned diffuser. As noted in Figure 25a, there are two vaned diffusers in these engines. The first is oriented radially; the second is oriented axially. The leading edges of the second vaned diffuser are visible in Figure 25b.

In general, two performance characteristics are used to describe the diffusion process: (1) static pressure recovery and (2) total pressure loss. The static pressure recover is an indicator of how much velocity was converted into static pressure. This

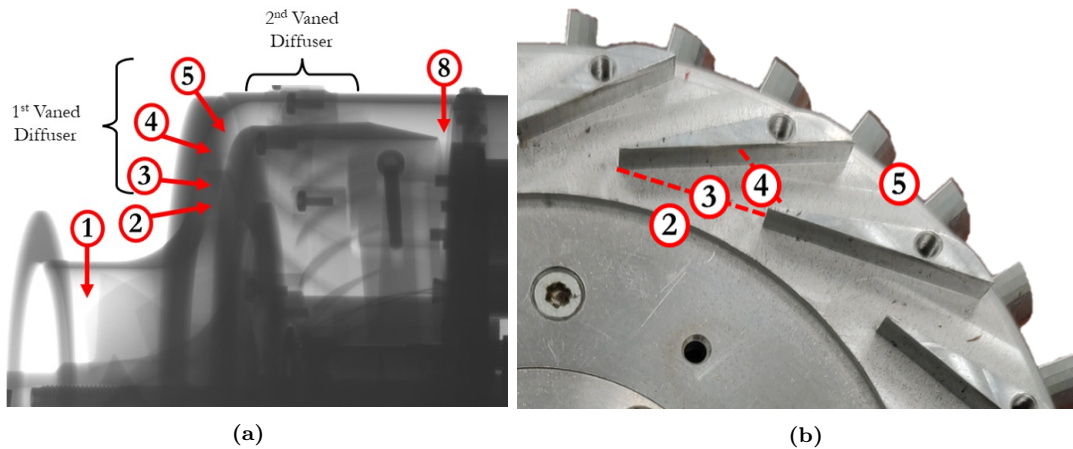


Figure 25. Station Numbering used for compressor analysis overlaid on: (a) engine CT scan, (b) photograph of diffuser. Both images are of Engine D. Station Numbering from [18].

is useful for the compressor of a gas turbine engine because high static pressure increases the number of molecular collisions which increases combustion efficiency. The total pressure loss coefficient is a measure of the efficiency of the diffusion process. Loss of total pressure indicates that less useful work can be done with the flow. In the case of a gas turbine engine, a decrease in total pressure is ultimately realized as a decrease in thrust. Equations 40 and 41 relate the diffuser inlet conditions to the exit conditions via the static pressure recovery coefficient, $C_{p,2m-4}$, and the total pressure loss factor, K_{2m-4} , respectively [18]:

$$\text{Static Pressure Recovery:} \quad p_4 = p_{2m} + C_{p,2m-4} (p_{02m} - p_2) \quad (40)$$

$$\text{Total Pressure Loss:} \quad p_{04} = p_{02m} - K_{2m-4} (p_{02m} - p_2) \quad (41)$$

where p_{2m} and p_{02m} represent the static and total pressures at the compressor exit, p_4 and p_{04} represent the static and total pressures at the diffuser exit.

The static pressure recovery is closely tied to the blockage in the diffuser. Blockage, B , is related to the Discharge Coefficient, C_D . This relationship is given in Equation 42. Discharge Coefficient is given by Equation 43 [34]:

$$\text{Blockage:} \quad B = 1 - C_D \quad (42)$$

$$\text{Discharge Coefficient:} \quad C_D = \frac{\dot{m}_0}{\left(\frac{\dot{m}_0 \sqrt{T_t}}{\sqrt{AP_t}}\right)_{3,4} \left(\frac{AP}{\sqrt{T_t}}\right)_{3,4}} \quad (43)$$

Experimental evaluation of diffuser performance has been found to be extremely sensitive to measurement uncertainty. Figure 26 presents data on static pressure recovery coefficients compared to blockage. The uncertainty in measured static pressure recovery coefficient is on the order of 15%.

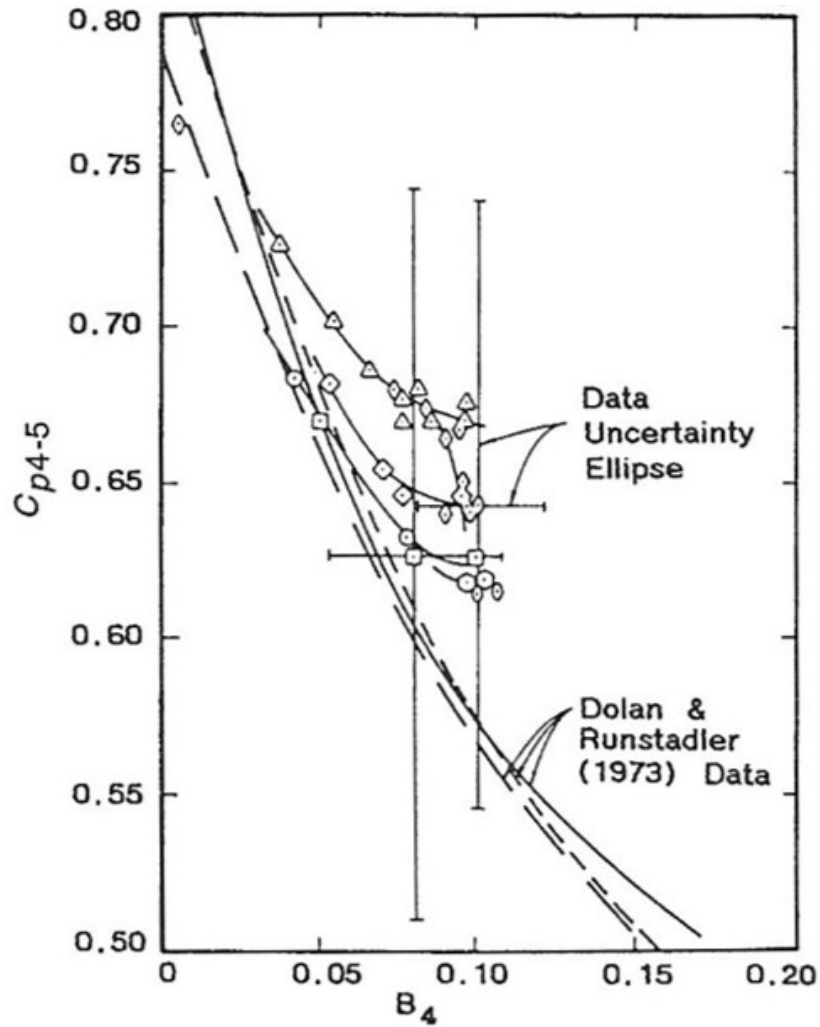


Figure 26. Empirical Static Pressure Recovery Coefficients taken in an applied setting (i.e. within an engine) compared to data from a highly instrumented lab setting. Illustrates high degree of uncertainty associated with diffuser measurements [11].

Diffusers are commonly separated into two categories: (1) vaneless and (2) vaned. Vaneless diffusers rely solely on the conservation of angular momentum to slow the flow down as it moves further radially from the compressor. As shown by Equation 44, as r_3 increases, $C_{\theta 3}$ will decrease. This relationship only applies to the tangential velocity component. The radial velocity component is not affected by the increase in distance from the center of rotation and stays relatively constant.

$$\text{Angular Momentum: } H_0 = r_3 C_{\theta 3} \quad (44)$$

The two most common types of vaneless diffusers are constant width, seen in Figure 27a, and pinched, seen in Figure 27b. There are many other variations of these designs, but constant width and pinched are two of the fundamental shapes used. These diffusers are commonly found in automotive turbochargers [18]. It is typical to find vaneless diffusers used in conjunction with vaned diffusers as there will be some open space through which the flow is only slowed via conservation of angular momentum and an increasing distance from the center of rotation. The reduction in speed through a vaneless diffuser is not an isentropic process. Losses in angular momentum can range from 5% to 15% [18]. Because angular momentum is proportional to velocity and dynamic pressure is proportional to velocity squared, losses in angular momentum are realized as significantly higher losses in terms of total pressure.

$$H_0 = r C_\theta \quad q = \frac{1}{2} \rho C^2 \quad (45)$$

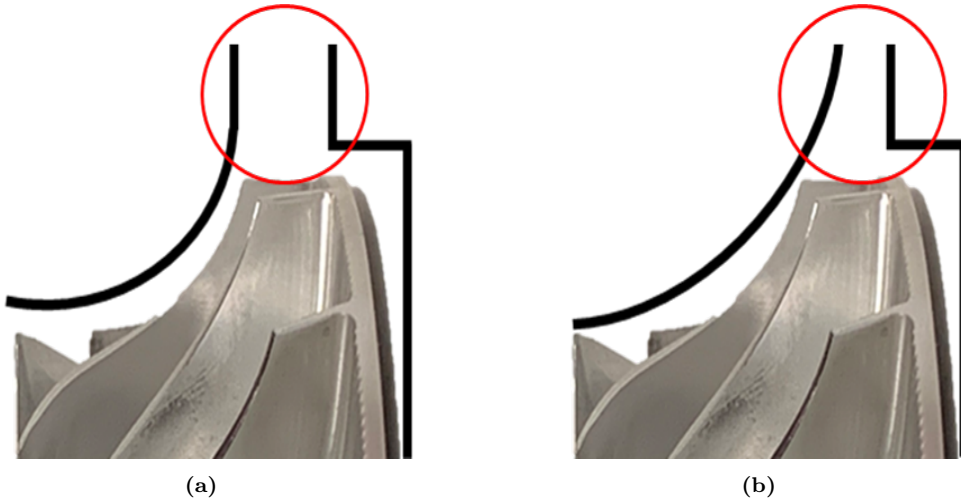


Figure 27. Vaneless Diffusers: (a) Constant Width, (b) Pinched.

Generating the necessary diffusion using only vaneless diffusers would require too wide of a diffuser to be appropriate for an aircraft engine. Vaned diffusers are commonly employed to generate higher static pressure recovery over a shorter distance. Vaned diffusers can also be separated into two categories: (1) channel diffusers and (2) airfoil diffusers [18] shown in Figures 28a and 28b, respectively. Historically, the accepted rule of thumb has been that channel diffusers have higher static pressure recovery than airfoil diffusers and are considered higher performing. However, Japikse notes that modern airfoil diffuser designs are becoming more effective, reducing the accuracy of this rule of thumb [17]. Additionally, this guideline only applies to static pressure recovery not total pressure loss.

Using the information presented in this section, the exit conditions and the specific work done by the compressor, w_c , can be calculated using Equations 46. The most accurate way of determining enthalpy is to use a database that lists enthalpy as a function of temperature and fuel fraction such as Appendix L of Reference [24].

$$P_{t3} = \pi_c P_{t2} \quad T_{t3} = \tau_c T_{t2} \quad h_{t3} \propto T_{t3} \quad w_c = h_{t3} - h_{t2} \quad (46)$$

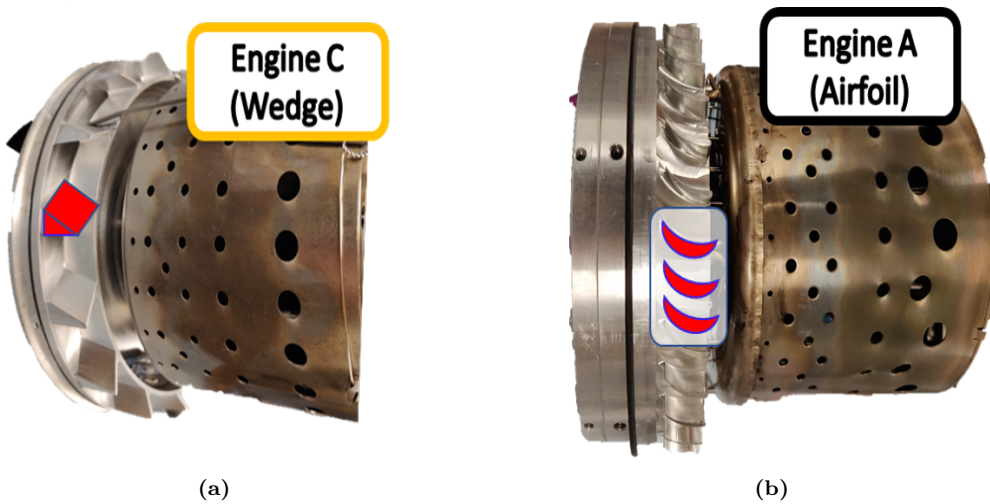


Figure 28. Vaned Diffusers: (a) Channel or Wedge, (b) Airfoil.

2.5 Combustor

The role of the combustor is to burn the air-fuel mixture and to deliver a uniform temperature of hot gases to the turbine [24]. The major challenge in designing an effective combustor is maximizing combustion efficiency while minimizing pressure loss across the component [24]. In a standard turbojet configuration, all of the airflow passes through the combustor. Some engine variations, such as a turbofan, will drive a layer of air outside of the engine in order to increase propulsive efficiency. Even though all of the air in the turbojet goes through the combustor, only about a quarter of the air is burned [25]. The rest of the air is used for cooling the combustion products to temperatures that the turbine can withstand. Air flow through the combustor is distributed across three zones: (1) the Primary Zone, (2) the Secondary Zone, and (3) the Dilution Zone. These regions are depicted in an illustration of an annular combustor in Figure 29. The process of determining how much air should be allotted to each of these zones is known as *air partitioning*.

The primary zone is responsible for flame holding and combustion stability. In the primary zone, the fuel is introduced to the air. Hot combustion products recir-

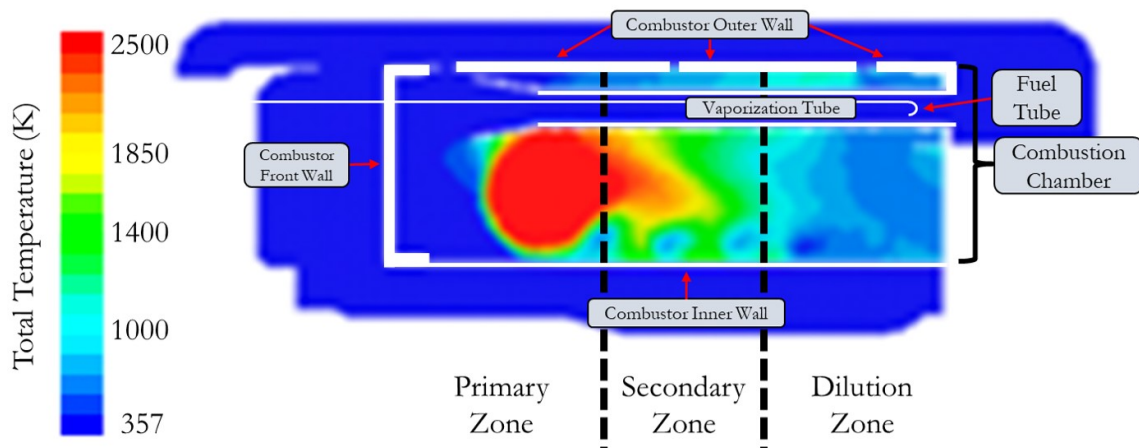


Figure 29. Illustration of air partitioning in an annular, microturbine combustor. Adapted from Gieras and Stańkowski [13].

culate in the primary zone and cause the fuel-air mixture to combust. This process of continual combustion is known as *flame-holding*. Gieras and Stańkowski studied the aerodynamics of cold flow passing through a microturbine combustor [13]. The combustor geometry shown in Figure 29 is similar to the combustors of the engines tested in this research. Therefore, the results of Gieras and Stańkowski aid in understanding microturbine combustor performance. Based on cold flow aerodynamics alone, a comparable microturbine combustor would experience a total pressure drop over the burner of 10%.

Figure 30 shows color contours of velocity magnitude overlaid on velocity streamlines. Streamlines indicate the path of the flow. For reference, the bulk flow is moving from left (engine front) to right (engine back). However, there are some notable flow features. First, the fuel air mixture is seen to exit the fuel tube with fast enough velocity that it impinges on the front wall of the combustor. After impingement, the flow slows and enters a recirculation zone. This flow feature is identified as the flame holding location in Figure 30. As indicated by the color contours of velocity

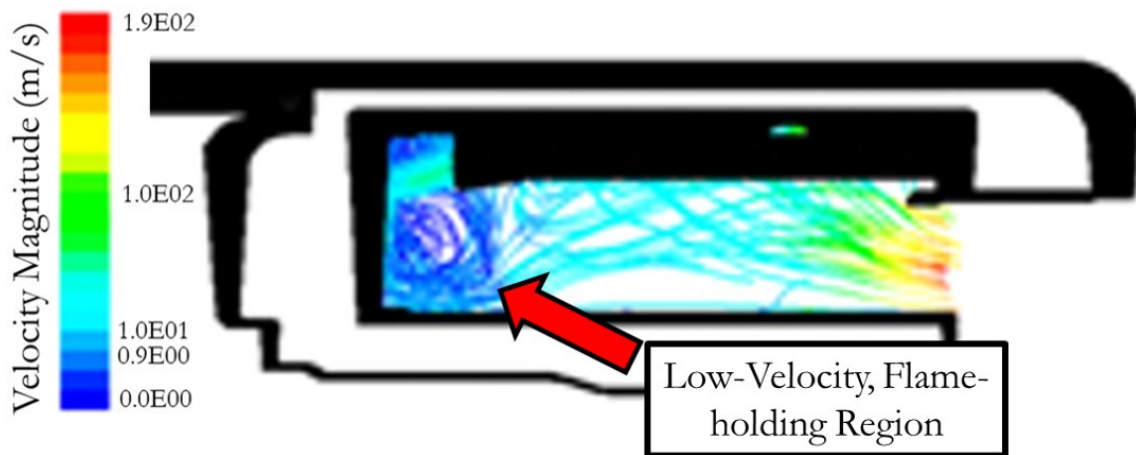


Figure 30. Streamlines through the combustor with color contours of velocity magnitude indicating flame-holding region. Adapted from Gieras and Stańkowski [13].

magnitude, the speeds in this recirculation zone are significantly lower than the rest of the flowfield. The recirculation of hot combustion products and the slow speeds in this region make it an effective flameholder design for the engine.

The secondary zone is responsible for ensuring the fuel is completely combusted. *Residence time* describes how long a fuel particle is inside the combustor. A long secondary zone allows for a longer residence time which raises combustion efficiency but adds length and weight to the engine. This presents a critical design trade-off between size, weight, and efficiency. Seen in Figure 29, the secondary zone is still hot, but not as hot as the primary zone. The cooler temperature in the secondary zone is due to the relatively cool temperature of the air introduced to complete the combustion reaction.

Finally, the dilution zone is responsible for reducing the temperature of the combustion products to a temperature suitable for the turbine. This zone is identified in Figure 29 as the cool blue region downstream of the secondary zone. While in the dilution zone, the flow must also be transitioned into a cross sectional area appropriate for the inlet of the turbine nozzle guide vanes.

2.5.1 Equivalence Ratio & Fuel Fraction.

A parameter known as the Equivalence Ratio, Φ , is used to quantify whether a combustion process is burning fuel lean or fuel rich. The equivalence ratio is given by Equation 47 [41]:

$$\Phi = \frac{(A/F)_{stoic}}{(A/F)} \quad (47)$$

Equivalence ratios of $\Phi = 1$ indicate that reactants are present in stoichiometric proportions while equivalence ratios of $\Phi > 1$ and $\Phi < 1$ indicate rich and lean combustion, respectively. The combustion process is highly dependent on equivalence

ratio. The species constituting the exhaust gases and the amount of energy released by the combustion reaction are both dependent on the availability of the reactants [41]. Since the amount of energy released by the fuel into the fluid is dependent on the equivalence ratio, the temperature of the products is also a result of this proportion.

When considering the engine as a whole, the fuel fraction, defined by Equation 58, is a useful term for estimating combustor performance. The total temperature of the gas leaving the combustor can be predicted using Equation 49.

$$f = \frac{\dot{m}_f}{\dot{m}_0} \quad (48)$$

$$h_{t4} = \frac{\eta_b f h_{PR} + h_{t3}}{1 + f} \quad (49)$$

While this represents a useful method of modeling combustor performance, it has two significant flaws. First, it requires combustor efficiency to be known or assumed. This is a difficult parameter to determine for microturbines. According to experts at SERL, $\eta_b = 0.95$ is an appropriate assumption for the size and style combustor employed in microturbine engines. Second, this method provides an estimate of the average temperature. In reality, significant thermal distortion exists at the exit of the combustor. Figure 31 provides computation results of a cross section of a thermally distorted flow near the exit of the combustor assuming uniform flame holding. This represents a best-case thermal distortion for this style combustor.

2.5.2 Thermal Distortion.

The non-uniformity of the fluid's temperature profile is referred to as thermal distortion. There are multiple ways to measure thermal distortion depending on what information is desired. The Society of Automobile Engineers (SAE) developed a list of parameters used to standardize how thermal distortion is quantified. These param-

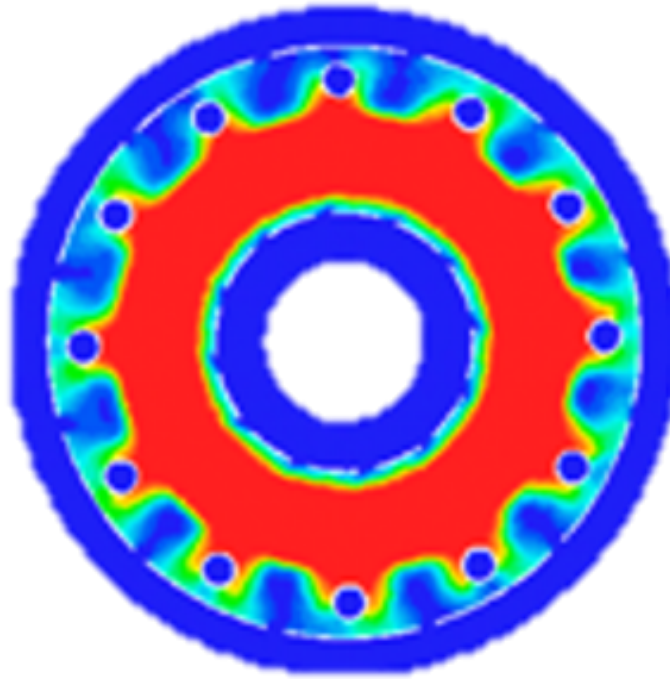


Figure 31. Axial view of a cross section of the flow within the combustor showing radial thermal distortion. Adapted from Gieras and Stańkowski [13].

eters give an indication of how the temperature varies radially or circumferentially and reflects the temperature of the ‘hot spots’ of the flow relative to the average temperature at that axial position. When experimental data is gathered for a flow’s thermal distortion, a thermocouple rake is typically employed to gather temperature data at a variety of locations. These rakes allow for measurements to be taken at multiple radial and circumferential positions at one time.

Since thermal distortion calculations for engines are most commonly made on flows with a circular cross sectional area, it is convenient to consider the data in a polar coordinate frame. The Circumferential Distortion Intensity (CDI) provides a measure of thermal variation that occurs at a constant radius away from the center of the flow. CDI can be calculated using Equation 50 [38]:

$$CDI_i = \frac{TAVHI_i - TAV_i}{TAV_i} \quad (50)$$

Where the TAV_i is the average temperature of the i -th ring, and $TAVHI_i$ represents the average of the temperatures exceeding TAV_i in the i -th ring. In other words, $TAVHI_i$, represents the average temperature of the hot spots located on the i -th ring.

The Circumferential Distortion Coefficient is a metric associated with the profile as a whole and is given by the average of all CDI values for the profile as shown in Equation 51 [38]:

$$CDC = \frac{1}{i} \sum_{i=1}^n CDI_i \quad (51)$$

A third metric used for thermal distortion analysis is the Radial Distortion Intensity (RDI) which is a measure of how the average temperature at a given radius (for all angles) compares to the average temperature of the entire thermal profile at that instance. RDI is given by Equation 52 [38]:

$$RDI_i = \frac{TAV_i - TFAV}{TFAV} \quad (52)$$

Where TFAV is the average temperature of the face/profile. A final metric used to discuss the variations in a thermal profile is the pattern factor, PF. This metric, given by Equation 53 [9]:

$$PF = \frac{T_{max} - T_{exit}}{T_{exit} - T_{inlet}} \quad (53)$$

where T_{max} is the maximum local temperature and T_{inlet} and T_{exit} the average temperatures at the inlet and exit planes, respectively.

2.6 Turbine

The turbine's role in a gas-turbine engine is to convert kinetic energy from the flow into shaft power that can be used to drive the compressor [24]. There are two design challenges associated with the turbine. The first is the efficient transformation of kinetic energy of the flow into shaft power. The second is withstanding the harsh environment created by the combustion exhaust gases. Like the compressor, the work done by the turbine can be described by the Euler Pump Equations. Therefore, the turbine adiabatic stage efficiency is calculated as the ratio of the useful work generated by the turbine to the work extracted from the flow (the ideal output). The equation for the adiabatic stage efficiency of a turbine is given by Equation 54. A useful simplification that can be made when the fluid behaves as calorically perfect gas [24]. The result of this simplification is given by Equation 55:

$$\eta_t \equiv \frac{W}{W_i} = \frac{h_{t4} - h_{t5}}{h_{t4} - h_{t5i}} \xrightarrow{CPG} \eta_t = \frac{c_p (T_{t4} - T_{t5})}{c_p (T_{t4} - T_{t5i})} = \frac{1 - T_{t5}/T_{t4}}{1 - (P_{t5}/P_{t4})^{(\gamma-1)/\gamma}} \quad (54)$$

$$\boxed{\eta_t = \frac{1 - \tau_t}{1 - \pi_t^{(\gamma-1)/\gamma}}} \quad (55)$$

The turbine polytropic efficiency can be calculated using the same approach that was shown for the compressor polytropic efficiency in Section 2.4. The turbine polytropic efficiency is given by Equation 56.

$$e_t \equiv \frac{(dh_t)_{act.}}{(dh_t)_{id.}} \longrightarrow \boxed{e_t = \frac{\gamma}{\gamma - 1} \frac{\ln(T_{t5}/T_{t4})}{\ln(P_{t5}/P_{t4})}} \quad (56)$$

Conservation of work can be used to relate the compressor work to the turbine work. Ideally, the work done by the compressor is equivalent to the work extracted

Table 2. Typical Ranges for Turbine Design Parameters.

Design Parameter	Range
Maximum AN ²	4-5x10 ¹⁰ in ² -RPM 26-32x10 ¹⁰ cm ² -RPM
Stage Loading Coefficient, ψ	1.4-2.0
Exit Mach Number	0.4-0.5
Exit Swirl Angle	0-40°

by the turbine. Due to bearing losses, the work done by the compressor is slightly lower than the work generated by the turbine. The relationship between the two components is described by Equation 76. According to Rodgers, the losses of turbocharger fluid film bearings sized for this application are on the order of 1kW at speeds of 100kRPM, and the losses of comparable ball bearings are less than 0.5kW [36]. Knowing the the turbine work is on the order of 100kW for the microturbine turbojets tested in this work, this results in a conservative estimate of mechanical efficiency of $\eta_m = 0.99$.

$$w_t = \frac{w_c}{\eta_m} \qquad w_t = h_{t4} - h_{t5} \qquad (57)$$

Ranges for several important turbine design parameters are included in Table 2. Dimensionless products discussed in Section 2.4.5, such as the stage loading coefficient, also apply to the turbine. Similar to the dimensionless analysis of the compressor, $n_s d_s$ diagrams are a useful tool in predicting turbine performance. Figure 32 relates the turbine adiabatic efficiency to specific speed and specific diameter with contours of maximum efficiency and of average efficiency.

In Section 2.5, the major function of the dilution zone shown to be cooling the combustion products to a temperature suitable for the turbine. However, turbine inlet temperature (TIT) does not appear explicitly as a design parameter in Table 2. This is because the TIT is rolled into the AN² parameter.

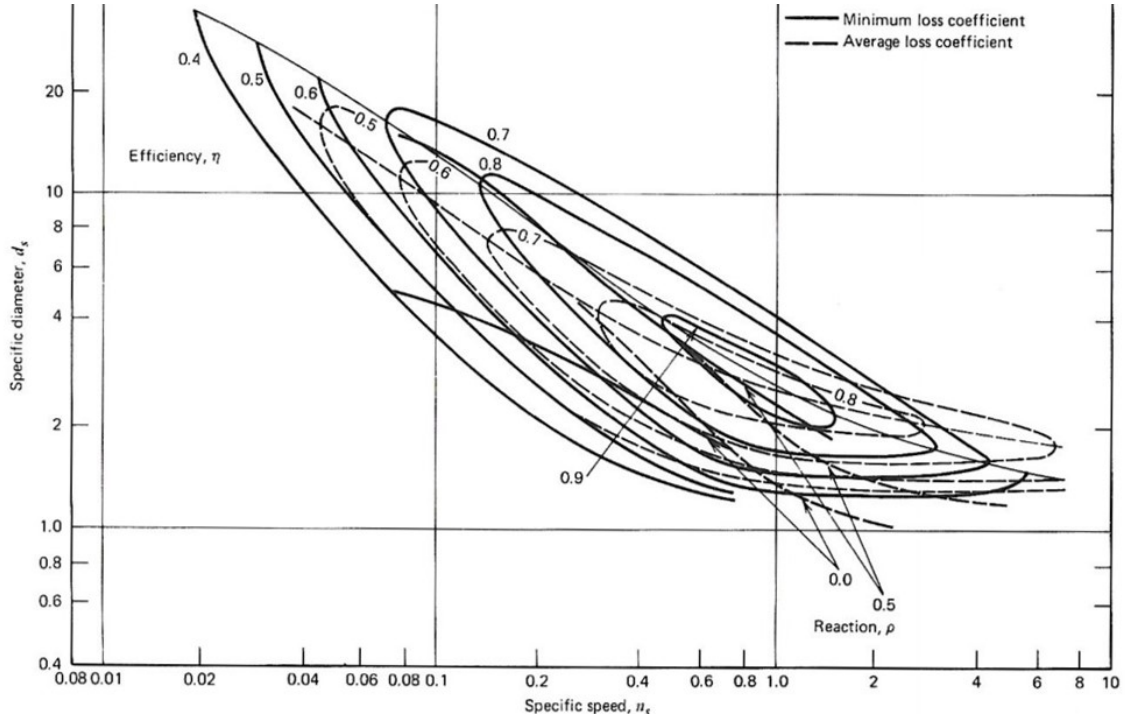


Figure 32. Turbine adiabatic efficiency related to specific speed and specific diameter [2]. Solid lines indicate maximum possible efficiency. Dashed lines indicate average efficiency.

AN^2 represents the allowable airfoil material specific strength [25]. AN^2 is dependent on the airfoil taper ratio, A_t/A_h , and the specific strength of the material, σ/ρ . As shown in Figure 33a, A_t represents the cross-sectional area at the tip of the airfoil. Likewise, A_h is the cross-sectional area at the hub. The specific strength is a material property dependent on temperature. This relationship between specific strength and temperature for several typical turbine materials is shown in Figure 33b.

The inverse relationship between temperature and specific strength is testament to the importance of sound combustor design. Without proper air-partitioning routing cool air to the dilution zone, the specific strength of the turbine would reduce, as would the maximum allowable stresses in the turbine. AN^2 is given by Equation:

$$AN^2 = \frac{3600}{\pi (1 + A_t/A_h)} \frac{\sigma_c}{\rho} \quad (58)$$

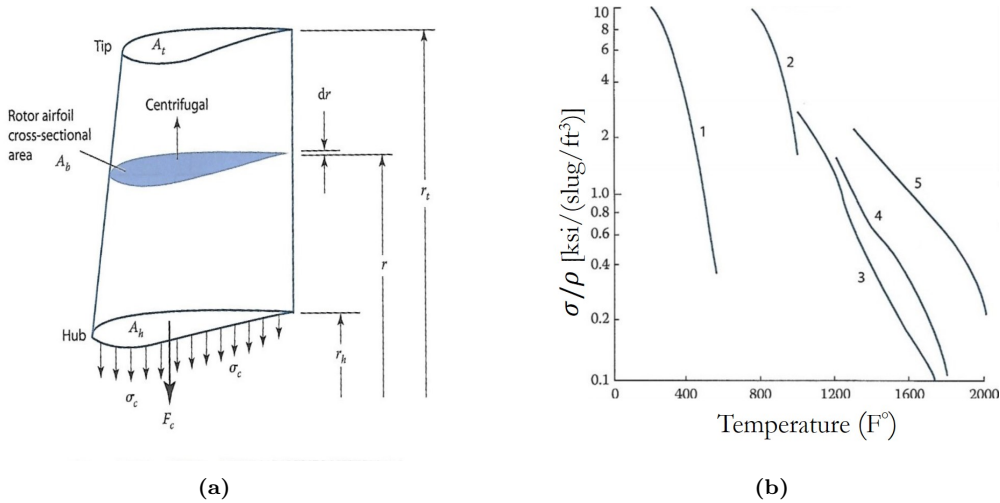


Figure 33. Turbine Rotors (a) Airfoil Nomenclature, (b) Strength-to-weight ratio vs. temperature for typical turbine materials. Materials: (1) Al alloy, (2) Ti alloy, (3) Wrought Ni alloy, (4) High-strength Ni alloy, (5) Single-crystal superalloy. Ref: [25].

When simply referring to the material property, σ/ρ is used to represent the specific strength. When referring to the ratio of the actual stress place on the airfoil to the material density, σ_c/ρ is used to represent the specific stress. To calculate the maximum allowable AN^2 , the material property for specific strength is used in Equation 58. To calculate the actual AN^2 experienced by the rotor during operation, the specific stress is used in place of specific strength.

2.7 Engine Performance

Because each engine is sized differently, it important that performance be normalized to facilitate useful comparisons. The two primary engine performance metrics are thrust and fuel consumption. Several normalizations of thrust exist to account for different design criteria. Three normalizations of thrust are used in this research: thrust to weight ratio (T/W), thrust per frontal area (T/A), and specific thrust (F/\dot{m}_0). Every discipline of aeronautical engineering seeks to minimize weight while maintaining performance, T/W reflects this pursuit. Higher T/W equates to aircrafts capable of higher performance or larger payloads. The second normalization, T/A,

is a result of drag and space constraints. For high speed vehicles, thrust per frontal area is a driving performance metrics due to the dominance of form drag in this flight condition. In 2003, Hamilton Sundstrand collected and published data on expendable turbojet engines [16]. The T/A data from that research is provided in Figure 34. This information provides a benchmark of performance required for military-grade expendable turbojets that proves to be a useful point for comparison in Section 4.1.1.

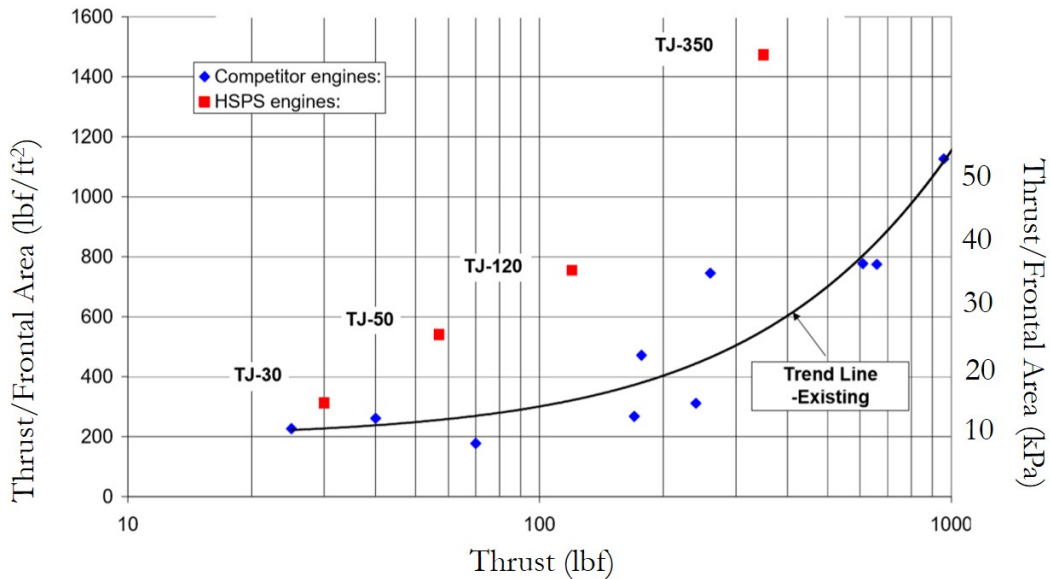


Figure 34. Thrust per frontal area for military-grade expendable turbojets [16]. Published by Hamilton Sundstrand after releasing their TJ-50 for the ADM-160 MALD.

The final thrust normalization is specific thrust, F/\dot{m}_0 . Since turbojet engines generate thrust by creating a momentum difference, normalizing the thrust by mass flow shows how effectively the engine accelerates the flow. Drawing upon Newton’s Second Law, this parameter is an indicator of the difference in the freestream velocity and the exhausting jet velocity. This is reinforced by inspecting the units associated with specific thrust and realizing that they are equivalent to velocity units as shown in Equation 59.

$$\text{Specific Thrust Units: } \frac{N}{kg/s} = \frac{\left(kg \frac{m}{s^2}\right)}{kg/s} = \boxed{\frac{m}{s}} \quad (59)$$

This metric is particularly useful during the engine design process and is typically used alongside the specific fuel consumption which represents the fuel consumption normalized by thrust as shown in Equation 60.

$$S = \frac{\dot{m}_f}{F} \quad (60)$$

A common technique for initiating engine design is to refer to a carpet plot that shows how various engine parameters affect engine performance. For a turbojet, a carpet plot will typically compare F/\dot{m}_0 , S , OPR , and TIT . A sample carpet plot is shown in Figure 35. Generating these carpet plots requires component efficiency to be known or assumed.

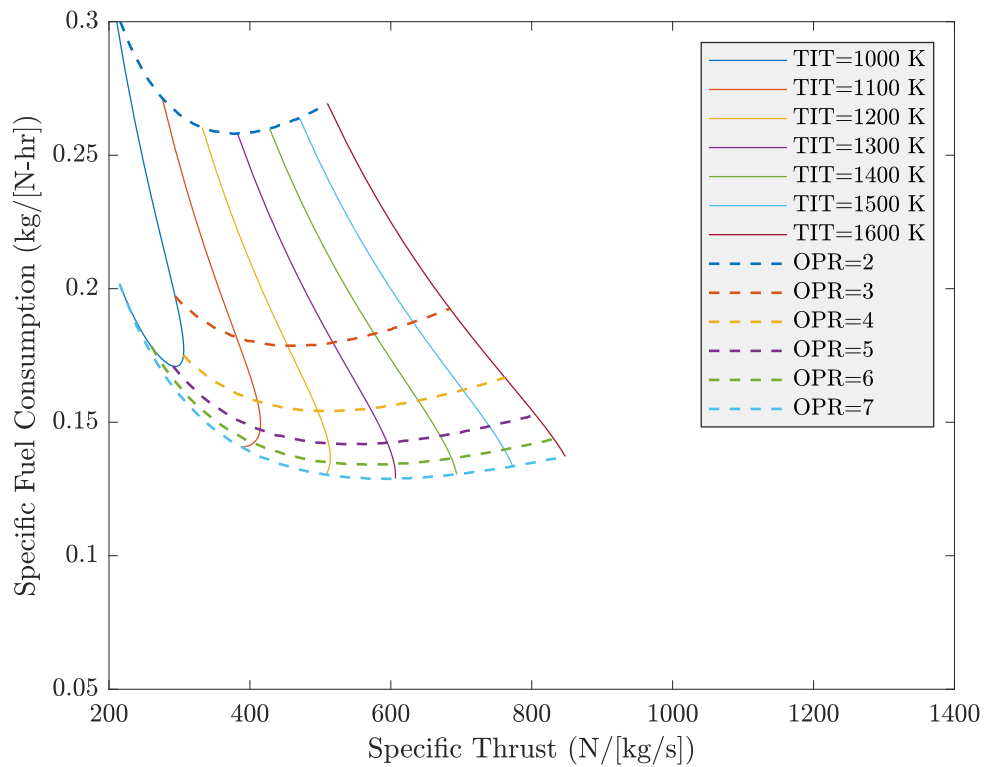


Figure 35. Carpet Plot showing turbojet design space.

2.8 Instrumentation

In order to conduct meaningful analysis of experimental data, proper measurement techniques must be employed during experimentation. As acknowledged throughout the rest of this chapter, the key data that must be measured in order to analyze an engine are: (1) thrust, (2) total and static temperature temperatures, and (3) total and static pressures. This section contains a review of common instrumentation techniques for each of these measurements.

2.8.1 Thrust Stand Fundamentals.

It is necessary to calibrate the load cell before each test to ensure accurate thrust measurements. When discussing thrust stand calibration, tare is defined as the difference between the measured load and the applied load [37]. Low tare does not imply low uncertainty. If the tare is repeatable, accurate thrust measurements can be calibrated to indicate the applied load with low uncertainty. The tare forces causing deviation of the measured load from the applied load can be identified as three separate groups: (1) deflection tare, (2) interaction tare, and (3) gravity tare [37]. Gravity tare deals with accounting for variable engine weight and is generally only an issue for rockets and for vertical thrust stands. Since this research is concerned with turbojets on a horizontal thrust stand, gravity tare will not be further discussed.

Deflection tare includes all forces that arise from bending of wires and hoses that connect the engine to the ground. Ideally, only deflection in the load cell would occur during engine testing. In this case, the load cell would experience the full thrust force, deflect appropriately, and measure the applied load accurately. In reality, the wires and hoses that connect the engine to fuel, control units, batteries, measurement hardware, etc. will also deflect and provided reactionary forces. These reactionary loads are the deflection tare forces. Load cells operate on the principle that a given load will

cause a repeatable deflection and are able to make very accurate measurements. If the deflections in wiring and other engine connections are repeatable, like a load cell, then they can be easily accounted for via calibration. Issues arise when the deflection is not repeatable. For the purpose of this discussion, hosing refers to plumbing, wires, sensors or any other connections (not including the thrust stand structure) between the engine and the ground. Runyan identifies four design considerations relevant to making deflection tare accountable:

1. Flexible hosing will produce a smaller reactionary force due to bending. However, since it will move, there may be friction between the hose and other structures. This friction force will not be repeatable. Rigid hosing should be used when high accuracy thrust measurements are required [37].
2. All hosing should be anchored on the floating frame and the ground structure. Ideally, these anchors are made in the same plane and orthogonal to the thrust [37]. Using coplanar anchors is not necessary for single component stands.
3. Movable joints just as ball joints introduce non-repeatable friction and should be used with discretion [37].
4. The floating frame should have sufficient space to move without contacting any other structures. Contact made while the floating frame is partially deflected will create a non-linearity in the calibration and will be difficult to account for. Ensure that the adequate clearance is given for the floating frame to travel through its range of motion without making contact with another object. Dirt and other objects can unsuspectingly aggravate this issue [37].

While well secured rigid piping may be preferable, it is not realistic for the research timeline or the size of engine being tested. The existing thrust stand has points for

the hosing to be anchored on both sides. However, these are not always orthogonal to the thrust axis. This was not considered to be an issue since all hosing was flexible tube or wires, contributing only small deflection tares. Slip that occurs in thrust stand hosing and components manifests itself in the thrust measurement as tare hysteresis [37]. When deflection tare is unaccounted for, the uncertainty of the thrust measurement increases.

The other major category of tare forces relevant for this experiment is the interaction tare. These forces are a result of the reactionary forces of the thrust stand structure. The thrust stand is composed of a floating frame which holds the engine and allows for movement so that the load cell can resist and read the thrust force. Ideally, the structure imparts no forces along the thrust axis. Generally, a thrust stand will have a series of flexures that separate the floating frame from the ground structure. In the case of single component stands, a rail or bearing can be used instead of flexures as is the case for the existing thrust stand at SERL. The most significant interaction tare that may exist for an air-bearing thrust stand is due to the alignment of the load cell. If there is a yaw between the path of motion for the air-bearings and the load cell, an interaction tare may occur due to this offset. Similarly, misalignment between the thrust axis and the path of motion of the air-bearings may induce an interaction tare.

2.8.2 Temperature: Thermocouples.

Total temperature is a measurement of the total kinetic energy of the molecules is a combination of both molecular speed (static temperature) and bulk flow velocity [21]. While there are a multitude of instrumentation techniques available to conduct temperature measurements, the thermocouple has historically been (and remains) the industry standard for measuring internal engine temperatures [48]. Thermocouples

measure temperature by relying on the Seebeck Effect, a thermo-electric phenomenon discovered by Thomas Johann Seebeck in 1822, in which two wires of dissimilar metals will produce a voltage potential when connected and heated at their junction when kept in an open circuit. The magnitude of this voltage is proportional to the difference in temperature of the connected, hot junction and the open, cold junction. The proportional constant used in this relationship is known as the Seebeck Coefficient. The Seebeck Coefficient and temperature range over which these instruments can be employed depend on the metals used. Furthermore, it is important to note that this thermoelectric effect is only dependent on the temperatures at the junctions. Temperatures along the wire do not directly affect the Seebeck Voltage. However, as will be shown later in this section, temperature variations along the wire will play a role in skewing the steady state temperature at the junction.

There are several different thermocouple types and configurations which should be understood before selecting a thermocouple for a given application. The three types predominantly used are the (1) exposed, (2) grounded, and (3) ungrounded junctions [48], shown in Figure 36.

Each configuration has different characteristics making them appropriate for different tasks. The exposed junction leaves the wire junction exposed directly to the medium in which it is measuring. Exposed junctions are desirable because they allow for the best accuracy and the best resolution of transient temperature fluctuations.

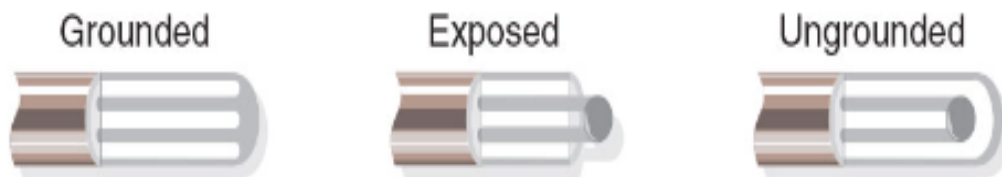


Figure 36. Typical thermocouple junction configurations [30].

However, they are fragile and can easily be damaged by high velocity flows. This generally makes exposed thermocouples ill-suited for use in engine instrumentation. The remaining junction configurations (grounded and ungrounded) are both shielded junctions. Each has a protective sheath that separates the junction from the medium in which it is immersed. This increases the durability of the thermocouple, but negatively impacts the thermocouple's response to transient temperatures [31]. In the harsh engine environment, shielding of the thermocouple is vital to mitigate the chances of FOD being released within the engine and damaging turbomachinery components downstream. There are two significant differences between the grounded and ungrounded thermocouples. The first is the response time. The grounded thermocouple has a metal connection between the sheath and the junction which allows for rapid conductive heat transfer to the junction, facilitating a faster response time than the ungrounded, though still significantly slower than the exposed thermocouple [48]. Thermocouple response time is dependent on size and configuration. While reviewing instruments for this research, response times for exposed thermocouples were on the order of 0.25 seconds and response times for sheathed thermocouples were on the order of 2.25 seconds as shown in Figure 37 [31].

The disadvantage of the grounded thermocouple is that the shielding becomes part of the thermoelectric circuit. By removing the metal connection between the sheath and the junction and by filling the void with an insulator, the thermocouple circuit becomes electrically insulated from the shielding. These ungrounded thermocouples are useful when dealing with ionized flows. Heat is still conducted through this powder, though at a slower rate.

The thermocouple *Type* refers to the metals used in the circuit, known as the thermometals [48]. The most common and inexpensive thermocouple types (J, K, T, E, and N) while thermocouples capable of finer precision and of withstanding higher

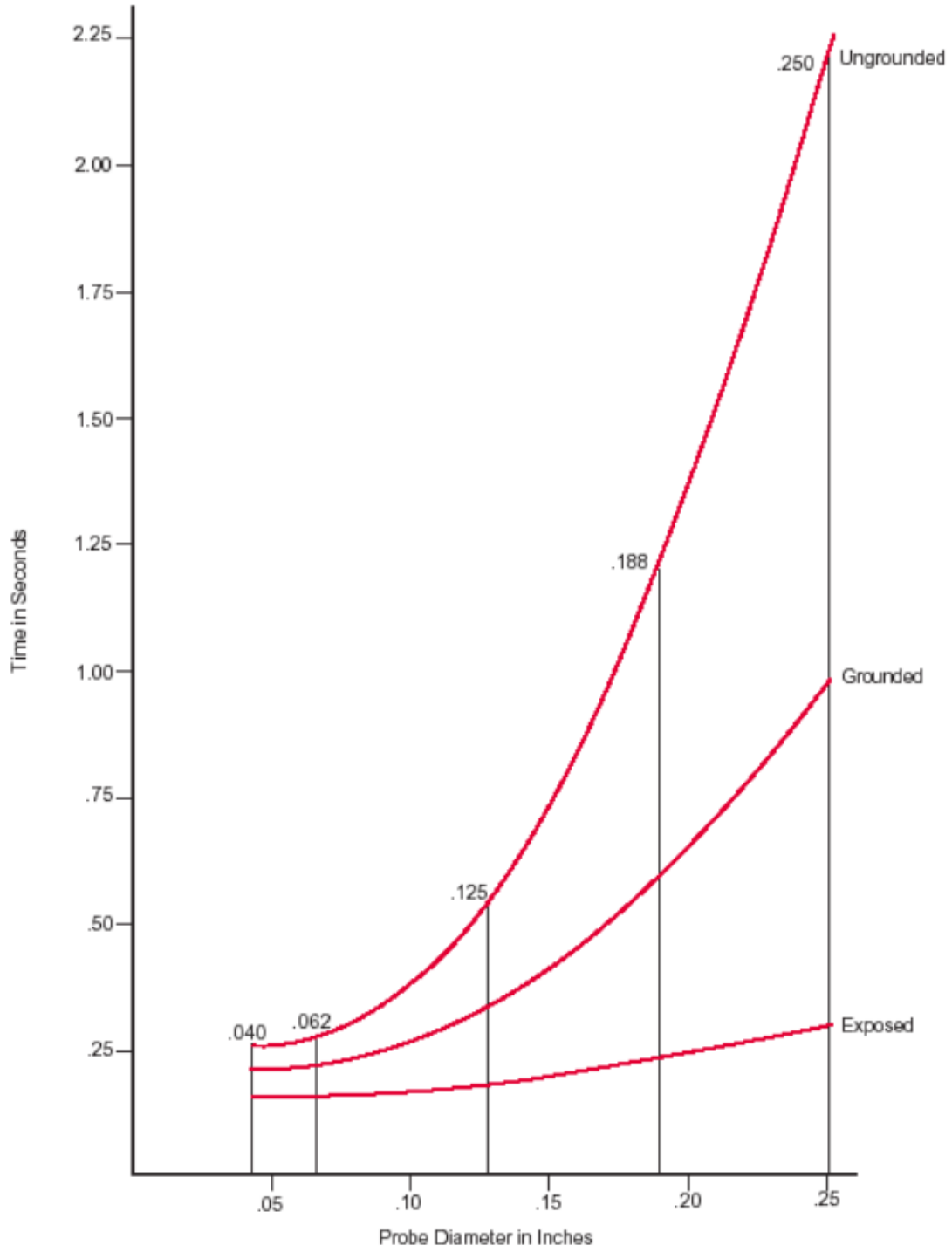


Figure 37. Thermocouple response time for variations in junction type and size. Measurements made in water [31].

temperatures are made from noble metals or specialized alloys (R, S, C, and GB-Type thermocouples). While significantly more expensive, the noble metal thermocouples are able to withstand temperatures in excess of 3,000 °R [48]. The calibration and thermal limits of some common thermocouples are listed in Table 3.

Table 3. Typical thermocouple calibrations and thermal ranges based on type. Data from Ref. [30]

Calibration	Temperature Range	Standard Accuracy
J	0 to 750	0.75% or 2.2
K	-200 to 1250	0.75% or 2.2
E	-200 to 900	0.5% or 1.7
T	-250 to 350	0.75% or 1.0

2.8.3 Thermocouple Corrections.

While thermocouples provide a compact, robust, and reliable way to measure temperature within an engine, their use is plagued by uncertainty and errors like any measurement technique. In writing the SAE standard for gas turbine engine measurements in 1984, Williamson and Stanforth identify two issues related to the use of thermocouples. The first is the calibration of the Seebeck Effect to the temperature difference across the thermocouple [48]. Today, it is relatively inexpensive to obtain thermocouples for a variety of configurations and calibrations (types) from instrument manufacturers, so this is not as much an issue for the research engineer. The second issue is that the temperature of the thermocouple junction is not necessarily (the authors note that it is commonly not) the temperature of the gas in which it is immersed. Rather, the temperature of the thermocouple junction is that at which a steady state of heat transfer between the junction and its surroundings is achieved [48]. The authors identify six sources of heat transfer that influence thermocouple junction temperature that are illustrated in Figure 38 and enumerated below:

1. q_1 : Convective heat transfer from the gas to the junction
2. q_2 : Net radiative heat transfer between the walls containing the medium and the junction
3. q_3 : Conductive heat transfer along the wires
4. q_4 : Transformation of kinetic energy to static temperature in the boundary layer of the probe
5. q_5 : Heat transfer due to chemical reactions occurring between the probe and the flow
6. q_6 : Radiative heat transfer from the gas to the junction

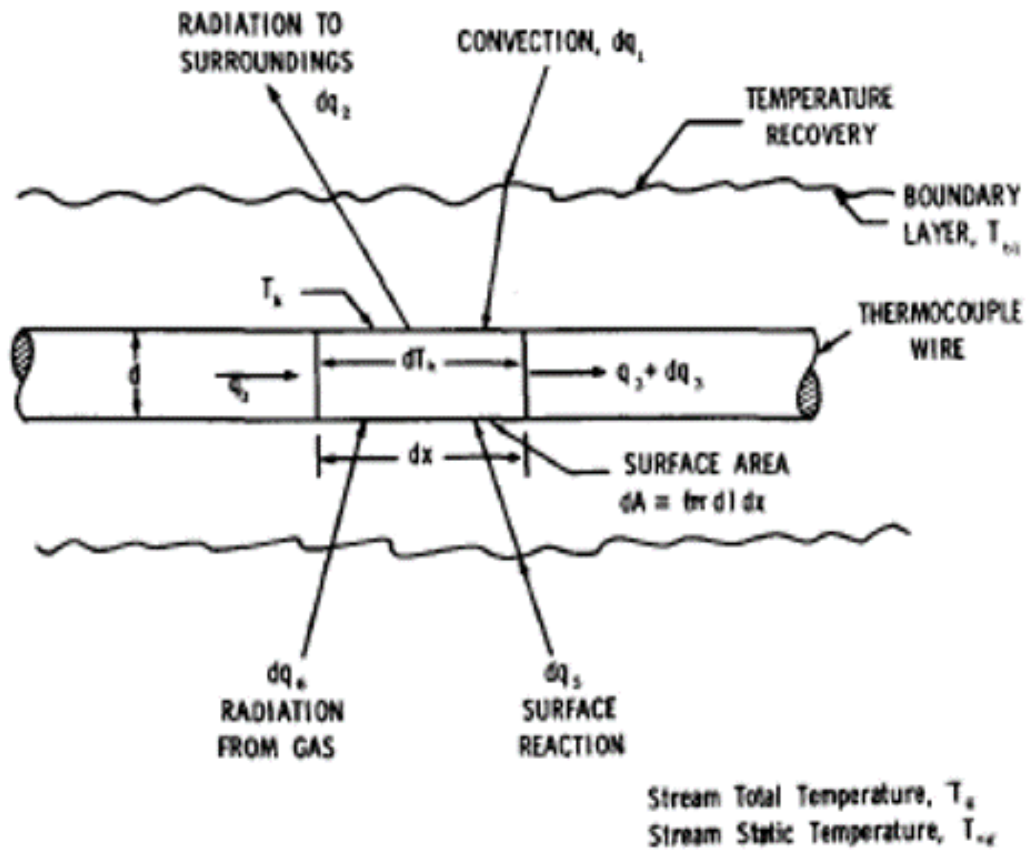


Figure 38. Six sources of heat transfer along a thermocouple. [48]

Upon inspecting this list, it becomes apparent that these issues, while prevalent in all gas turbine engines, are exasperated in microturbines. For example, due to the compact size and small flow passages associated with these engines, the size of boundary layers relative to the entire flow becomes larger as the passage becomes smaller. At the same time, closer proximity to the engine casing will increase conductive and convective heat transfer from the junction to the cool engine casing.

Of the six heat transfer sources present, three have the biggest effect on skewing measurements in high-temperature, high-velocity flow: (1) viscous dissipation or aerodynamic heating, (2) conduction along the thermocouple wires, and (3) radiation from nearby bodies [40] [48]. The first source of error indicates that the thermocouple reading is neither the static nor total temperature, but some measurement in between. For low speed flow, such as the ambient condition and station three, the thermocouple measurement is assumed to be the total temperature. Sparrow suggests that a shielded thermocouple junction aids in reducing radiative heat transfer to the sensor [40].

Combustors are prone to patterning. Patterning describes the distortion and non-uniformity that is a result of uneven combustion across the cross section of the flow. Due to this distortion, it is difficult to produce a measurement at station 4 that is consistently representative of the global temperature at that station. In order to account for this patterning, it is common practice to add a rake of thermocouple probes to measure flow temperatures at a multitude of points throughout the turbine inlet. According to Walsh and Fletcher, incorporating enough thermocouples to accurately measure the average temperature exiting the combustor is impractical [44]. However, calculating the average temperature based on a number of finite point measurements is extremely sensitive to probe location [44]. The standard thermocouple rake for measuring distorted flows consists of probes at eight circumferential loca-

tions and at three to five radial locations [38] [44]. In reference [10], the sensitivity of thermal distortion measurements to the number of probe locations was investigated. This work was completed using results from CFD analysis of several nozzles modeled downstream of a combustor and turbine. As shown in Figure 39, the calculations regarding the state of the flow are sensitive to probe location and quantity until over 1000 probes are introduced to the flow.

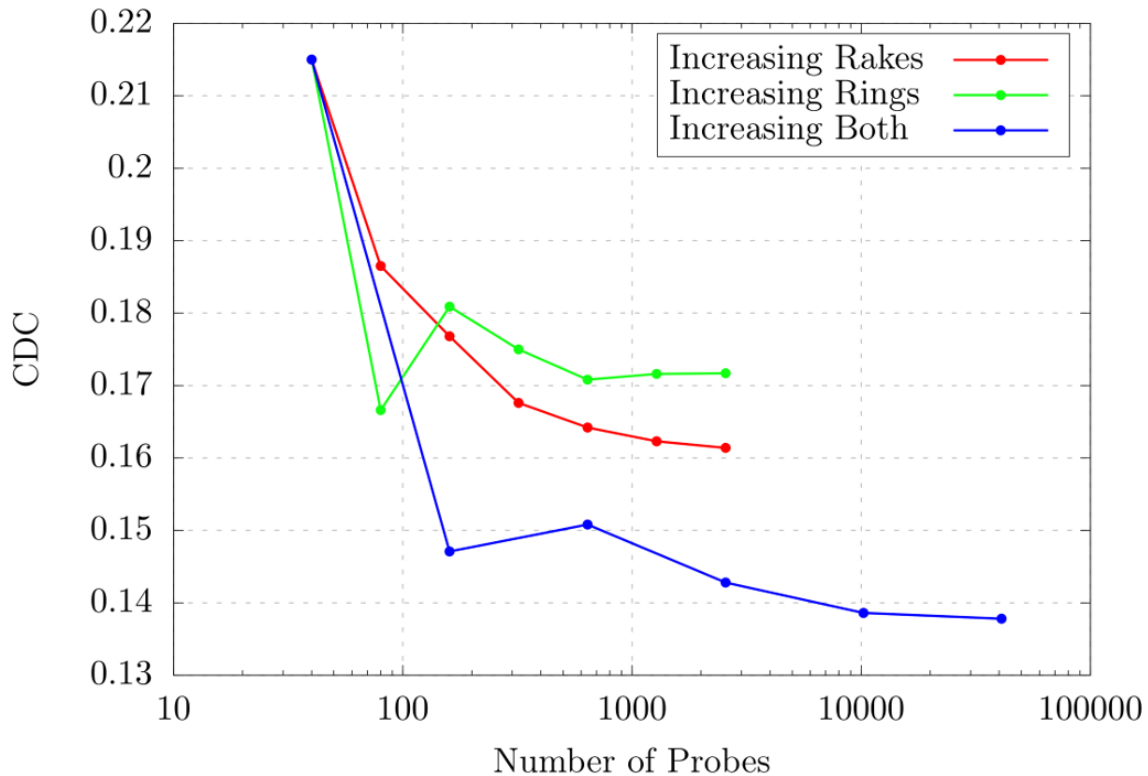


Figure 39. Thermal distortion sensitivity to number and location of probes [10].

2.8.4 Kiel Tube.

In 1935, Kiel presented the total-head meter to the National Advisory Committee for Aeronautics (NACA) as a more suitable means for determination of dynamic pressures along a wing. Kiel showed that his device, presented as the total-head meter but now known commonly as the Kiel Tube, allowed for the measurement of

total pressure while exposed to a variety of yaw angles that could be experienced in flight. His proposed design is provided in Figure 40. He proved that this device was insensitive to flow changes up to 45° of yaw and provided correct total pressure readings throughout this range. A notable design criteria that allowed for his device to sustain consistent and accurate reading across a wide range of yaw angles was the enclosure. Kiel described his device as a “venturi, housing a pitot tube” [19]. In his testing, he found that the reduction of flow passage area characteristic of a venturi tube allowed the flow to remain consistent and allowed for accurate total pressure reading by placing the pitot tube ahead of the throat of the venturi enclosure [19]. By comparing the original design proposed by Kiel, Figure 40, to a modern Kiel Tube, Figure 41, it is apparent that very little modification to this design has occurred since Kiel first presented it.

The success with which Kiel was able to measure total pressure values motivated similar design for the thermocouple. Thermocouples encased in Kiel Tubes have become the industry standard for empirical determination of total temperature values. Like in Kiel’s original total-head meter, Kiel Tube thermocouples are designed to stagnate the flow around the thermocouple junction to achieve a better total temperature reading. A diagram of a thermocouple shrouded with a Kiel Tube is provided in Figure 42.

Since the gas turbine has undergone continuous advancement since its creation, the technology has progressed so far that research and development teams seek to advance the current state of the art by component efficiencies of less than 1%. Bonham et al. point out that this drives the need for engine instrumentation to provide measurements with an uncertainty of less than 0.1% if they hope to calculate component efficiencies within 0.5% uncertainty [4]. In pursuing such low uncertainty, the group assessed current practices for empirical determination of total temperature within a

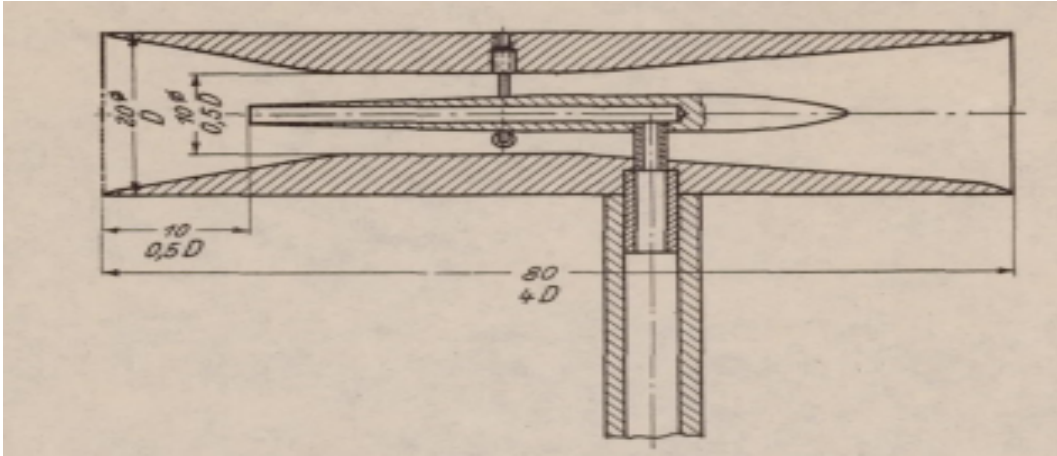


Figure 40. G. Kiel's proposed "total-head meter" [19].

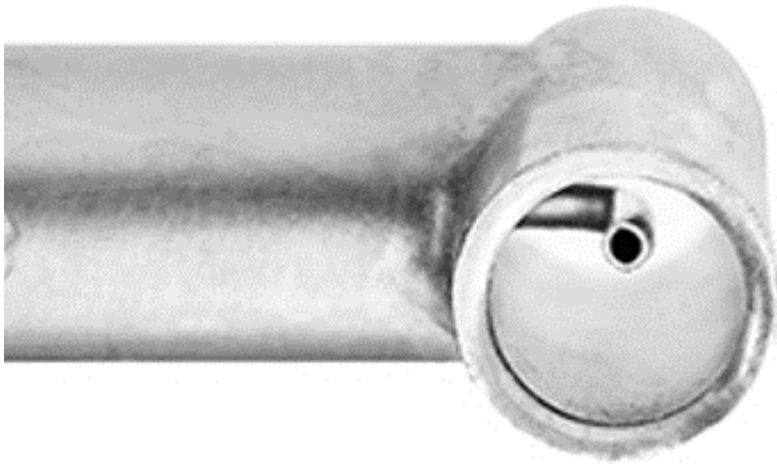


Figure 41. Modern Kiel Tube.

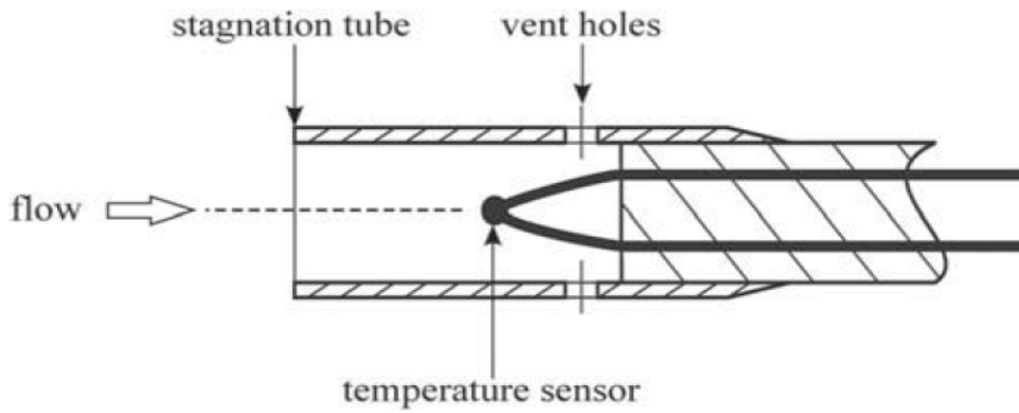


Figure 42. Kiel Tube Thermocouple [4].

flow. The group states that, while temperature recovery ratios are available to convert from a thermocouple's indicated temperature to the true total temperature, these correction factors are developed in the steady flow of controlled wind tunnels. The discrepancy between the steadiness of the calibration conditions and the unsteadiness of the experimental conditions results in the correction recovery ratios being an ineffective means of determining total temperature. The unsteadiness which renders the correction factors inappropriate for turbomachinery testing are a result of wakes shed from rotating turbomachinery. These wakes cause an unsteadiness in Mach Number and therefore in static temperature.

One of the primary contributors to thermocouple reading error is due to conduction from the sensing element through the rest of the instrumentation and surrounding materials. Bonham et al, propose that this conduction is the primary source of uncertainty that renders Kiel Tubes inaccurate when used in the unsteady flow downstream of turbomachinery. Bonham et al reviewed three types of probes for taking total temperature measurements: (1) the Kiel Tube thermocouple shown in Figure 42, (2) the Platinum Resistance Thermometer (PRT) Kiel, and (3) the Acrylic Platinum Resistance Thermometer Kiel. First assessing the Kiel thermocouple, the team illustrated how the unsteadiness of the flow downstream of turbomachinery compounds with the uncertainty of instrumentation to create significant issues in accurate and conclusive determination of component efficiency. This is due to the frequency at which wakes shed from a piece of rotating turbomachinery would pass through a given point downstream of the flow [4]. Since each wake is the result of the passing of a rotor blade, the blade passing frequency is the same, or at least an upper limit, on the frequency with which a wake could cross a probe. Therefore, in order for the thermocouple to indicate the transient effects of the unsteady flow, the blade passing frequency must be significantly less than $1/\tau$ where τ represents the thermocouple time constant [4].

For reference, the blade passing frequency of the JetCat P-200 at idle is excess of 10 kHz, and a typical thermocouple time constant is on the order of one second. This shows thermocouples to be severely insufficient at collecting the dynamic changes in temperature due to wake shedding downstream of the compressor. Consequentially, it is necessary to understand that even with perfectly certain instruments, there is an inherent uncertainty in measurements of flow downstream of turbomachinery due to insufficient sampling frequencies of available thermocouples. Measurements made within the engine will represent averaged values and will not necessarily resolve all transient behavior. This was acceptable for the goals of this research.

III. Experimental Methodology

Now that a framework for understanding this topic has been established, the methods used to investigate the research objectives can be presented. To review, the research objectives were: (1) to identify the potential performance of recreation-grade microturbine turbojets, (2) to quantify the effects of instrumentation on engine performance, and (3) to investigate same-make, same-model performance variation due to manufacturing variation.

Chapter III begins by providing the engine performance data published by each engine's manufacturer in Section 3.1. All testing was conducted at AFRL's Small Engines Research Lab (SERL). In Section 3.2, the facility used to house the test rig is discussed. Section 3.3 provides information regarding the thrust stands at SERL. The pre-existing thrust stand was deemed insufficient to finish testing and a replacement was installed. This section includes descriptions, calibration processes, and measurement accuracies for both systems. In Section 3.4, the instrumentation used to measure overall and component performance is discussed. Finally, the chapter will conclude with a description of how measurement uncertainty was quantified, Section 3.5.

3.1 Published Engine Performance

For this study, four similarly-sized engines were selected. Within this document, they are referred to as Engines A, B, C, and D (see the appendix for engine identification). Based on published values, all engines weighed between 14.3 - 30.4 N, had outer casing diameters of 110 - 133 mm, and produced 186 - 300 N of thrust. These and other notable engine specifications can be found in Tables 4 and 5.

Table 4. Engine Geometry.

Engine (-)	D _{max}		Length	
	(mm)	(in)	(mm)	(in)
A	132	5.20	355	13.98
B	110	4.33	258	10.16
C	133	5.23	390	15.35
D	130	5.12	401	15.79

As seen in Table 5, these engines all perform similarly enough to group them within the same class of engine. However, there are a few significant differences in performance. Engine A was designated as the baseline for this research due to SERL’s previous experience with this engine. Other engines were selected based on performance specifications that distinguished them from Engine A. Engine B was selected because of its high thrust-to-weight ratio (T/W) and low fuel consumption. The manufacturer of Engine B published thrust at the maximum speed but published fuel consumption at a slower speed. The manufacturers of the other engines published all data at the maximum speed. This complicates using published data to compare engines. Based on prior experience with Engine A, the published fuel consumption of Engine B was recognized to be surprisingly low, even at the slower speed. Engine C was selected because it offered a 43% increase in thrust for an engine that claimed the same size and weight as Engine A. Engine D was selected because it claimed a similar thrust, weight, and size, while having a 30% decrease in fuel consumption.

Table 5. Notable published engine specifications for the four turbojets tested. *Fuel Consumption Data for Engine B published at 105 kRPM.

Engine (-)	Thrust (N)	Weight (N)	T/W (-)	OPR (-)	Fuel Consumption (g/min)	N (kRPM)
A	210	24.8	8.47	4	525	112
B	186	14.3	13.0	N/A	392*	114
C	300	26.0	11.5	3.5	804	105
D	235	30.4	7.74	4.6	515	132

CT scans were taken of each engine in order to visualize and measure internal flow passages. Additionally, these images are useful for determining proper probe locations and for illustrating the two engine architectures tested. The first architecture is the standard, axial-flow turbojet. The flowpath for this style engine is overlaid on a CT scan of Engine B in Fig. 43. This engine layout consists of a centrifugal compressor, a combined vaned-to-dump diffuser, an axial-flow, annular combustor, and an axial-flow turbine. Engines A, B, and C were all standard, axial-flow turbojets. The only engine that was not designed with this layout was Engine D. CT scans of Engines A and C, both standard axial-flow engines are found in Fig. 44.

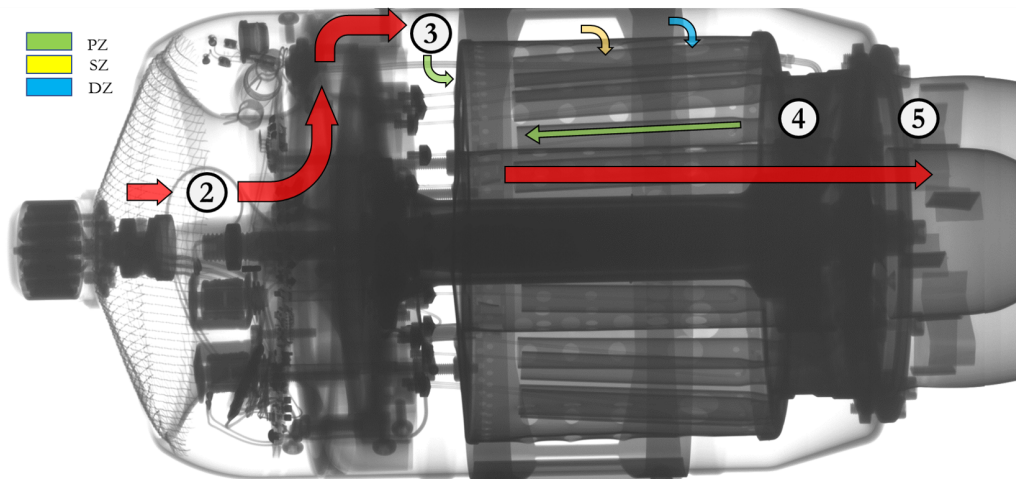


Figure 43. Flowpath through a standard, axial-flow turbojet. Flowpath overlaid on a CT scan of Engine B.

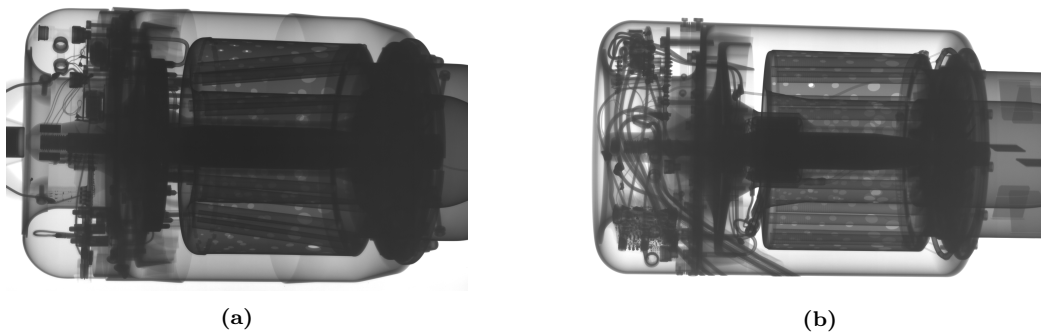


Figure 44. CT scans of Engines A and C, both standard, axial-flow turbojets.

Engine D is considered a reverse-flow turbojet. The flowpath through this style of engine is illustrated using a CT scan of Engine D in Fig. 45. In such engines, the flow downstream of the combustion chamber is turned 180° twice before passing through the turbine. In this layout, flame-holding occurs at the rear of the engine, and the exhaust products travel toward the front of the engine. The turbine is housed between the compressor and the combustor. This allows for a shorter shaft which can reduce reduce weight. The weight saved on the shaft is offset by the need to use a radial flow turbine in this configuration. The radial turbine is larger and heavier than the axial flow turbines used in Engines A, B, and C. Fig. 46 juxtaposes the axial-flow turbine of Engine B to the radial-flow turbine of Engine D.

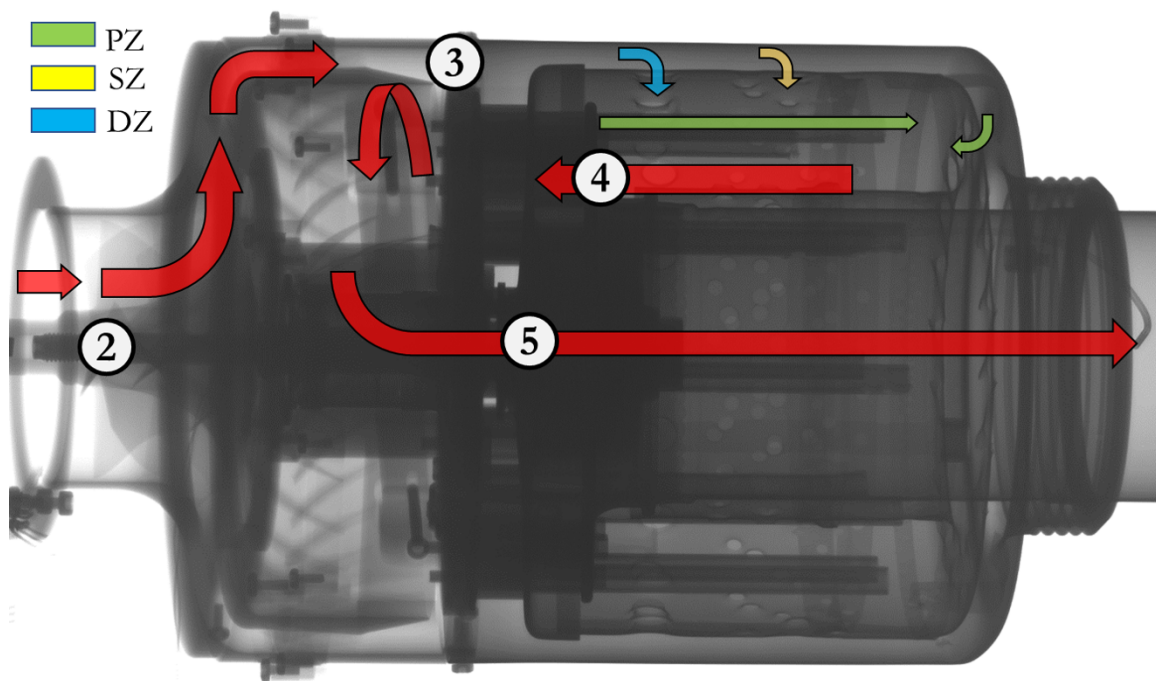


Figure 45. Flowpath through a reverse-flow turbojet. Flowpath overlaid on a CT scan of Engine D.

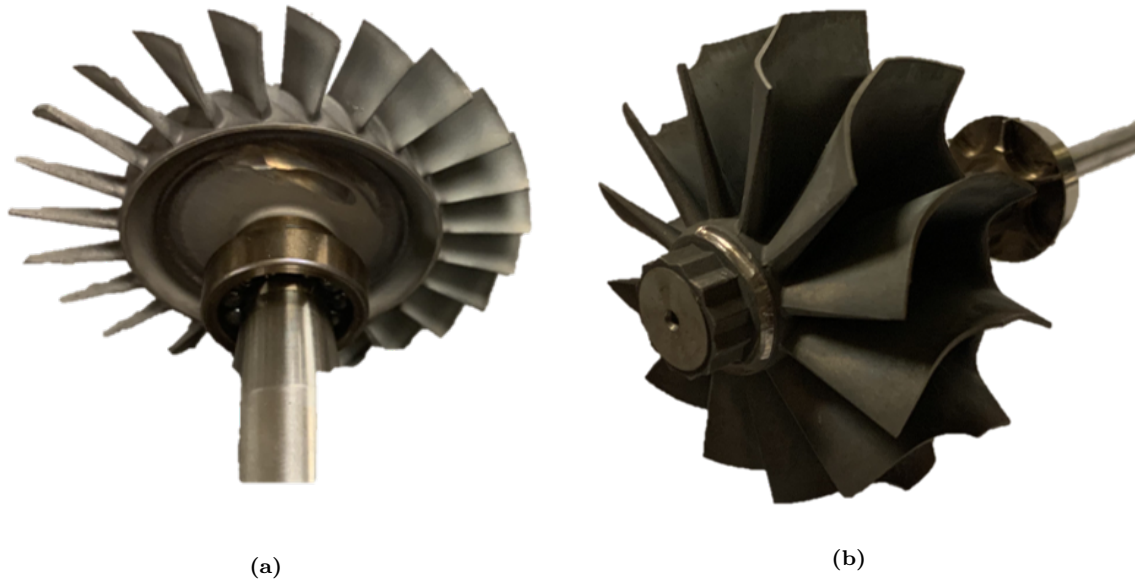


Figure 46. Microturbine turbojet turbines: (a) Axial turbine from Engine B, (b) Radial turbine from Engine D.

The compressor is a crucial component for determining engine performance. Blade count, diameter, blade angles, and many other parameters affect performance. Table 6 provides a summary of important compressor dimensions. Each compressor utilized splitters in their impeller design. Splitters effectively reduce the blade count at the inducer while keeping a high blade count at the impeller exit: allowing for increased efficiency and flow rates.

Microturbine engines require more than just the engine itself to operate. Batteries, pumps, valves, engine control units, receivers, plumbing, etc. are all accessories that are required for engine operation. Every engine manufacturer has its own way of

Table 6. Compressor impeller dimensions using compressor station numbering.

Engine	ID1	OD1	A1	OD2	Length	Z_r	β_{1b}
(-)	(mm)	(mm)	(cm ²)	(-)	(mm)	(-)	(°)
A	19.2	61.3	26	84.0	40.6	12	62.6
B	15.0	59.0	25	78.0	28.0	16	69.0
C	16.2	70.2	37	90.0	39.4	14	69.4
D	16.0	54.4	21	75.0	39.1	12	61.3

packaging these components. In the same vane, every manufacturer has its own way of defining what constitutes *engine weight*. For the sake of consistent comparisons, engine weight for this study was defined as the weight of the engine and all accessory components, barring external plumbing and batteries. Plumbing weight is insignificant compared to engine weight and battery size is variable depending on capacity. Table 7 provides the weight measured for each engine.

Table 7. Engine Weights (N).

Engine	Pub.	Meas.	$\Delta(\%)$
A	24.8	24.6	-0.81
B	14.3	17.7	+19.2
C	26.0	35.3	+35.8
D	30.4	32.6	+7.24

3.2 Facility: AFRL’s Small Engines Research Lab (SERL) Test Stand 5

Testing was conducted in AFRL/RQ’s Small Engine Research Facility at Test Stand 5. The facility layout is shown in Fig. 47. At the time of testing, this facility was capable of housing four separate engine experiments for small, gas-turbines or reciprocating engines. The facility is equipped with compressed air, compressed nitrogen, fuel-delivery and fuel-storage systems, thrust stand, and exhausting fans.

The engines used in this research were designed to have a nearby fuel tank (on the aircraft). Due to safety and logistic concerns, the fuel is stored in a separate, ventilated room. This storage solution requires a significant amount of plumbing to connect the storage tank to the engine: 50 ft of 1/8” plumbing. The small pumps that come with each engine cannot overcome the head loss of this system. To remedy this issue, compressed nitrogen is used to pressurize the fuel tank and provide continuous fuel flow to the engine. The amount of pressure required was dependent on the rate of fuel consumption.

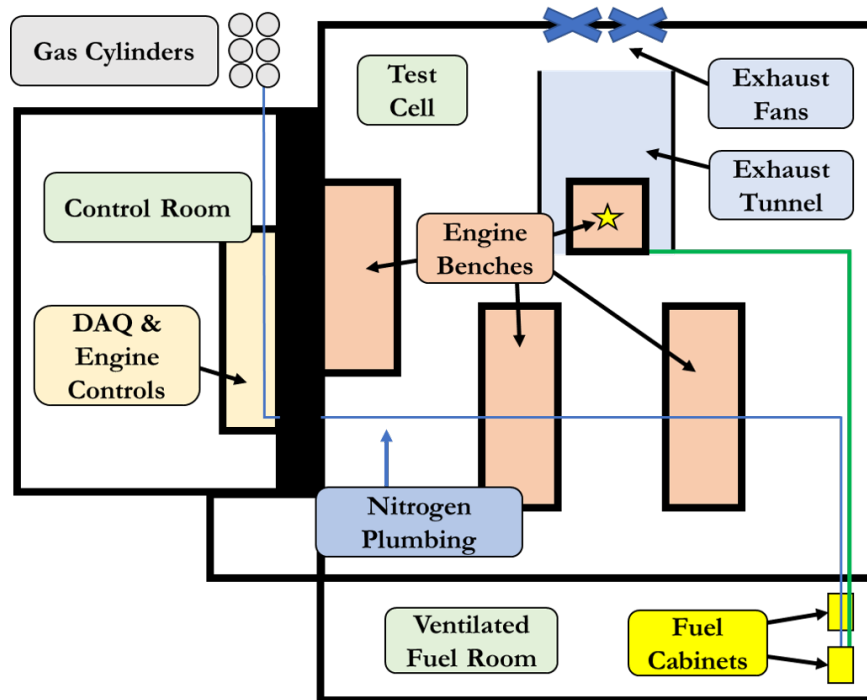


Figure 47. SERL's 5-Stand Floor Plan

Originally, the regulator for the fuel pressure was located within the test cell. Therefore, only a single fuel pressure could be set for the test. Engine B was particularly sensitive to the fuel-supply pressure. The lower fuel pressures with which the engine was able to start were too low for full-speed engine operation. The higher fuel pressures would flood the engine during ignition and cause the engine to overheat. In order to facilitate normal engine operation, a pneumatic regulator was added in the control room so that fuel-supply pressure could be adjusted during the test. A gauge pressure transducer was used to measure fuel pressure just upstream of the engine's pump. Fuel-supply pressure was adjusted to maintain a neutral or slightly-positive pressure gradient toward the engine.

Including the fuel pressure regulator, there were four devices in the control room that were used by the operator during experimentation. These devices are shown in Fig. 48. A LabView program, shown on the computer screen, was used to collect and monitor data. This code was written by Nick Grannan at ISSI and had a data

acquisition rate of 10 Hz. On the desk, from left to right, the first three devices are the ground control units/data terminals for Engines B, C, and D, respectively. These units are from the manufacturer. They serve a variety of control functions and live-stream data that the engine is recording. These are useful for testing components such as starter motor, glow plug, fuel pumps, and fuel valves. After reconstructing engines or after extended periods of without being operated, it is necessary to check each of these functions before attempting to start an engine. To the right of the three ground control units is the servo controller. In a flight setup, these engines are controlled by a radio transmitter and receiver. The receiver generates a pulse width modulation signal that controls engine speed. In the experimental setup, the servo-controller is used in place of the transmitter-receiver setup and generates a PWM signal that mimics the receiver output for engine control. On the far right of Fig. 48 is the regulator for the fuel pressure.

3.3 Thrust Stands

The purpose of any aircraft propulsion system is to generate thrust. Therefore, it is imperative that thrust is measured accurately and reliably. When the research for this thesis began, a single-component, air-bearing thrust stand was in use at SERL's Five Stand. This thrust stand had a fairly high uncertainty in its thrust measurements (3-5%). Testing began with this stand because it was the existing standard for SERL. During testing it was realized that this thrust stand was not capable of measuring the largest engines. It was determined the thrust stand needed to be upgraded to support the larger thrusts of Engine C. The replacement stand, a flexure-based system, improved both the maximum capacity and the measurement accuracy of thrust measurements for the facility. Time constraints prohibited Engines A, B, and D from being retested on this stand. This section begins by providing

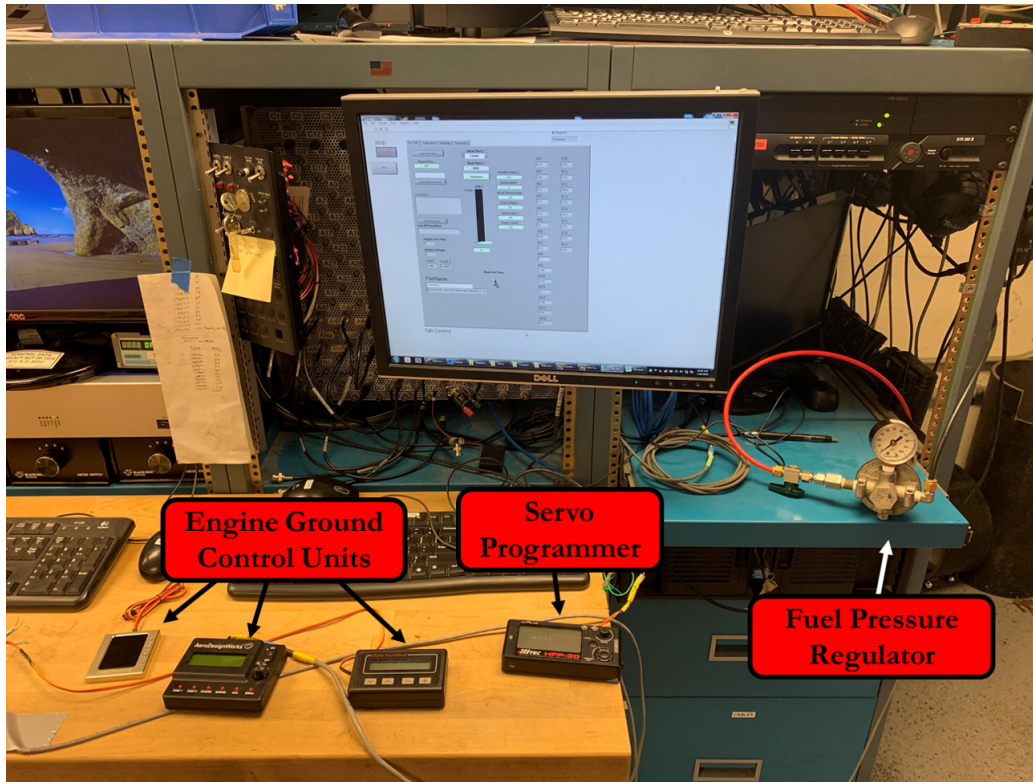


Figure 48. Photograph of the control room identifying equipment needed during testing.

physical descriptions of each thrust stand, to include the reason for failure of the air-bearing stand. After both descriptions are provided, the calibration processes and results for each thrust stand are provided.

Both thrust stands were single-component, off-axis stands. ‘Component’ refers to the number of component forces that are measured. The single component stand used in this experiment measures the axial force produced by the engine exclusively. ‘Off-axis’ refers to the alignment of the load cell with centerline of the engine [37]. Essentially, this description of the thrust stand indicates whether the axis of the instrument is coincident or offset from the axis of thrust.

The pre-existing thrust stand, shown in Fig. 49, utilized air bearings to separate the floating frame from the base structure. The air bearing system, shown in Fig. 50, was designed to reduce stresses endured by the test stand’s structure so that the

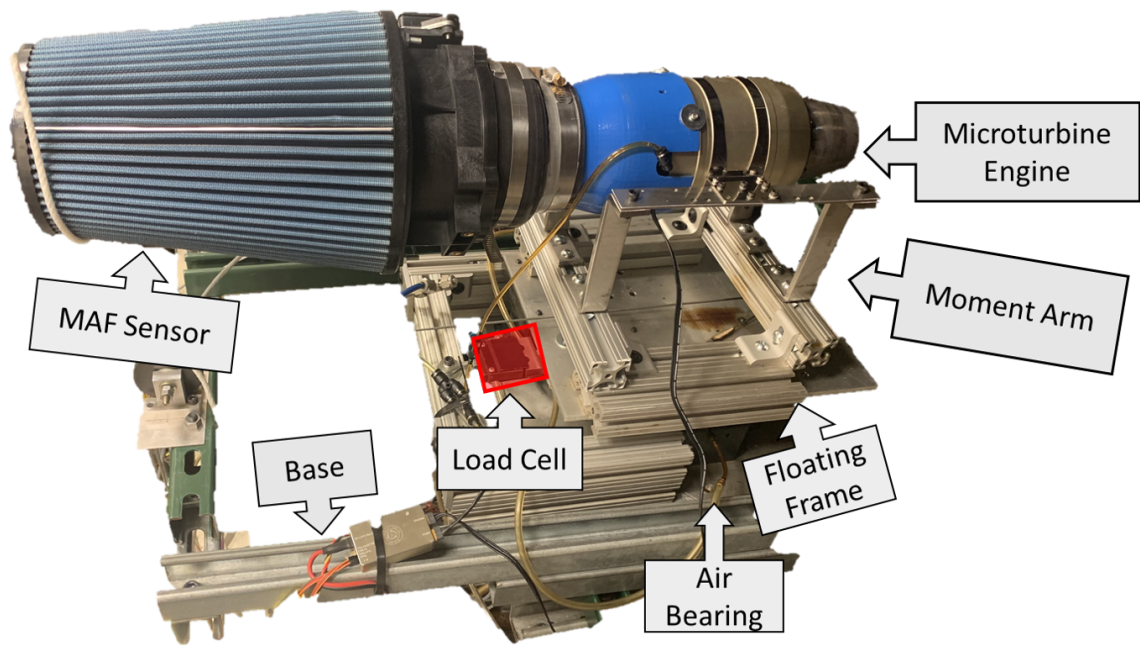


Figure 49. Pre-existing, air-bearing thrust stand.



Figure 50. Air-bearings used to support pre-existing thrust stand.

engine's thrust is resisted solely by the load cell. This configuration was supposed to be satisfactory for this class of engines and no modifications were intended. Unfortunately, while testing Engine C (the highest published thrust), thrust measurements were close to 25% lower than the published value. It was determined that this discrepancy between measured and published thrust was due to a failure of the air-bearing system. The large moment imposed on the thrust stand by the engine was causing the air bearing to rotate and seize. This bearing failure changes the tare of the stand and creates inaccurate measurements. A new, more-accurate calibration process was devised (see Section 3.3.1), and it was determined that the bearing failure occurred near 260N. This left the results for Engines A, B, and D unaffected, but the thrust data for Engine C was no longer acceptable.

In order to resolve this issue, a new thrust stand was installed in 5-Stand, shown in Fig. 51. Nick Grannan of ISSI had recently designed and installed a thrust stand



Figure 51. Installation of new, flexure-based thrust stand.

for testing microturbines with up to 900 N thrust at a neighboring facility. This stand was deemed suitable for the purposes of this research and of SERL in general, so it was replicated and installed in place of the existing air-bearing thrust stand. The manufacture of the stand components was contracted out to a local machinist with water jet capabilities.

Here the design of the new thrust stand will be briefly discussed. Fig. 52 shows a side view of the thrust stand. In this view, the flexures used to connect the floating

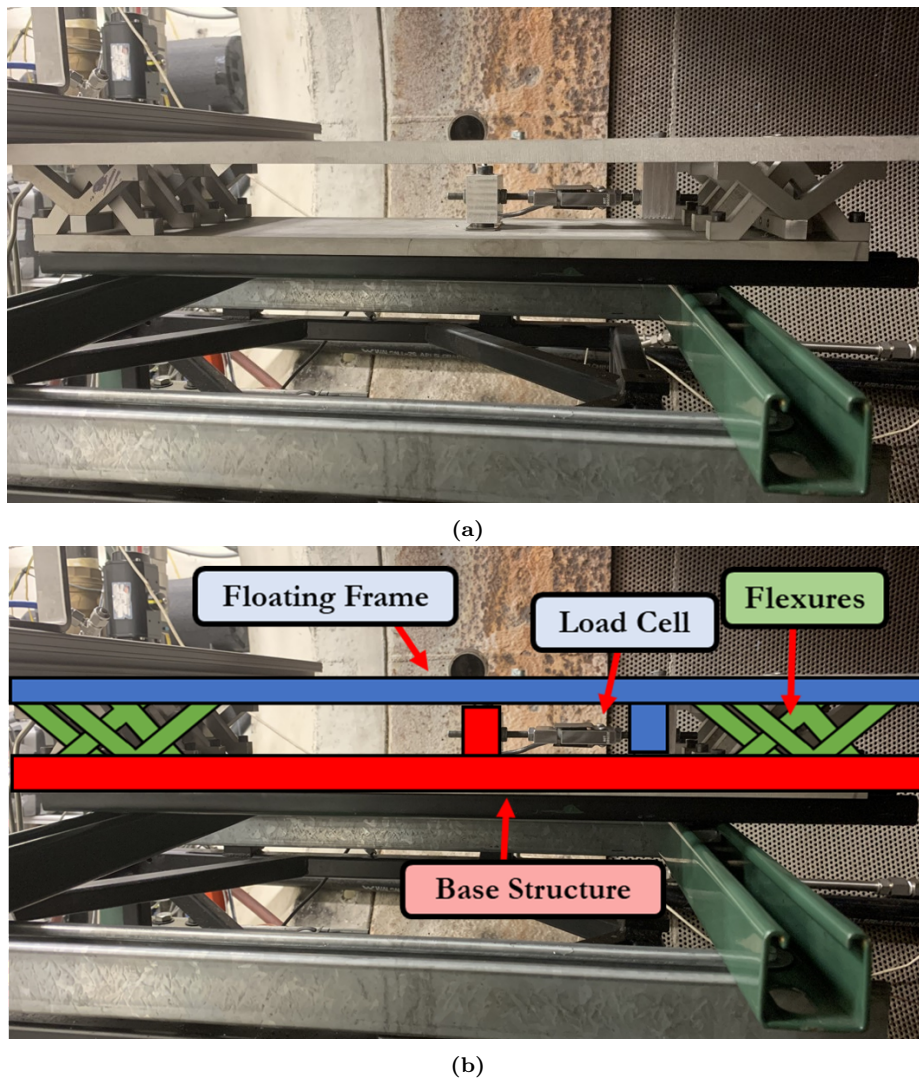


Figure 52. Flexure Thrust Stand Side View: (a) Photograph, (b) Same view with annotations

frame (top) to the thrust stand base (bottom) are clearly visible at the left (front) and right (rear) of the thrust stand.

While air-bearings are an acceptable thrust stand component, there are several benefits to employing flexures instead of air bearings. Flexures create a repeatable, interaction tare unlike air bearing designs. So long as the flexures, seen in Fig. 52, are not exposed to stresses beyond their yield stress, they will continue to deform elastically, and their deformations will be repeatable and predictable. This results in a much more accountable tare than the air bearings. The tares associated with the air bearings are due to friction and can be attributed to either the accumulation of dirt within the bearings or the application of large moments. Tare associated with these non-repeatable forces increases measurement uncertainty. The flexure-stand is not susceptible to these uncertainties, giving it improved capacity and accuracy.

The load cell is located in between the two series of flexures. A closer view of the load cell is presented in Fig. 53. The base-side bracket was shimmed to ensure that load was transmitted axially to the load cell and that no bending moment was forced onto the load cell. Locknuts on both sides of each bracket and of the load cell ensure the assembly is rigid and prevent hysteresis due to rotation of the rod.

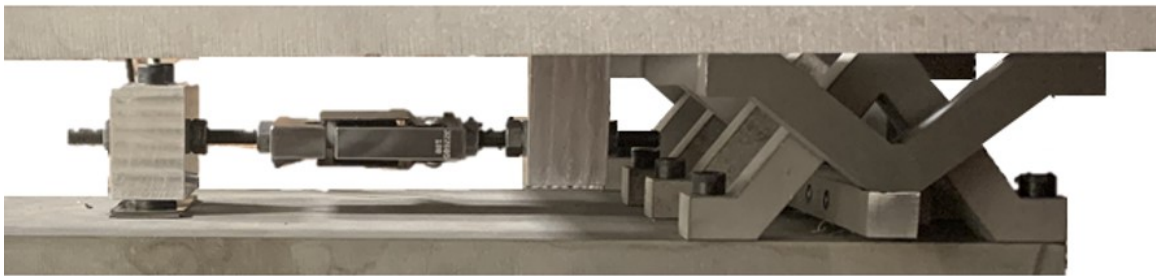


Figure 53. Close-up of the load cell connection between the floating frame and base.

3.3.1 Thrust Stand Calibration.

Calibration accounts for tare by creating a function that relates the measurement reading from the load cell to the applied load. Because load cells output a linear relationship between output signal and load, the goal is to find the slope of the line that relates the output on the load cell to engine thrust. This slope would be one if there were no tare and the load cell was directly measuring the applied load. Tare exists due to misalignment of the axis, the offset, deflections in the thrust stand structure, etc. See Section 2.8.1 for more information on tare. The y-axis intercept of the linear relationship is not a significant result of the calibration process. This is the zero-thrust condition for the thrust stand and will fluctuate with environmental conditions. For example, stresses induced by thermal expansion due to changes in ambient temperature will cause the zero-thrust reading of the load cell to change.

Two separate calibration processes were used. The air-bearing thrust stand calibration process and results are provided first, followed by a similar discussion for the flexure-based thrust stand. Because the load cells used were calibrated in lbs, the calibration process will be described using US Customary units. There are several points of consideration for a proper calibration process. First, the calibration must meet or exceed the maximum expected thrust of the engine. If the thrust is larger than the applied load used to calibrate the stand, unknown tares may develop which will not be properly accounted for in the calibration function. For these experiments, calibrations needed to exceed 75 lb (maximum thrust of the largest engine). Second, the calibration load should be applied in small enough increments that the linearity of the relationship between thrust and load cell reading can be verified. A nonlinear relationship may indicate that the floating frame is making a new contact with a grounded object [37] or the development of some other non-repeatable interaction tare. Dividing the maximum load by five proved to provide sufficient resolution for

proving linearity and determining thrust-stand hysteresis. Third, the calibration load should be applied in both an increasing and a decreasing manner. These will be referred to as the loading and the unloading calibrations, respectively. This will allow for any hysteresis in the stand to be incorporated into the uncertainty of the calibration function. Calibration using only measurements from increasing loads would only be appropriate if it could be ensured that the engine never decreased the thrust it produces. This is very difficult to ensure for these engines because of their control schemes. Thrust overshoot is common and not quantified. Therefore, the effects of hysteresis must be taken into consideration. Fourth, the calibration load must be applied along the thrust axis. This point is especially significant for the air-bearing thrust stand because it is sensitive to large moments. Applying the calibration load along a different axis creates a different moment than the moment produced by the thrust force. This can lead to issues in accounting for deflection tare, specifically impingement of the air bearing rod on its holster. A calibration that takes each of these four points into consideration will produce a calibration function that accounts for all repeatable tare. Any tare that is not repeatable will be represented as uncertainty in the thrust measurement.

3.3.1.1 Calibration: Air-Bearing Thrust Stand.

Calibration for the air-bearing stand used several calibration weights and a hanger. It was found that the existing method for calibrating the thrust stand was susceptible to error. Fig. 54 illustrates the fault of the pre-existing method that was in use at SERL when this research started and the enacted solution. Originally, a cord supporting the calibration weight ran from the weight holder to a pulley and was anchored to a bolt on the floating frame of the thrust stand, as seen in Fig. 54a. It can be seen that there is a significant moment arm between the air bearing and

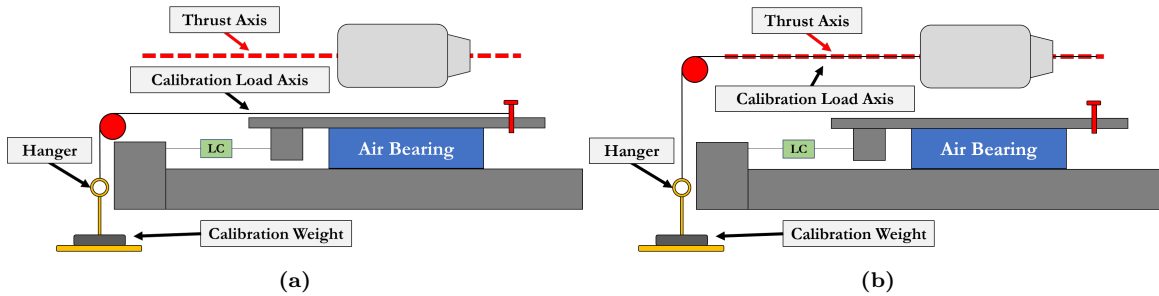


Figure 54. Correction of air-bearing thrust stand calibration issues: (a) pre-existing calibration setup, (b) corrected calibration setup.

the axis of thrust, approximately 2.5 ft. At low thrust, the air bearings were able to withstand the moment produced by the engine and functioned normally. However, at higher thrusts, the moment created by the engine was too large and the air bearings seized, causing a significant increase in friction, a non-repeatable tare. This set the upper limit for the thrust stand at approximately 260N.

The solution to this calibration issue is shown in Fig. 54b. By moving the calibration load to be coincident with the thrust axis, the moment produced by the calibration load became representative of the moment produced by the engine's thrust. This allowed the tare to be calibrated more precisely. Note, this does not necessarily increase or decrease the accuracy of the thrust stand. Rather, the uncertainty indicated in the calibration process is more realistic because both repeatable and non-repeatable tares are more properly being accounted for during the calibration process. Photographs of the air-bearing thrust stand during a proper calibration are shown in Fig. 55. Fig. 55a presents the calibration weights and weight hanger at the bottom of the image. Fig. 55b shows that the calibration load is properly aligned with the thrust axis by attaching the calibration cord to the rear engine mount. An additional structure was added to the thrust stand to align the pulley with the thrust axis while allowing the calibration weight to hang freely.

The results from this thrust stand calibration are presented in Fig. 56. This calibration curve is presented with the load cell measurement on the x-axis and the

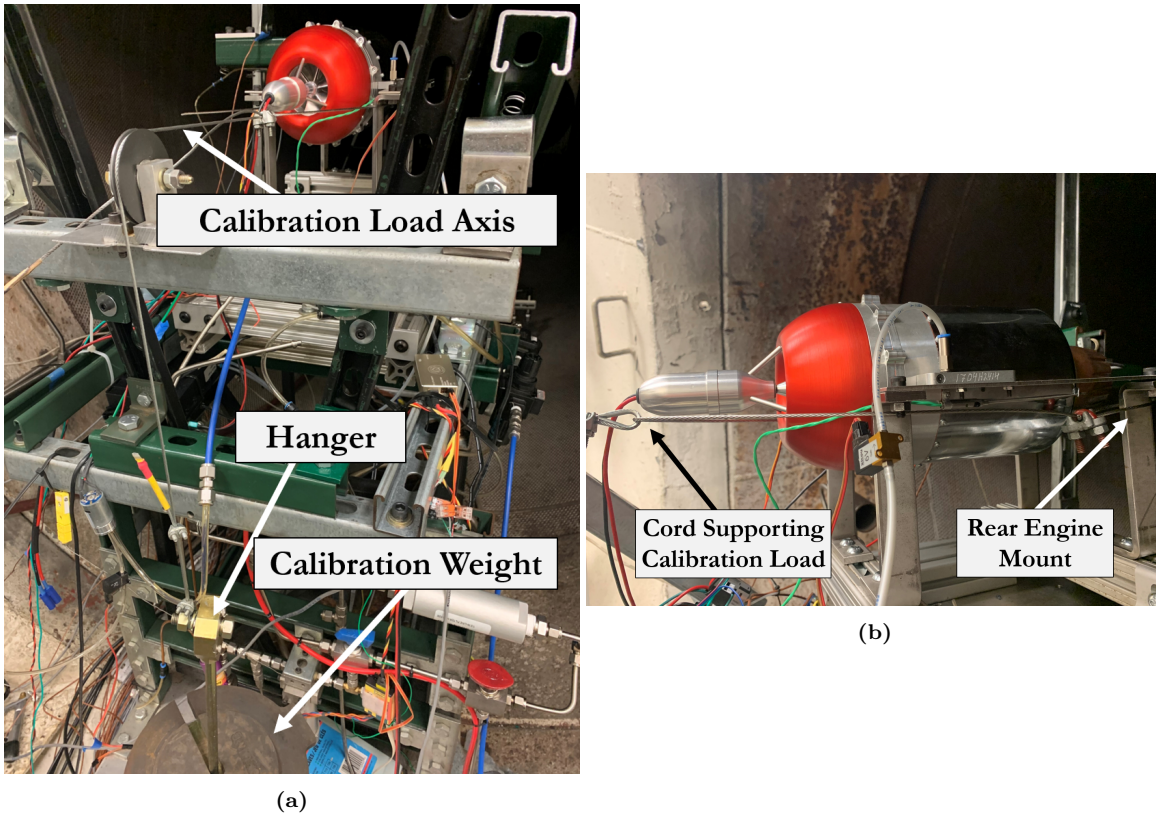


Figure 55. Proper calibration process for the air-bearing thrust stand. (These diagrams will be appropriately colored later)

calibration weight on the y-axis. Since the same calibration weights were used each time, the calibration creates a series of vertical groupings of data points. The variation along the x-axis is due to non-repeatable tares in the thrust stand. Using the trendline shown in Fig. 56, the calibration can be described as: $\text{Applied Load} = -1.0123(\text{Load Cell Reading}) + 13.215$.

Since the load cell is in compression, increases in calibration load are realized as decrease in load cell reading. Note, with zero calibration weight, the load cell reads +13.2. The load cell was removed from the thrust stand to confirm that the stand was not putting the load cell into tension while at the zero load condition.

Once the calibration curve is created, it is necessary to determine how well the curve accounts for tare. Using the same data that was used to produce the calibration

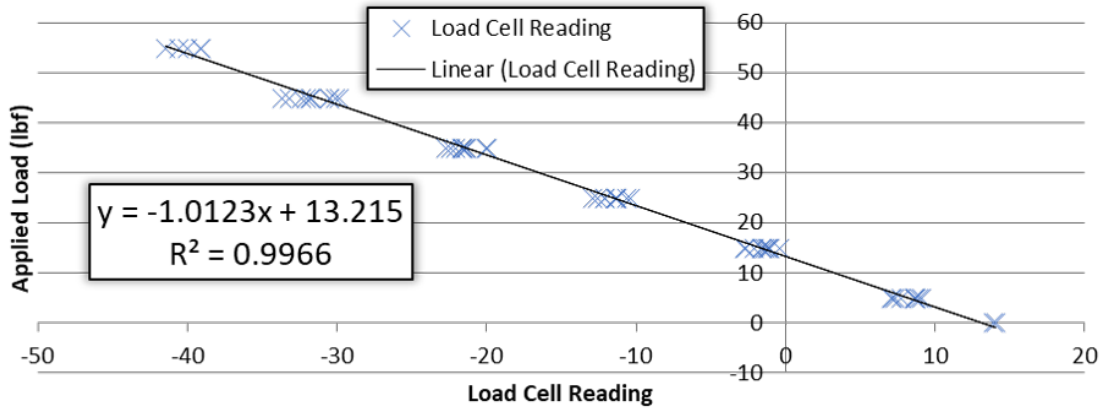


Figure 56. Calibration results for the air-bearing thrust stand.

curve, the load cell readings were used to calculate the applied calibration load. This calculation was based on the calibration curve. The error between the calculated applied load and the true calibration load are shown in Fig. 57. Fig. 57a, presents the tare detected at each load in terms of force while 57b presents the error as a percentage of the calibration load. According to Fig. 57a, it there is a minimum uncertainty of approximately 1.25 lbf. According to Fig. 57b, it seems that there is a minimum uncertainty of approximately 5%. It can be inferred that the uncertainty of the air-bearing thrust stand is the greater of 1.25 lbf or 5% of the applied load.

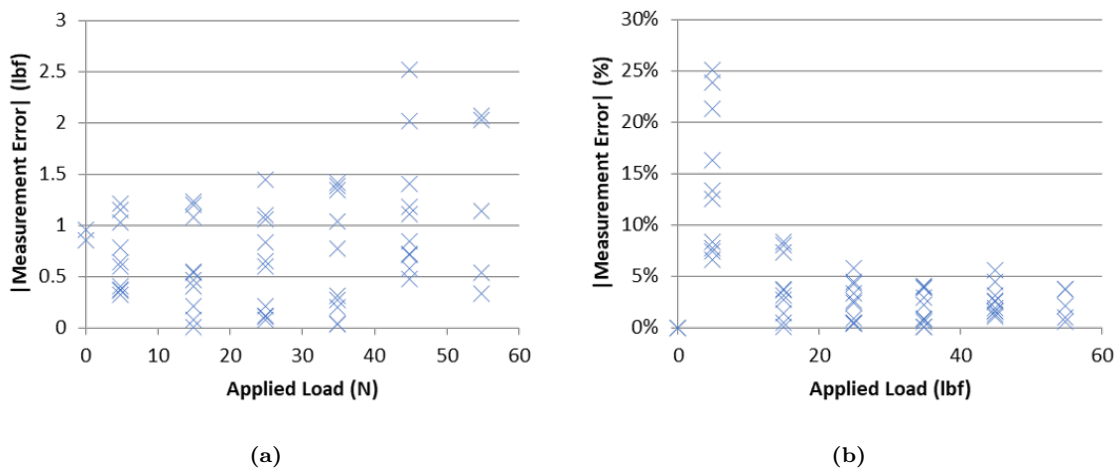


Figure 57. Uncertainty development. Error given in (a) lbs and (b) % of applied load.

3.3.1.2 Calibration: Flexure Thrust Stand.

The calibration process for the flexure-based thrust stand was different from that of the air-bearing stand. Rather than use a hanger and weights, calibration of the flexure-based thrust stand utilized a linear actuator and a second load cell, as seen in Fig. 58. The linear actuator was mounted to the base of the thrust stand. One side of the load cell was connected to the linear actuator while the other was connected to the floating frame. Unlike the calibration of the air-bearing stand, this system does not use any wire cables. Use of the cables created alignment issues and degraded the calibration process by introducing non-repeatable tare forces due to sliding cables.

By retracting the linear actuator, the floating frame is pulled forward. This load simulates the thrust of the engine and puts the thrust stand load cell into compression

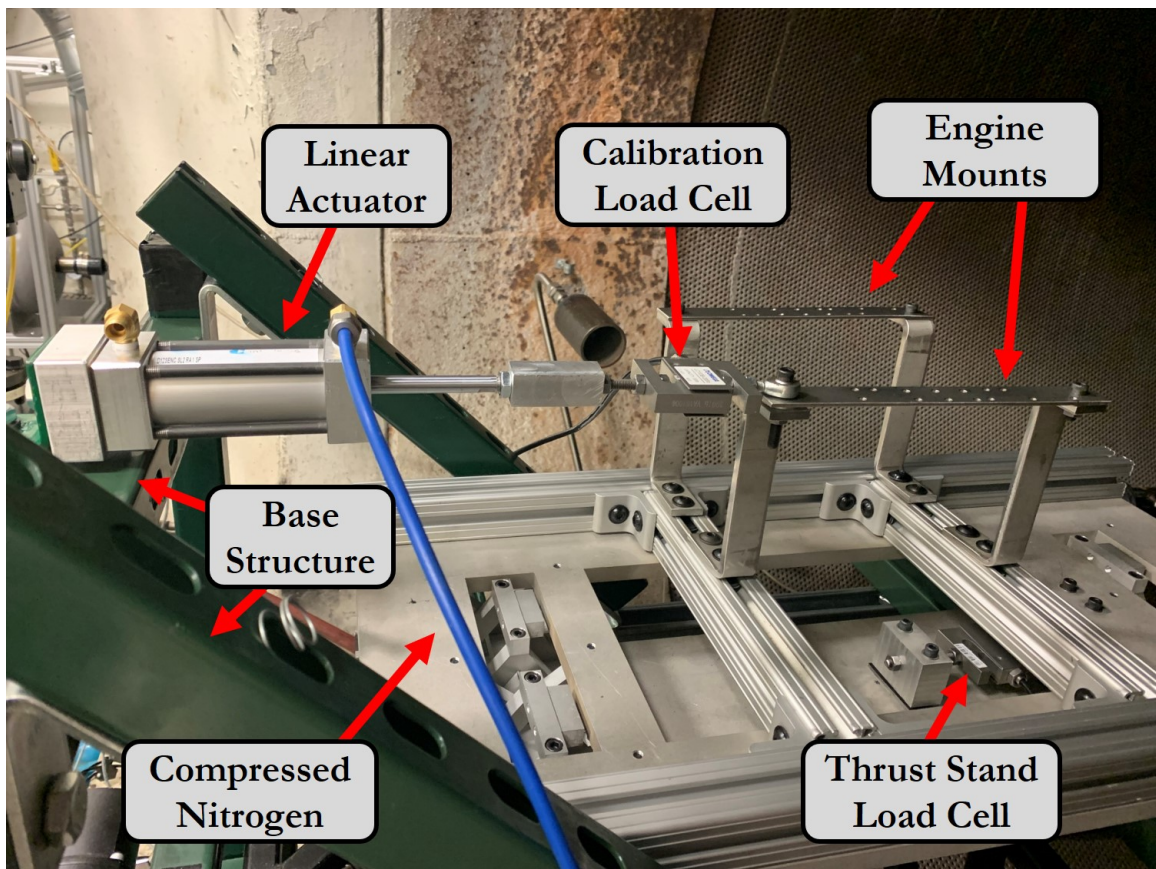


Figure 58. Calibration setup for flexure-based thrust stand: side-view.

while putting the calibration load cell into tension. Using the measurements from the calibration load cell as the applied load, the thrust stand load cell can be tared. The tare is equal to the difference between the applied load (indicated by the calibration load cell) and the load measured by the thrust stand load cell.

It is necessary for the calibration load to be applied coincident with the thrust axis. Any misalignment will result in an incorrect calculation of the tare of the thrust stand. In order to ensure that the the calibration load was correctly aligned, a careful alignment process was followed while mounting the calibration system and while mounting the engine. The axis of thrust was designated to be horizontally offset from the inner edge of the reinforcing side-bar by 5.5 inches and vertically coplanar with the top of the engine mounting brackets. The establishment of the horizontal offset is shown in Fig. 59a. In this image, the thrust axis is projected onto the thrust stand and shown as a solid black line. The dashed black line is offset from the thrust axis by a distance equal to the radius of the actuator shaft, 4.75 mm. A plumb bob, shown in Fig. 59b is dropped from the actuator shaft to ensure that the shaft is axially aligned with the thrust axis. The plumb bob is checked at the base and the tip of the actuator shaft. When the plumb bob hangs over the offset dashed line in both locations, the shaft is axially aligned. At this point, the actuator was firmly secured, leaving the load cell cantilevered off the tip of the actuator shaft, as shown in Fig. 60a.

In addition to proper axial alignment, it is crucial to ensure that no undue forces or moments are being applied to the load cell when it is fixed to the engine mount. Best practice in minimizing these unwanted forces is to align the turnbuckle hole on the load cell with the hole on the engine mount and then securely fasten the mount and the load cell into place. Proper alignment of this connection is shown in Fig. 60. Once both structures are rigid, a bolt can be used as a pin to connect the load cell to

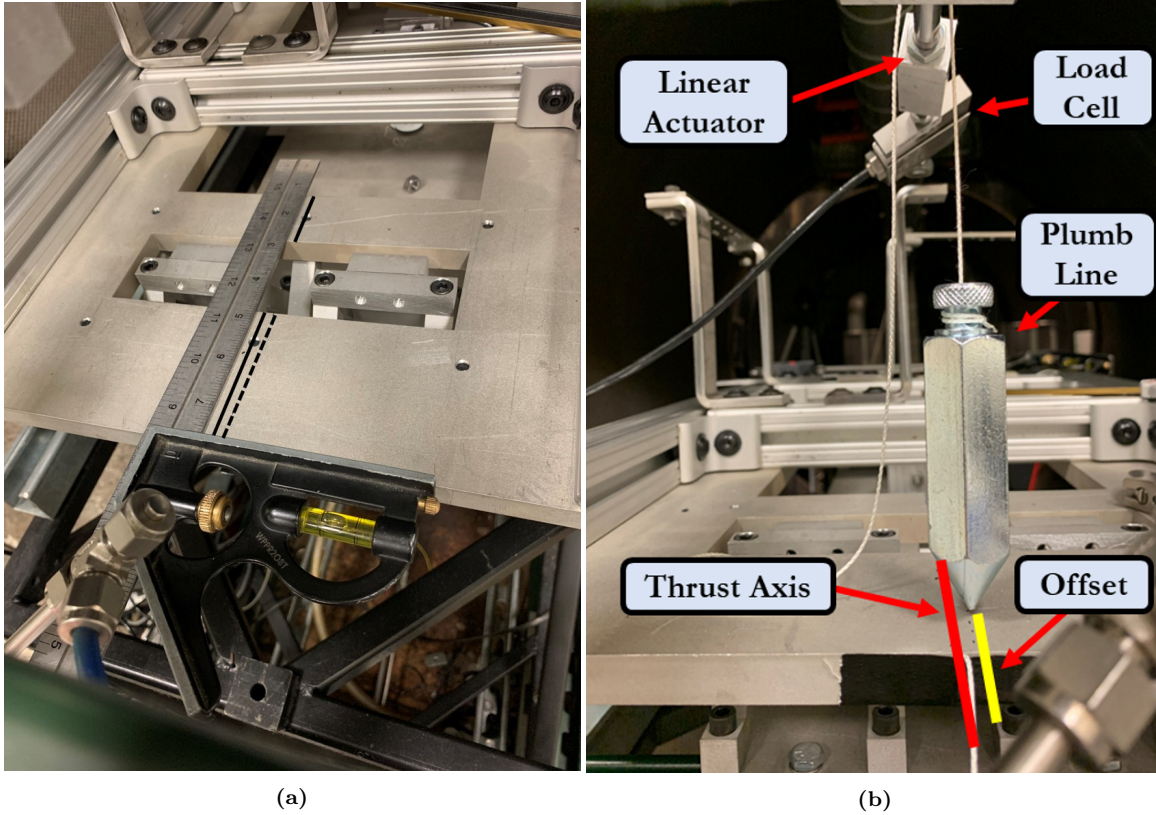


Figure 59. Alignment of linear actuator with thrust axis: (a) establishment of thrust axis and offset, (b) use of plumb to align linear actuator with thrust axis.



Figure 60. Flexure-based thrust stand calibration load cell connection alignment: (a) side-view of attachment, (b) vertical alignment of load cell connection with engine mount.

the engine mount. If the two components are properly aligned, the pin will be able to be raised and lowered freely. Once this alignment is achieved, the pin was fastened using washers to shim the load cell connection as shown in Fig. 61.

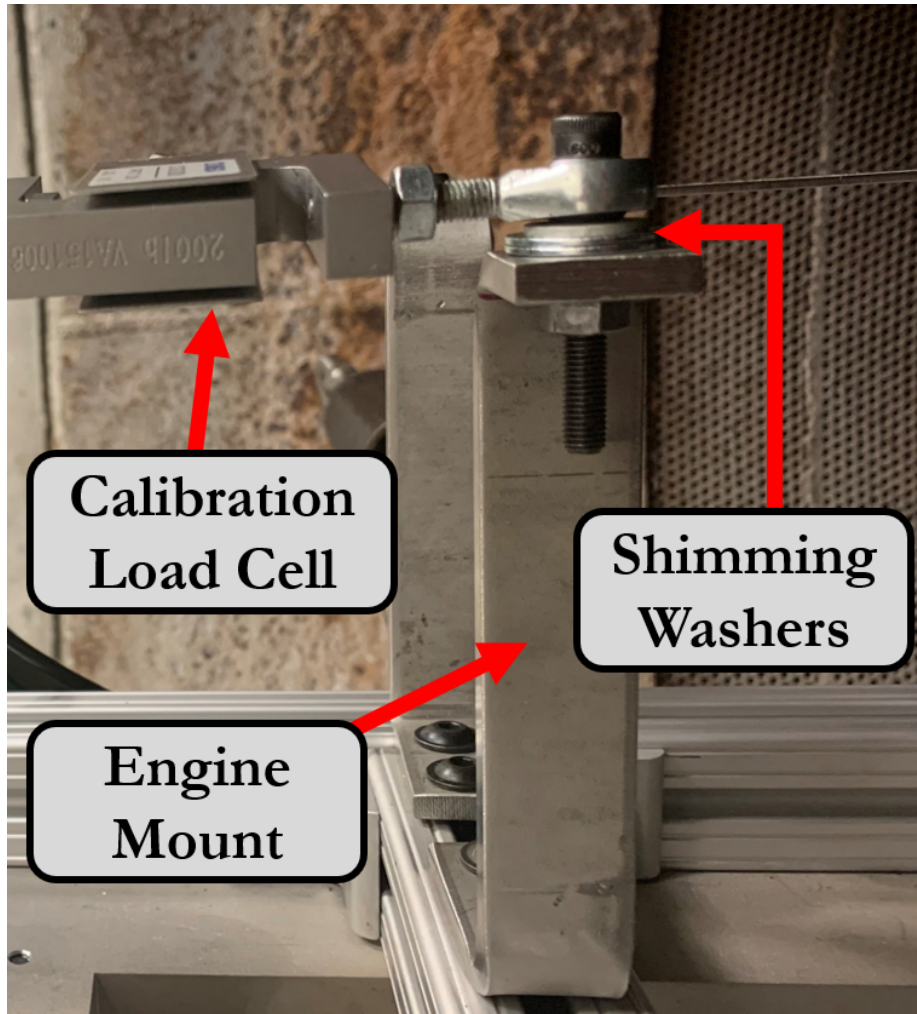


Figure 61. Vertical alignment of load cell using washer to shim connection between load cell and engine mount.

Results of the calibration process are shown in Fig. 62. Fig. 62a shows the raw data from the calibration load cell. Fig. 62b shows the raw data from the thrust-stand load cell. Once the calibration actuator reached the desired load, data was gathered while the stand and actuator were at rest. These periods are indicated by the horizontal steps of the data in Fig. 62. Ten seconds of data along each of these

steps was used to determine an average load cell reading. The same was done for the load cell indicating the calibration force. Ten seconds of data at 10 Hz results in data sets of 100 samples. These 100-sample data sets are indicated by the colored markers in both data sets. Red indicates samples used to create the *loading* calibration curve. Blue indicates samples used to create the *unloading* calibration curve. Points were selected on the calibration load cell data set. The time-stamps on those data points were used to identify the samples in Fig. 62b. The thrust stand load cell is in compression while the calibration load cell is put into tension by the actuator. This explains the sign difference between the load cell readings.

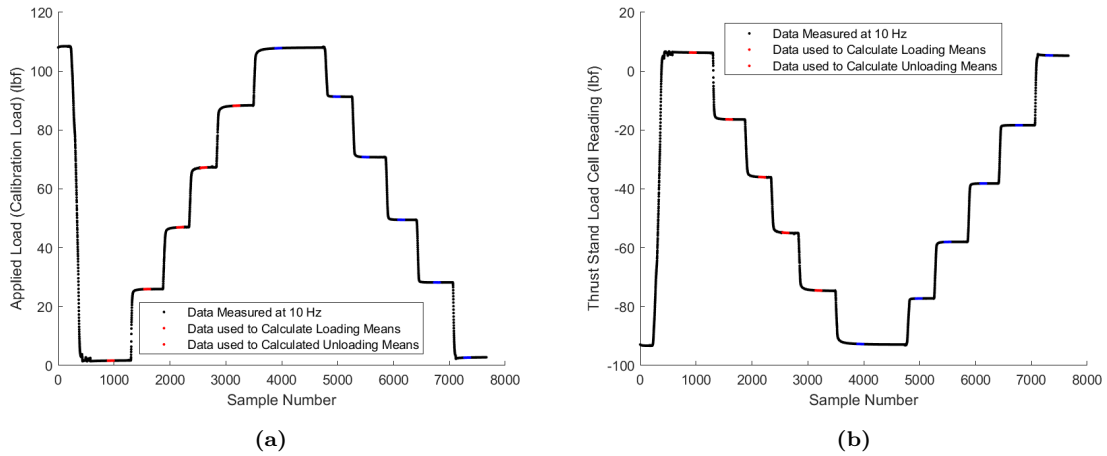


Figure 62. Raw Data used to Calibrate Flexure Thrust Stand.

Fig. 63a compares the thrust stand load cell reading (x-axis) to the calibration load cell reading (y-axis). It can be seen that the relationship between these two data sets is linear with a slope near unity which is to be expected since identical

Table 8. Flexure Thrust Stand Calibrations.

Cal.	p_1	p_2
1	-1.072	8.391
2	-1.072	8.394
3	-1.072	8.396

load cells are being used for each measurement. Fig. 63b shows the change in tare as the load changes. Note that this relationship is linear. This indicates that the tare is mostly attributed to repeatable sources (i.e. reaction forces from the deforming flex-

ures). Using this data, the following calibration curve can be calculated as a linear curve fit:

$$AppliedLoad = p_1(StandLoadCellReading) + p_2 \quad (61)$$

Three calibration tests were completed. The coefficients of the linear calibration curve-fits associated with each test are shown in Table 8. From the results of this test, the scaling factor used to determine the applied load from the output of the stand load cell was -1.072. The scaling factor of the loading and unloading curve fits matched to 4 significant figures.

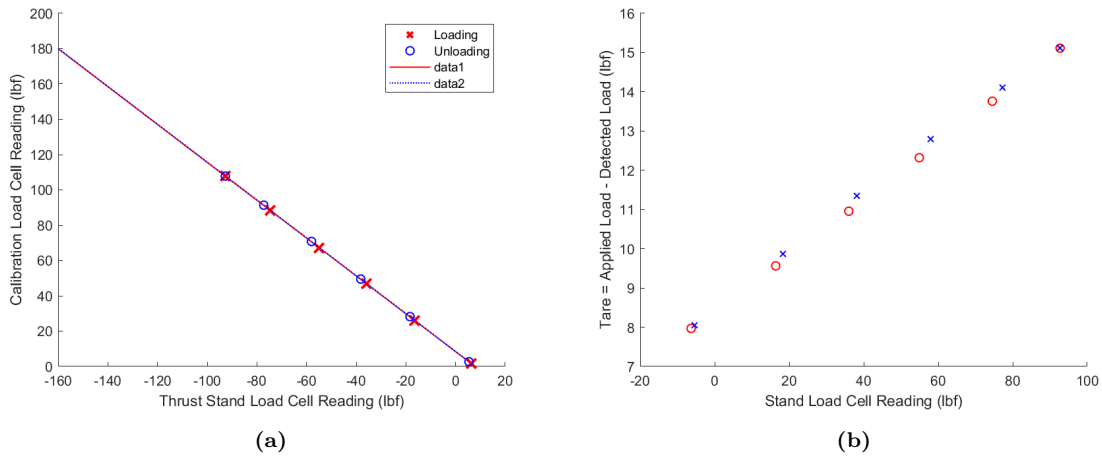


Figure 63. Raw Data used to Calibrate Flexure Thrust Stand.

There are many factors that contribute to measurement uncertainty. The uncertainty of the load cell is 0.03 %. The highest thrust measured during the calibration process was 180 lbf. If the load cell uncertainty was the total uncertainty of the thrust measurement, the maximum uncertainty would be 0.054 lbf. However, hysteresis in the stand and other non-repeatable tare forces are larger than the load cell uncertainty. Fig. 64 shows the error between the load determined using the calibration equation and the applied load measured by the calibration load cell. From these results, the uncertainty of the thrust stand due to hysteresis is 0.25 lbf. This was the largest thrust-stand uncertainty to be measured.

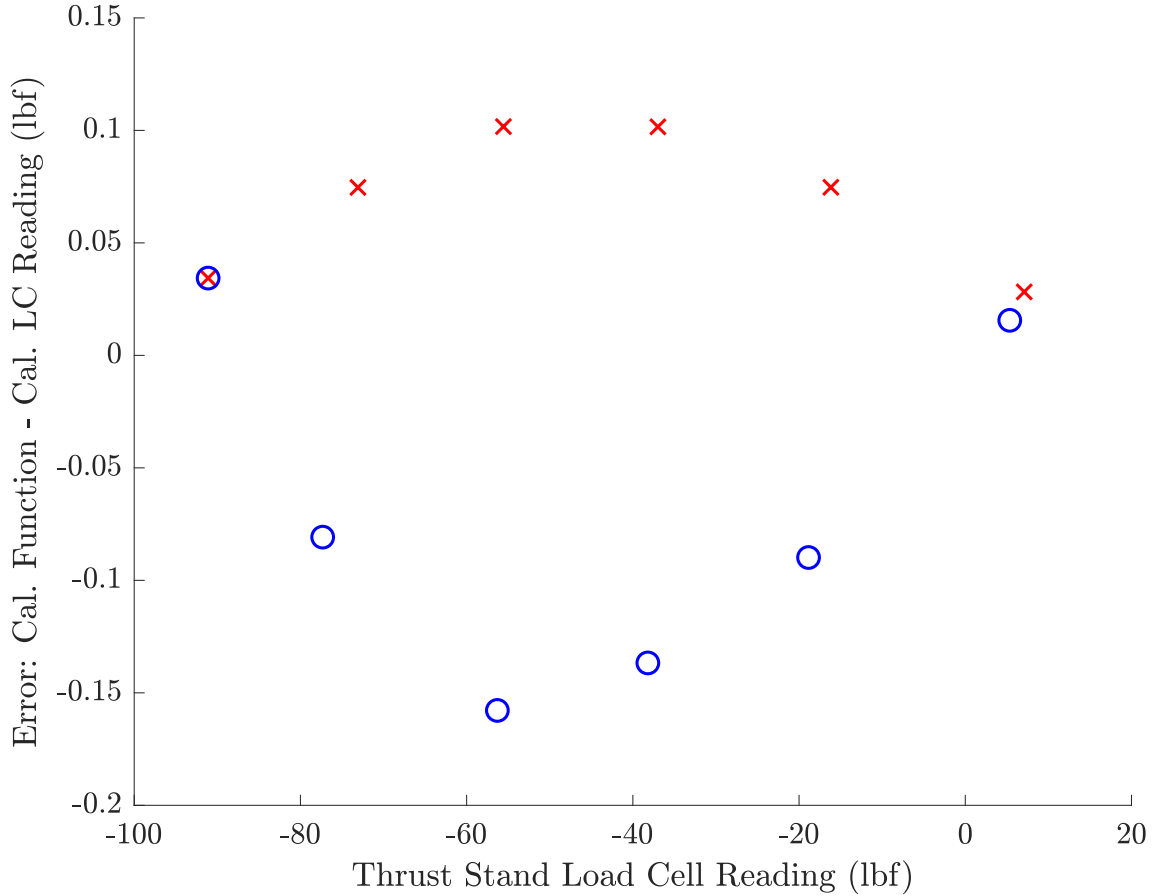


Figure 64. Quantification of uncertainty due to hysteresis.

3.4 Instrumentation

Determining the potential performance of recreation-grade turbojets requires an understanding how current engines are achieving their performance. Once component-level performance is understood, the highest performance components can be theoretically combined to predict the potential performance based on recreation-grade components. Experimental analysis is an important aspect of engine development and evaluation. Systems and components do not always behave as expected due to physics that are not accounted for in models or due to unexpected interactions between components. While theory, models, and correlations are necessary for effective engine design and analysis, they are only theoretical predictions until validated by

experimental data. The large variation of temperatures and pressures at different engine stations makes accurate instrumentation necessary for conclusive engine analysis. Internal instruments must be kept away from rotating turbomachinery and must be survivable in the harsh combustor conditions. These and other experiment-design considerations will be discussed in the following sections. Section 3.4.1 discusses the data acquisition system used to record measurements. Section 3.4.2 discusses the mass air flow meter and its calibration. Section 3.4.3 discusses internal instruments used to determine station properties.

3.4.1 Data Acquisition System.

Data acquisition systems (DAQs) are used to manage instruments and to convert their output to a useful signal that can be recorded or streamed. SERL uses National Instruments equipment and software for data acquisition. The software associated with National Instruments' DAQ is the LabView program. This software allows the user to create an interface that allows them to monitor the experiment real-time and record data. The hardware for the DAQ is dependent on the signal produced by the instrument. National Instruments has interchangeable "cards" for different instrument types which provide ports to wire the instrument into the DAQ. Three cards were used in this DAQ setup: (1) an analog input card, (2) a thermocouple card, and (3) a strain-gauge card. These cards can be seen in Fig. 65. Each card accepts multiple inputs of that type.

While many instruments output signals as a voltage that is calibrated to physical units, some instruments output signals as a frequency. In this experiment a Hall Effect RPM sensor was used to measure engine speed and a flow meter were used measure volumetric flow rate of the fuel. Both of these instruments output their

signals as a frequency. Red Lion frequency converters, seen in Fig. 65, were used to filter noise and convert the frequency output to a calibrated voltage.

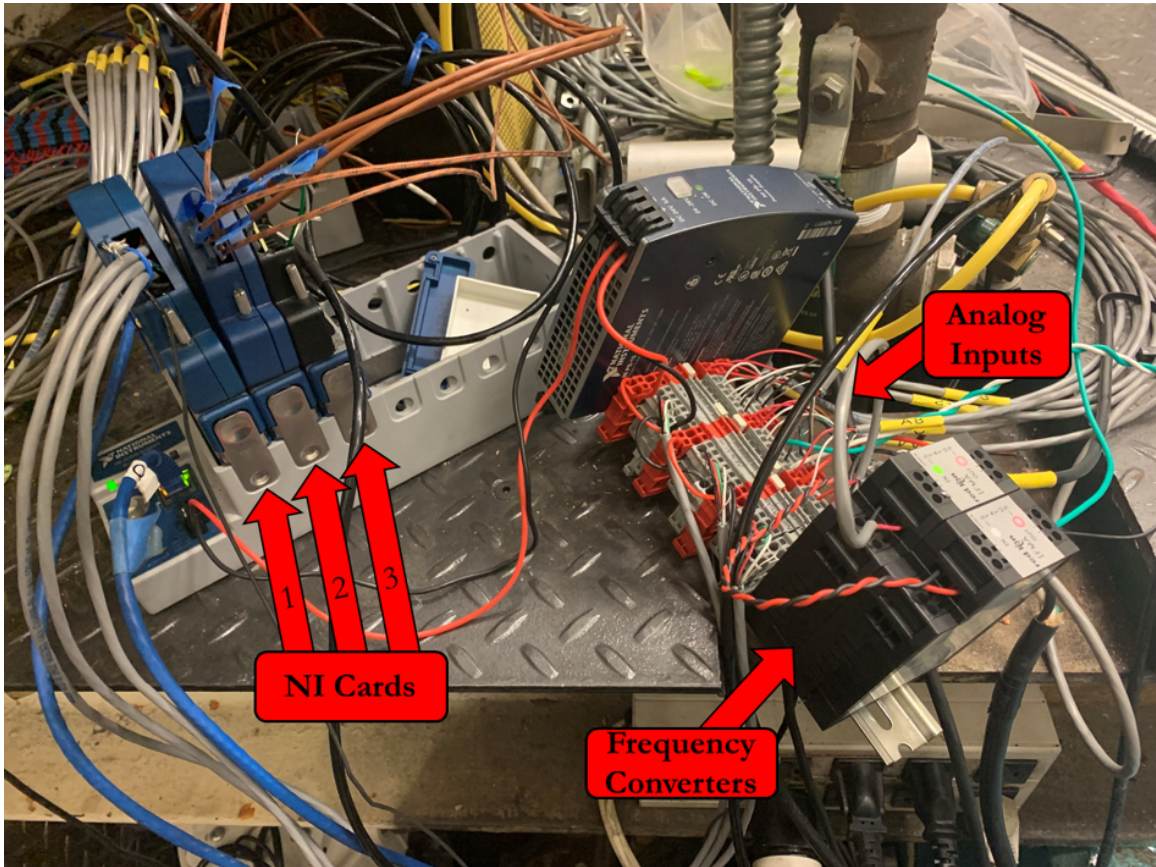


Figure 65. DAQ.

3.4.2 Mass Air Flow Sensor.

Mass air flow rate is an important engine parameter for a number of performance evaluations: comparing engine sizing, normalizing thrust, determining flow velocity and predicting combustor temperature. An automotive mass air flow rate sensor (MAF) was used for this measurement. Adapters were needed to connect the MAF to the engine. These were designed by Simon Ray of ISSI and were additively manufactured within AFRL. Fig. 66 shows the MAF connected to Engine B. Flexible hosing and two hose clamps were used to connect the MAF to the adapter. Each

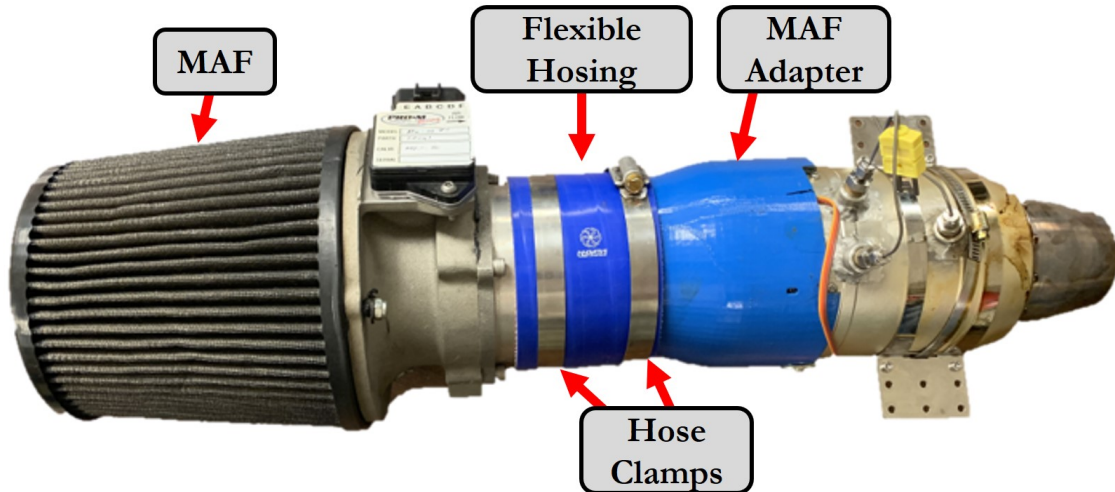


Figure 66. MAF connected to Engine B using additively manufactured adapter.

engine needed a unique adapter to accommodate its inlet and the bolt pattern used to attach the secure the casing. This allowed the existing bolt tappings to be used to secure the MAF. These adapters provided structural support for the MAF and created a smooth transition for flow entering the engine. This minimized pressure drop associated with the additional hardware and minimized flow distortions that would affect compressor performance. These adapters were strong enough to support the weight of the MAF cantilevered off the front of the engine. However, extended exposure to the hot engine caused the adapter to deform after several uses.

To ensure that all air that was ingested by the engine first passed through the MAF, the adapters were designed to fit tightly around the engine inlet. Since the MAF adapters were additively manufactured, they were fairly porous and air could pass through the wall. To alleviate this concern, MAF adapters were coated with spray paint. This coating sealed the walls of the adapter to prevent airflow through the adapter walls.

The first MAF used was the 3" Slot Style Pro-Tube by Pro-M Racing shown in Fig. 67a. The housing for this MAF was simply a tube and did not have a curved



Figure 67. (a) 3” Slot Style Pro-Tube MAF by Pro-M Racing, (b) Pro-M 92 High Performance MAF with Inlet and Flow Straightener

bell-mouth inlet as one would find for a turbojet engine. Since this MAF was not equipped with a proper inlet, it caused significant pressure drop through the MAF when engines were operating at the design point. This led to a reduction in thrust. To correct this issue, new MAF with a bell-mouth inlet was selected, the Pro-M 92 Mass Air Meter by Pro-M Racing, seen in Fig. 67b. This high performance MAF provided the necessary measurement without significantly disrupting the flow.

The MAF manufacturer provided calibration tests that indicated the sensor output at various mass air flow rates. The calibration data from the manufacturer is shown in Fig. 68. A third-order polynomial curve fit was used to create a trendline of the data so that a measured output voltage could be converted to a mass air flow rate. Unlike thermocouples, load cells, or most other instruments used in this research, the MAF had no published uncertainty since it was not intended for a laboratory setting. When determining the uncertainty of the MAF calibration curve, errors at mass flow rates in excess of the maximum mass flow rate observed do not need to be considered. The maximum mass flow rate seen in this research was 0.6 kg/s. Fig. 68 shows the calibration data that was used to build the trendline. This data encompasses the operating range of all engines tested. The uncertainty can be calculated by evaluating the trendline at each voltage for which there is a calibration point. Then by taking the

absolute value of the difference between the calculated mass flow rate and the mass flow rate according to the calibration data, the error of the trendline can be found. These results are shown in Fig. 69 For simplicity, largest error will be considered the uncertainty under all operating conditions. Therefore, the MAF measurement uncertainty was 0.9%.

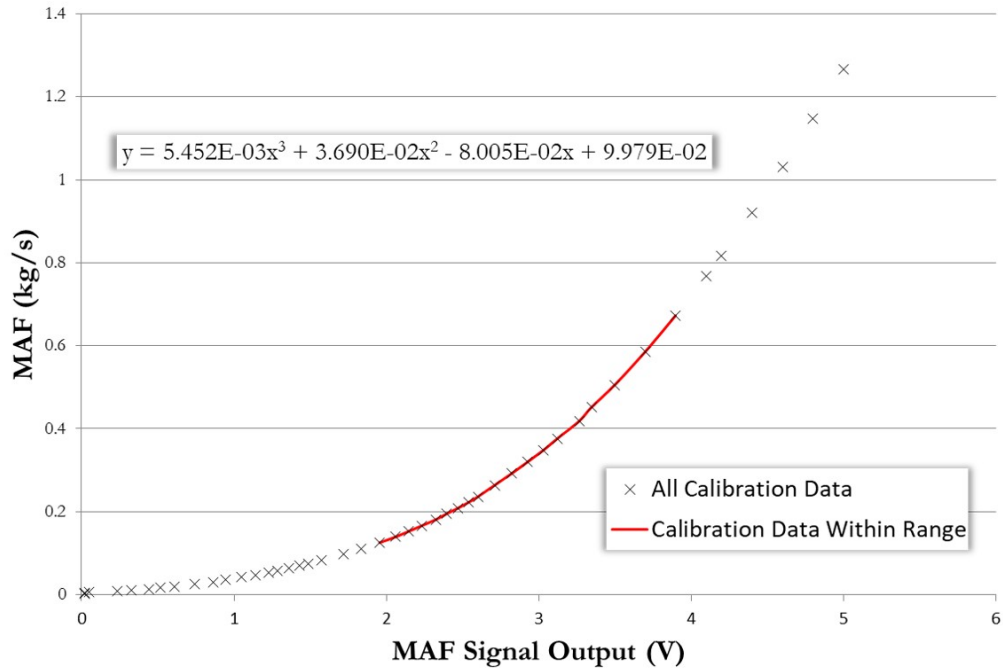


Figure 68. Calibration Data from MAF manufacturer overlaid with trendline. Trendline is based only on data that lies within the bounds of engine performance.

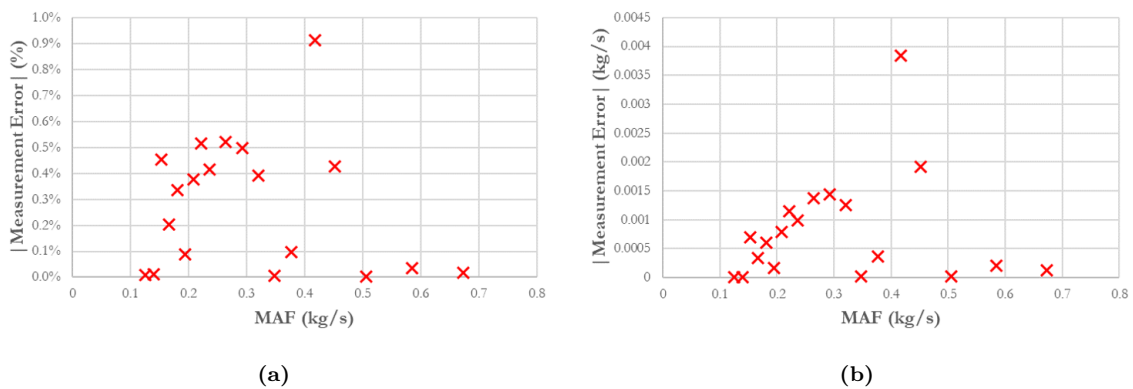


Figure 69. Error of MAF Calibration Curve against Calibration Data presented as: (a) Percentage of the Manufacturer’s calibration mass flow rate and (b) mass flowrate (kg/s).

3.4.3 Internal Instrumentation: Temperature and Pressure.

Turbojet performance is dependent on the atmospheric conditions. Since the experiments involved in this research were conducted on different days, it is necessary to correct for variations in the experimental atmospheric conditions. Important engine performance metrics can be corrected to standard conditions using Equations 62 [24]:

$$F_c = \frac{F}{\delta_0} \quad S_c = \frac{S}{\sqrt{\theta_0}} \quad \dot{m}_{fc} = \frac{\dot{m}_f}{\delta_2 \sqrt{\theta_2}} \quad \dot{m}_{ci} = \frac{\dot{m}_i \sqrt{\theta_i}}{\delta_i} \quad N_{ci} = \frac{N}{\sqrt{\theta_i}} \quad (62)$$

Accurate measurement of the ambient pressure and temperature is crucial for properly correcting engine performance. The ambient air is quiescent, so static and total properties are equivalent. When this research began, ambient pressure was read from a barometer in the control room and ambient temperature was read as the average temperature of the thermocouples used to instrument the engine. In the winter, it was realized that temperature varied significantly within the test cell. To ensure that ambient conditions were measured accurately, it was realized that designated ambient instrumentation was needed throughout the duration of the test. An absolute pressure transducer was put in place to measure P_0 .

For measuring ambient temperature the resistance bulb thermometer, recommended by Walsh and Fletcher, is an attractive option because it offers lower uncertainty than a thermocouple [44]. These thermometers are fragile. Considering the high volume of traffic in the labs by multiple research groups, a K-Type thermocouple was chosen to measure the ambient temperature. This thermocouple was positioned near the engine inlet so that the temperature of air being ingested by the engine could be sampled throughout the test. It was found that temperatures dropped over the course of a

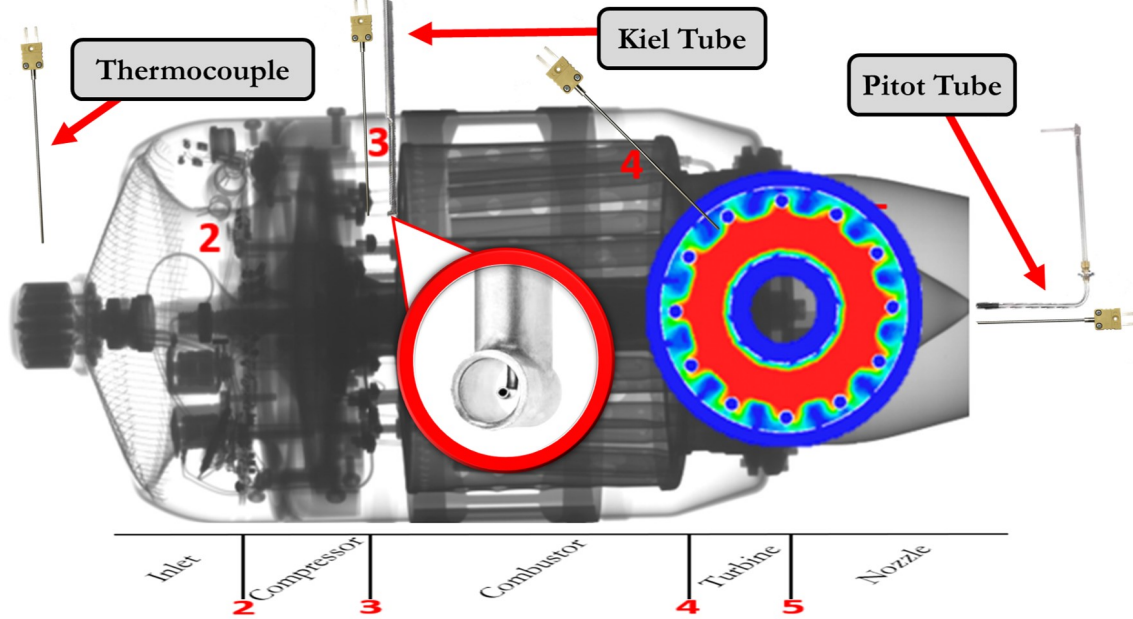


Figure 70. Instrumentation diagram overlaid on CT scan of Engine B. Thermal profile of turbine inlet conditions is appended from Ref. [13]

single test by over 5K when testing during the winter as cold outdoor air was pulled into the test cell.

Temperature measurements were made using ungrounded, shielded K-Type thermocouples. While exposed thermocouples provide faster response times and in effect, better measurement of transient temperatures, the testing conducted was only concerned with steady state engine operation. Furthermore, the shielding provided additional protection from the high velocity flow. Damaged instruments inside the engine could result in FOD and potential damage to the engine. Additionally, the ungrounded thermocouples have an advantage over grounded thermocouples in this application because they provide insulation from radiation from the engine casing or components [40].

In addition to the ambient conditions, temperature and pressure data was collected at engine stations 3, 4, and 9. This data was used to evaluate component performance. A diagram of the instrumentation layout is provided in Fig. 70. Experimental analysis

of microturbine engines is difficult due to the geometric constraints of the engine. In larger engines, test probes are relatively small compared to the flow passages, and rakes of probes can be placed within the engine to resolve non-uniform gas properties. In microturbines, probes can be relatively large and can potentially cause significant disturbance since the flow passages are so narrow in these engines [15]. Fig. 71 shows a thermocouple positioned in front of the nozzle guide vane (station 4). This issue is compounded if multiple probes are positioned at the same station. Therefore, no redundant instrumentation was used.

To measure the total pressure at station 3, a Kiel probe was used. Kiel probes are variants of Pitot probes that measure total pressure and are relatively insensitive to the orientation of the flow for yaw up to 40° [19]. This makes Kiel probes ideal for use inside of the engine since instrument alignment can be difficult. One Kiel tube was positioned at station three and connected to a 100 psia pressure transducer. Specifications for the instruments used in this research are provided in Table 9. In addition to this Kiel Tube, a thermocouple was used at this location to measure the temperature of the flow leaving the diffuser. The thermocouple and Kiel tube were placed at the same depth and at adjacent circumferential locations in an attempt to keep uniform properties between the two sampling locations.

Table 9. Instrument specifications.

Instrument	Brand	Part No.	Range	Accuracy
K-Type Thermocouple	Omega	KMQIN-062U-12	0-920 °C	0.75%
Pressure Transducer	Omega	PX419-050A5V	0-50 psia	0.08%
Pressure Transducer	Omega	PX419-100A5V	0-100 psia	0.08%
MAF	Pro-M Racing	Pro-M 92	0-1.3 kg/s	0.9%
Fuel Flow Meter	Max Machinery	P213	0-1.82 L/min	0.2%
Load Cell	Omega	LCCD-100	0-100 lbf	0.03%
Load Cell	Omega	LC103B-200	0-200 lbf	0.02%
Freq. to Analog Converter	Red Lion	IFMA	+/- 90 V	0.2%



Figure 71. Thermocouple positioned in front of NGV, illustrating relatively large size of the thermocouple to the passage size.

To measure temperature at station 4, the turbine inlet, a single thermocouple used. This thermocouple was inserted at a 45° angle so that it could pass through a dilution hole and sample the turbine inlet. Due to the patternation discussed in Chapter 2, there were concerns that the measured temperature was not representative of the average temperature at the turbine inlet. Therefore, this method was supplemented with an analytic method of determining temperature using Equation 63.

$$h_{t4} = \frac{f\eta_b h_{pr} + h_{t3}}{1 + f} \quad (63)$$

This equation relies on measurements for mass air flow rate, mass fuel flow rate, and the temperature at station 3; accurate measurements were achieved for each of these parameters. This analytic technique required a combustor efficiency to be assumed. Based on previous SERL experience, $\eta_B = 95\%$ was assumed, but values on the range of 90-95% would have been acceptable.

Finally, to measure gas properties downstream of the turbine, a pitot tube was used to collect total and static pressures and a thermocouple was used to collect temperature data. The instruments were placed at the nozzle exit plane as shown in Fig. 72. Use of isentropic flow relationships, shown in Equation 64, allowed for exit

Mach number to be calculated based on the static and total pressure measurements from the Pitot Tube.

$$\frac{P}{P_t} = \left(1 + \frac{\gamma - 1}{2} M^2\right)^{-\frac{\gamma}{\gamma - 1}} \quad \rightarrow \quad M = \sqrt{\frac{2}{\gamma - 1} \left[\left(\frac{P}{P_t}\right)^{-\frac{\gamma - 1}{2}} - 1 \right]} \quad (64)$$

To measure the static pressure, a 50-psia pressure transducer was used. To measure the total pressure, a 100-psia pressure transducer was used. Three concerns were raised regarding the quality of pitot tube measurements at the nozzle exit. First, pitot tubes are significantly more sensitive to misaligned flow than Kiel tubes and can only make accurate measurements up to a few degrees of misaligned flow. This is

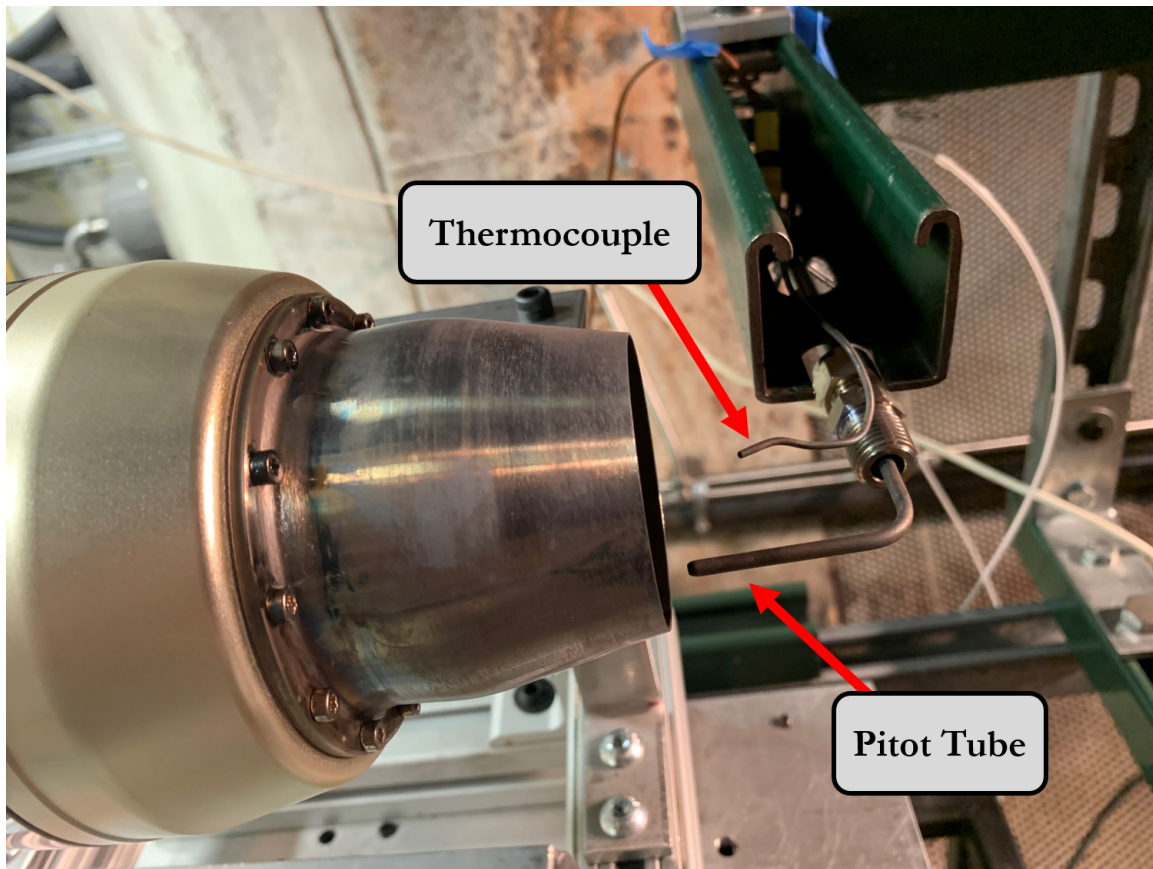


Figure 72. Pitot Tube and Thermocouple at nozzle exit plane.

a concern due to any residual swirl left from the turbine. Second, like the combustor and turbine measurements, distortions in the flow may continue to exist. The magnitude of distortions will hopefully be less significant due to mixing and dissipation in the nozzle. Finally, concerns were raised regarding the presence of a bow shock over the Pitot tube. A review of the measurements saw no discontinuities in the data to indicate the development of a bow shock over the Pitot tube.

3.5 Uncertainty Analysis

In interpreting the data collected during this research, Moffat’s uncertainty analysis technique was used to determine measurement uncertainty. Using Moffat’s methods, the notation $X \pm \delta X$ indicates that the measurement, X , has an uncertainty of δX . When calculating a result, R , based on N experimental measurements, Moffat recommends combining the effects of measurement uncertainty using a root-sum-square method shown in Equation 65 [27]:

$$\delta R = \sqrt{\sum_{i=1}^N \left(\frac{\partial R}{\partial X_i} \delta X_i \right)^2} \quad (65)$$

where δR is the uncertainty in the calculated result, R . This equation was used consistently throughout this research. The results of the uncertainty analysis are presented as error bars on each data plot.

The same RSS technique is used when multiple instruments are used in series to make a single measurement. In this scenario, the elemental uncertainty of each instrument must be combined in order to properly qualify the measurement. This is necessary in the case of measurements such as the fuel flow rate. The flow rate is measured by a flow rate meter, and an output signal is generated as a frequency. The DAQ used measures signals from 0-5 Volts. The frequency to analog converter

was used to convert the frequency signal into a voltage. The flow meter and the frequency to analog converter both have uncertainty associated with them. Therefore, the uncertainty of the flow rate measurement must be a combination of the two elemental uncertainties: the uncertainty from the flow meter and the uncertainty from the frequency converter. This combination is shown in Equation 66:

$$u_{\text{flow rate}} = \sqrt{(u_{\text{flow meter}})^2 + (u_{\text{freq. converter}})^2} \quad (66)$$

IV. Results

The experimental results for this research are presented in this chapter. In Section 4.1, the overall engine performance will be discussed. Engine performance will be compared to published values of thrust and fuel consumption. Additionally, the four engines considered in this research will be compared to one another. In Section 4.2, results and analysis for specific engine components will be discussed. Due to limitations discussed in this section, the bulk of the analysis is focused on the compressor. Regarding the combustor and turbine, specific experimental difficulties that were encountered are discussed. In lieu of the desired experimental results, analytic techniques were used to estimate turbine performance based on overall engine performance. Section 4.3 discusses the potential performance achievable with recreation-grade turbojets based on the technology surveyed. Commercial engines are compared to the Hamilton Sundstrand TJ-50 military-grade turbojet to evaluate if recreation-grade engines have the ability to meet military performance specifications. Finally, results concerned with the two secondary research objectives are presented. The effects of instrumentation are reviewed in Section 4.4. The variation in performance between same-make, same-model engines is discussed in Section 4.5. The implications of the results regarding these supplemental research objectives are discussed in relationship to the results presented in Sections 4.1 and 4.2.

4.1 Overall Performance

In this section, measured engine performance will be compared to the performance claims published by the manufacturer. In SERL's past work with small piston engines, performance measured in the lab often did not align with the manufacturer's claims. Due to this experience, all performance metrics must be experimentally verified. In

addition to validating published engine performance, the engines tested in this study will be compared with one another. The data used for these comparisons establishes the range of performance that can be found in recreation-grade microturbine turbojets. The overall performance will be presented in two sections. The first will present thrust related performance: thrust, mass air flow, and three normalizations of thrust. The second section will present the results pertinent to fuel consumption rates.

4.1.1 Thrust and Mass Air Flow.

In this section, thrust measurements for each engine are presented and compared to the manufacturer's published performance. Throughout this document, measured performance is generally presented in a common format. This format is used first in Figure 73. Each engine is identified by a unique color. Magenta, blue, green, and red represent Engines A, B, C, and D, respectively. Markers on these plots represent the average value of 5-10 seconds of data gathered at 10 Hz. Error bars are included where appropriate.

The corrected engine speed is presented along the horizontal axis. Engine speed is presented as a percentage of the published maximum speed or *design speed*. Within this work, the maximum speed was considered to be the design operating condition. By presenting engine speed as a percentage of the design speed, the design points of each engine align vertically, making comparisons between engines more apparent. Engines were not tested exactly at their design speed. This is partially attributed to variations in atmospheric test conditions. These engines regulate their speed based on the true engine speed, not based on the corrected speed. This allows these engines to operate at corrected engine speeds higher than the design speed when ambient temperatures are colder than 288.15 K. Since data was generally not gathered at the design point, a curve-fit was necessary for interpolating or extrapolating engine per-

formance. These curve-fits are represented as dashed curves. Finally, on some graphs, the design point performance will be identified as a black “x”, and the published data will be vertically offset from this point and indicated by a gold star.

As seen by the data presented in Figure 73 and Table 10, the data indicates that each engine produced less than the published thrust. Thrust deficiencies were 2-7.5% of the published thrust. The measurement uncertainty associated with the air-bearing thrust stand (5%) was relatively large compared to the discrepancy between published and measured thrust. While it seems likely that the engines tested produce up to 7.5% less thrust than advertised, more accurate thrust data is needed to confirm

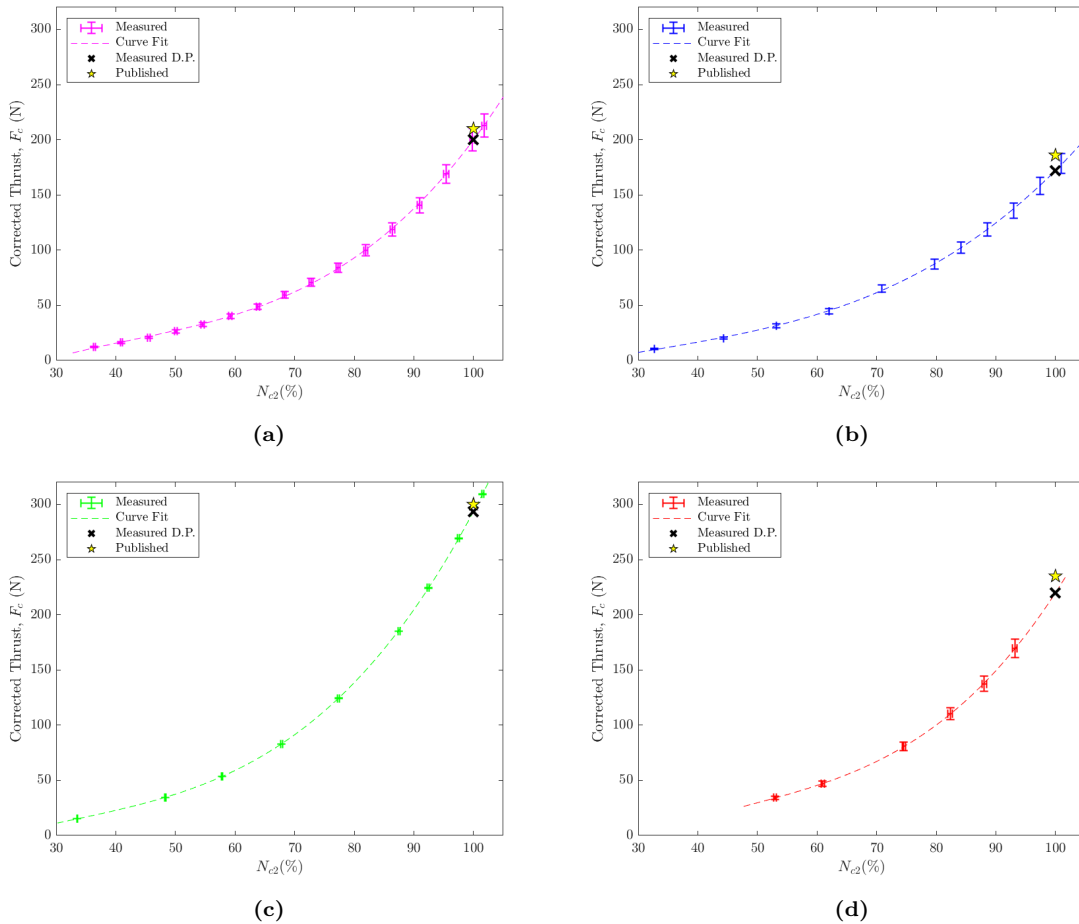


Figure 73. Measured corrected thrust compared to the manufacturer’s published performance data.

Table 10. Measured vs. Published Thrust.

Engine	Thrust (N)		
	Meas.	Pub.	Δ (%)
A	200	210	-4.8
B	172	186	-7.5
C	293	300	-2.3
D	220	235	-6.4

this. With the current data, only up to a 2.5% discrepancy between measured and published thrust can be confirmed. The upgraded flexure-based thrust stand has an order of magnitude improvement in accuracy. Additional testing of Engines A, B, and D would provide data with thrust uncertainty similar to that of Engine C. The improvement in measurement accuracy can be seen by comparing the error bars in Figure 73c to the thrust data of Engines A, B and D.

Equations for the trendlines relating thrust to $N_{c2}(\%)$ are provided in Table 11. A third order polynomial curve-fit tool was used (MatLab's *fit* command). The trendlines are given in the form, $y = p_1x^3 + p_2x^2 + p_3x + p_4$, where $y = F_c$ and $x = \frac{N_{c2}}{N_{d.p.}} \times 100\%$. The empirically-determined, design-point thrust is calculated by evaluating the corrected thrust curve fit at 100%.

Table 11. Trendlines relating corrected thrust (N) to corrected engine speed (% of design speed) for each engine.

Engine	p1	p2	p3	p4
A	6.017E-4	-7.649E-2	4.371	-75.44
B	3.431E-4	-3.449E-2	2.062	-36.45
C	4.669E-4	-3.264E-2	1.543	-20.03
D	8.418E-4	-1.212E-1	7.238	-134.5

4.1.1.1 Normalizations of Thrust.

For each of the following thrust normalizations, the experimentally-determined, design-point thrust was used. The first normalization of thrust is the thrust to weight ratio, T/W. Like all other engine parameters, engine weight was measured in-house. Comparisons of the measured engine weight to the published engine weight are provided in Table 12. The significant discrepancy between measured and published weights for Engines B and C is in part due to what is included in this weight measurement. Engine weight is not an industry-standardized metric, and these engines are not well regulated. There are a variety of accessory components that are necessary for engine operation (pumps, fuel valves, Engine Control Units, RPM sensors, starter motors, etc.). If a company chooses not to include these in their measurement of engine weight, engine weight will be artificially low. The measured weight, found in Table 12, includes all components necessary to operate the engine excluding the battery. The battery was excluded from this calculation because variations in capacitance will significantly distort the T/W of the engine. Engines A, B, and D, each required a 3s LiPo battery. Engine C required both a 3s LiPo battery in addition to a 6s LiPo battery. As indicated by the $\Delta\%$ column of Table 12, the manufacturers of Engines B, C, and D were not including accessory components in their measurement of engine weight.

Table 12. Measured vs. Published: Engine Weight & T/W.

Engine	Weight (N)			T/W		
	Meas.	Pub.	Δ (%)	Meas.	Pub.	Δ (%)
A	24.6	24.8	-0.81	8.1	8.5	-3.99
B	17.7	14.3	+23.8	9.7	13.0	-25.29
C	35.3	26	+35.8	8.3	11.5	-28.06
D	32.6	30.4	+7.24	6.7	7.7	-12.70

Using the measured thrust and weight data, T/W can be determined for each engine. Table 12 presents the measured T/W and provides a comparison to the published values. From Tables 10 and 12, it is apparent that the difference between the measured and published weight is the main driver behind the large decrease in T/W for Engines B, C, and D.

Based on previous lab experience, T/W for each engine was expected to be approximately 8. The significantly higher published T/W values of Engines B and C were one factor that motivated research regarding their performance. As seen in Table 12, the measured values for T/W are much closer to the expected value. Despite this significant reduction in T/W, Engine B maintains a notably high T/W of 9.7. Later sections will explain how this high performance is achieved in Engine B, but it can be attributed primarily to hotter combustor temperatures. In addition to performing well in terms of T/W, Engine B also achieves high performance in terms of T/A.

While thrust to weight is a common metric used throughout aeronautical engineering, T/A is less common. T/A is most frequently used to describe and compare small attritable turbojets [16]. These engines are typically employed on high speed missiles which seek small frontal areas in order to minimize drag. The T/A performance metric is created by normalizing the thrust by the maximum area seen when viewing the engine axially. Therefore, this area can be calculated using the maximum diameter of the engine, as seen in Figure 74. Values for T/A can be found in Table 13 along with the diameters used to calculate frontal area for each engine.

Table 13. Thrust per frontal area, T/A.

Engine	D_{max} (cm)	A_{max} (cm ²)	T/A (kPa)
A	13.3	139	14.4
B	11.0	94.2	18.3
C	13.3	139	21.0
D	12.9	131	16.8

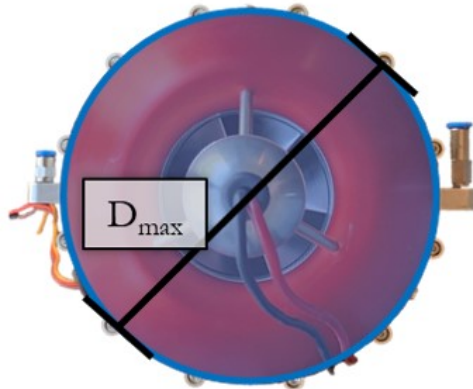


Figure 74. Frontal Area (Engine D)

At face value, it seems that Engine C is the highest performer with respect to T/A. Consulting the published data in Figure 75, it becomes apparent that higher T/A are more easily achieved with larger, higher-thrust engines. Overlaying the data collected in this research onto Harris's data for expendable turbojets, Figure 75, provides a new perspective regarding the performance of the commercial engines [16]. The data in Figure 75 indicates that the recreation-grade engines tested in

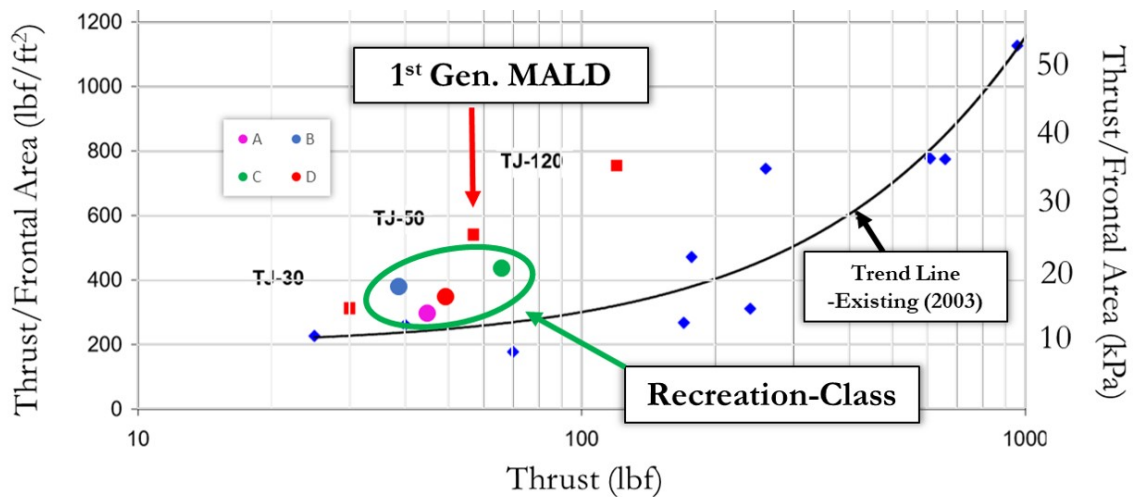


Figure 75. Thrust Per Frontal Area. Data from the four engines tested is overlaid on early 2000's state of the art microturbine turbojets. Appended from [16]

this work lie beneath Hamilton Sundstrand's TJ-50, but above their competitors, presumably other military-grade attritable turbojets. Considering that Engine B has only half the thrust of Engine C, its T/A is fairly high, seeming to fall on the same trendline as Hamilton Sundstrand's military-grade engines. Therefore, it is possible for commercial engines to achieve comparable T/A performance as military-grade engines. However, as will be shown in Section 4.1.2, increasing thrust per frontal area comes at the expense of specific fuel consumption.

The final normalization of thrust that discussed is specific thrust, F/\dot{m}_0 . Since thrust and mass air flow were both measured directly, determining specific thrust is a straightforward calculation based on corrected thrust and corrected mass air flow. Figure 76 shows that, with respect to thrust and mass air flow rate, Engine C has the highest measurements, and Engine B has the lowest. Engines A and D are between the two extremes. With respect to the thrust measurements shown in Figure 76a, the two engines are within measurement uncertainty.

For engines tested on the air-bearing thrust stand, the 5% uncertainty in thrust measurements creates a comparable uncertainty in specific thrust. The results in Figure 77 indicate that the specific thrust of Engines A, B, and D is approximately 500 ± 25 N/[kg-s] at the design point. The relatively large measurement uncertainty prevents engines from being distinguished based on specific thrust. Recall that the new flexure-based thrust stand had an improved accuracy, and that thrust on this system can be measured to $\pm 0.25\%$. Since Engine C was tested on the flexure-based thrust stand the accuracy of the specific thrust measurement for this engine was limited by the accuracy of the mass air flow meter, 0.9%. Therefore, the specific thrust accuracy for Engine C was 0.93%. Comparing the uncertainty bars for Engine C to those of the other three Engines illustrates the effect of improved thrust accuracy on resolving specific thrust data.

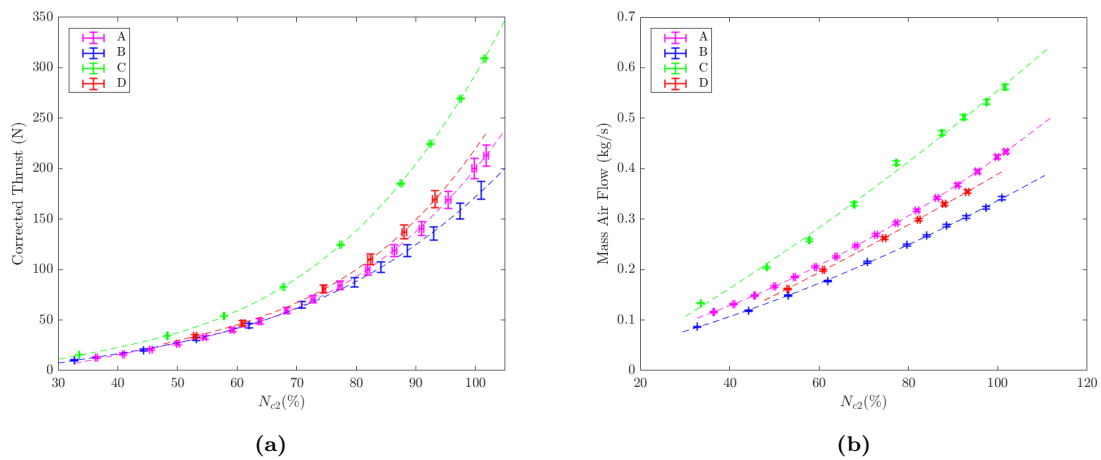


Figure 76. Experimental results for corrected thrust and corrected mass air flow for all four engines.

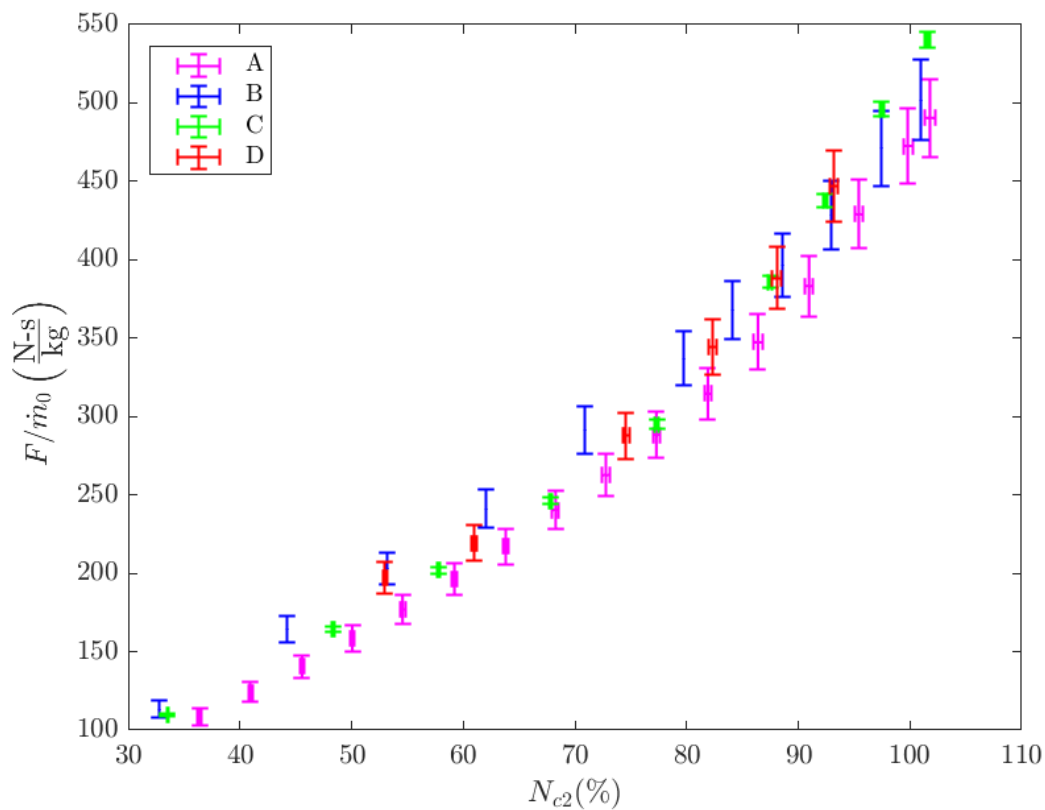


Figure 77. Specific thrust for all four engines.

As shown in Section 2.7, F/\dot{m}_0 has units of speed. Therefore, specific thrust can be used to determine the jet power, P_{jet} , given by Equation 67. Jet power can be used to determine engine efficiency by comparing against the fuel power, P_{fuel} , given by Equation 68. From these two terms the jet efficiency, η_{jet} , can be determined. The jet efficiency, given by Equation 69, indicates how much of the energy stored in the fuel was converted into kinetic energy.

$$KE_{jet} = \frac{1}{2}mV_9^2 = \frac{1}{2}m \left(\frac{F}{\dot{m}_0} \right)^2 \quad \longrightarrow \quad P_{jet} = \frac{1}{2}\dot{m}_9 \left(\frac{F}{\dot{m}_0} \right)^2 \quad (67)$$

$$P_{fuel} = \dot{m}_f h_{PR} \quad (68)$$

$$\eta_{jet} = P_{jet}/P_{fuel} \quad (69)$$

Jet efficiency served as a useful metric for comparing overall engine design. As seen in Figure 78, Engine D was the most efficient engine and Engine B was the least efficient. Engines A and C operated within $\pm 1\%$ efficiency with error bars on the same

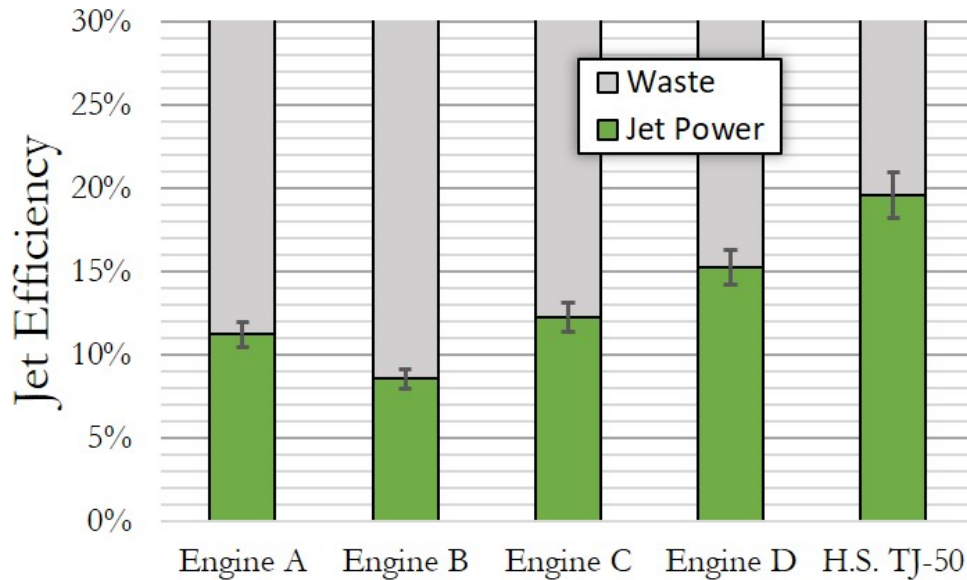


Figure 78. Overall engine efficiency based on jet power. H.S. TJ-50 calculations based on data from Ref. [16].

order of magnitude. Recalling the T/W and T/A results, it becomes apparent that the high thrust performance of Engine B was accompanied by poor engine efficiency. Notice that a fifth engine, the Hamilton Sundstrand TJ-50, is presented in Figure 78. This engine represented a military-grade engine within the same thrust class as the commercial engines tested. All data regarding the H.S. TJ-50 presented in this report was based on information published by the manufacturer in Reference [16].

4.1.2 Fuel Consumption.

The analysis for engine fuel consumption rates will be presented similarly to that of the thrust data. First, measured fuel consumption rates will be presented and compared to published data. From those measurements, trendlines will be created to describe fuel consumption throughout the entire engine operating regime. Finally, fuel consumption will be normalized by thrust, producing the specific fuel consumption performance metric.

It was found that the difference between measured and published fuel consumption rates was much larger than the discrepancies in thrust measurements. While thrust measurements were all within 2-7% of the published performance, fuel consumption rates were closer to 10% higher than published values, excluding Engine B. The measured fuel consumption for Engine B was 45% greater than the published values. The results for fuel consumption are presented in Figure 79 and Table 14. Curve-fits for fuel consumption as a function of % design speed are provided in Table 15.

Fuel consumption rates for the four engines tested are compared to each other in Figure 80. Referring back to the comparisons of thrust shown in Figure 76a, it becomes apparent that Engine C has the highest thrust and the highest fuel consumption, a sensible connection. The next highest fuel consumption rate is that of Engine B. Consulting Figure 76a, Engine B has the lowest thrust. This indicates that En-

Table 14. Measured vs. Published Fuel Consumption. *Off-design point.

Engine	Fuel Consumption (gpm)		
	Meas.	Pub.	$\Delta(\%)$
A	579	525	+10
B	568* (699)	392*	+45* (+78)
C	866	804	+7.7
D	559	515	+8.5

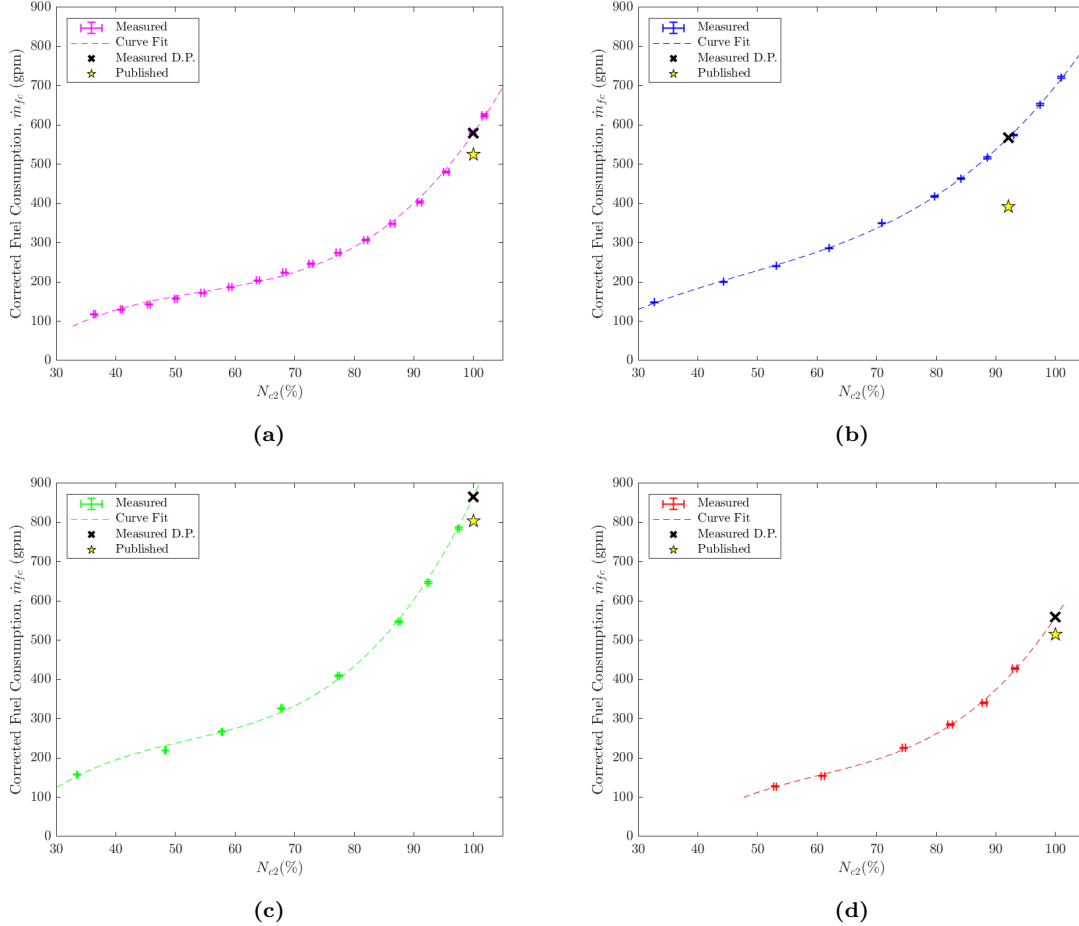


Figure 79. Measured corrected fuel consumption compared to published data.

Table 15. Trendlines relating corrected fuel mass flow rate (kg/s) to corrected engine speed for each engine.

Engine	p1	p2	p3	p4
A	3.204E-03	-5.261E-01	3.14E+01	-4.87E+02
B	1.860E-03	-2.680E-01	1.737E+01	-1.960E+02
C	2.314E-03	-3.164E-01	1.885E+01	-1.966E+02
D	4.122E-03	-7.455E-01	4.887E+01	-9.791E+02

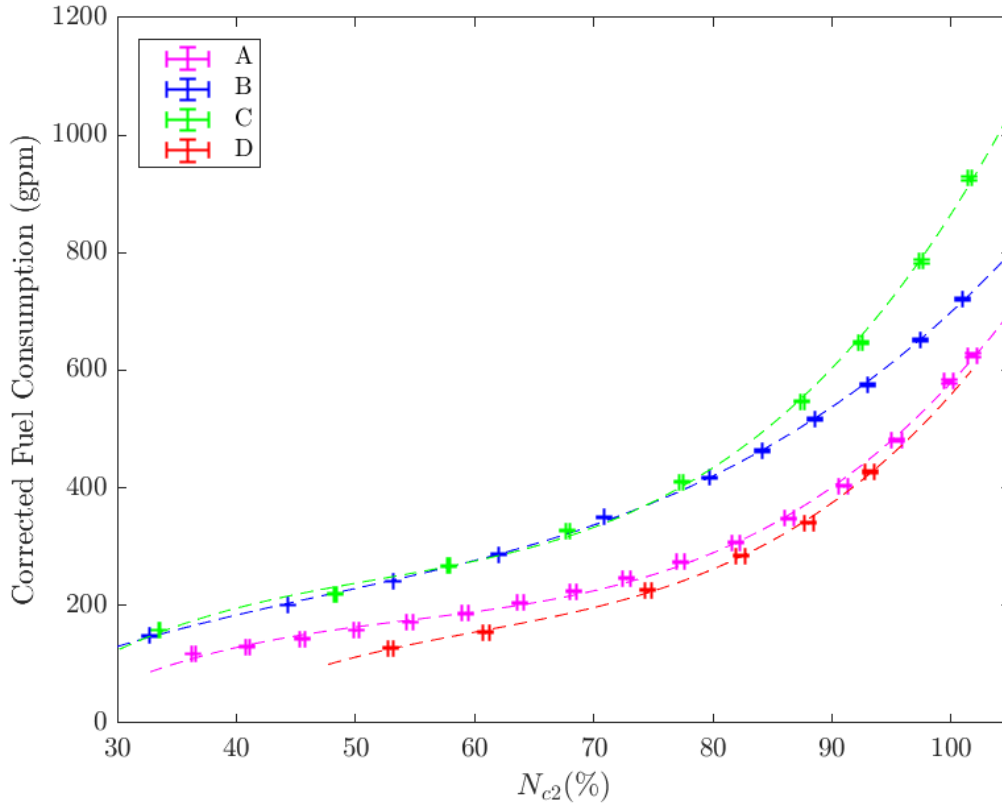


Figure 80. Corrected fuel consumption for all four engines.

gine B is significantly more inefficient than the other three engines. Ultimately, this inefficiency is the result of a low OPR, as will be shown in Section 4.2.1. This conclusion that can be further quantified by considering specific fuel consumption, shown in Figure 81a. Looking at the specific fuel consumption of these engines throughout the entire operating range, it is clear that Engine B has a high fuel consumption while Engines A, C, and D all converge to some lower limit of specific fuel consumption. Figure 81b presents the same data shown in Figure 81a, but only shows data collected near the design point. This perspective makes it apparent that Engine D has the best specific fuel consumption, while Engines A and C have slightly higher specific fuel consumption rates. The difference in performance between Engines A and C is smaller than the measurement uncertainty associated with fuel flow rate measurements. This

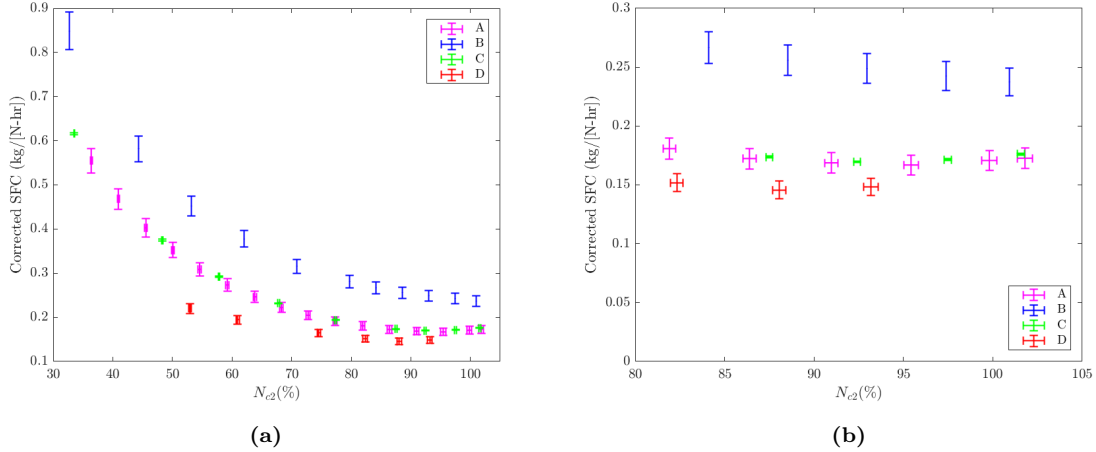


Figure 81. Experimental results for corrected specific fuel consumption for all four engines: (a) full operating range, (b) near design point.

data establishes a wide range of potential specific fuel consumption rate for commercially available turbojets: 0.15 - 0.25 kg/[N-hr]. Since specific fuel consumption is used in calculating range and loiter time, these values are crucial for determining the operational capabilities that can be met with commercial microturbine turbojets.

The results presented in this section provide ranges of measured performance that can be used in the future as a benchmark for performance available in the market for commercial microturbine turbojets. Published thrust aligned fairly well with the measured thrust data which ranged from 172 - 293 N. Several normalized thrust metrics were presented. T/W ranged from 6.7 to 9.7, and T/A ranged from 14.4 - 21.0 kPa, but was found to be sensitive to engine sizing. Specific thrust was found to be approximately 500 ± 25 N/[kg/s] for all four engines. Specific thrust data was used to calculate the jet efficiency as a metric for overall engine efficiency. This data indicated that efficiency for a commercial microturbine ranged from 8.5-15%. For Engine B, fuel consumption was found to vary significantly from published values. Since fuel consumption measurements for the other three engines were within 10% of the published data, it was assumed that the experimental methods used were sound. Therefore, the discrepancy between published and measured fuel consumption rates

likely stems from an issue with the manufacturer's data. Between all four engines, specific fuel consumption ranged from 0.15 to 0.25 kg/[N-hr]. Three of the four engines had specific fuel consumption rates between 0.15 and 0.17 kg/[N-hr]. Section 4.2 discusses component-level performance and provides insight regarding the differences in overall performance.

4.2 Component Performance

In this section, results regarding component performance are presented. Compressor performance is presented first for two reasons. First, the compressor is typically considered the driving component behind turbojet performance. Second, non-uniform flow patterns developed during the combustion process make it extremely difficult to determine combustor and turbine performance, especially with a single point-measurement per station. In order to provide an assessment of turbine performance despite this difficulty, analytic techniques were used to estimate turbine performance. Combustor performance was assumed based on the available literature.

4.2.1 Compressor.

It is useful to begin by recalling which instruments were used to provide data for this compressor analysis. The analysis begins with the ambient pressure and temperature measurements. Through the inlet, total temperature was assumed to be constant and total pressure was assumed to drop by 5% of the ambient pressure. Measurements for the compressor exit conditions were taken downstream of the diffuser and approximately halfway between the shaft and the outer casing of the engine. This allowed the measurements at engine Station 3 to account for the expansion through the dump diffuser. Additionally, it allowed the measurements to be taken in low-Mach flow. Thermocouple measurements taken in high-Mach flow tend to indicate

a temperature that is in between the static and total temperatures of the flow. By taking the measurement in a low-Mach flow, these effects can be ignored.

Beginning with the dimensionless analysis of compressor performance, expected values of compressor efficiency can be predicted. Using the Cordier Line discussed in Section 2.4.5, the specific speed and specific diameter can be used to estimate turbomachinery efficiency. The contours of constant efficiency presented in Figure 82 represent total-to-static efficiency. As discussed with the thermocouple measurement, because the exit measurements were taken in low-Mach flow, the difference between total and static values should be less than 5%. As seen in Figure 82, when considering these compressors in terms of dimensionless properties, all four compressors perform similarly. It can be inferred from Figure 82 that the efficiency of each compressor should be between 80 - 85%. This prediction is made independent of any pressure measurements; this is significant. When studying fluid thermodynamics, total temperatures indicate work interactions with the flow and total pressures are used to indicate losses. In other words, the total temperature reflects how much work was put into the flow, and the total pressure reflects how much work can be taken out of the flow. The discrepancy between these two measures of work is due to the increase in entropy. Since no pressure data is used in the dimensionless analysis, the Cordier Line provides an estimation of what the turbomachinery efficiency that is independent of the actual efficiency.

With this performance prediction in mind, the measured compressor efficiency results are presented in Figure 83. Notice the wide range of compressor efficiency, nearly a 15% spread. Efficiency results ranged from 0.65 for Engine B to just over 0.80 for Engine D. This creates a significant discrepancy from the predicted 0.80 - 0.85. It is unlikely that the turbomachinery used in these engines are less efficient than that which was used to develop the Cordier Line in 1953. The difference likely

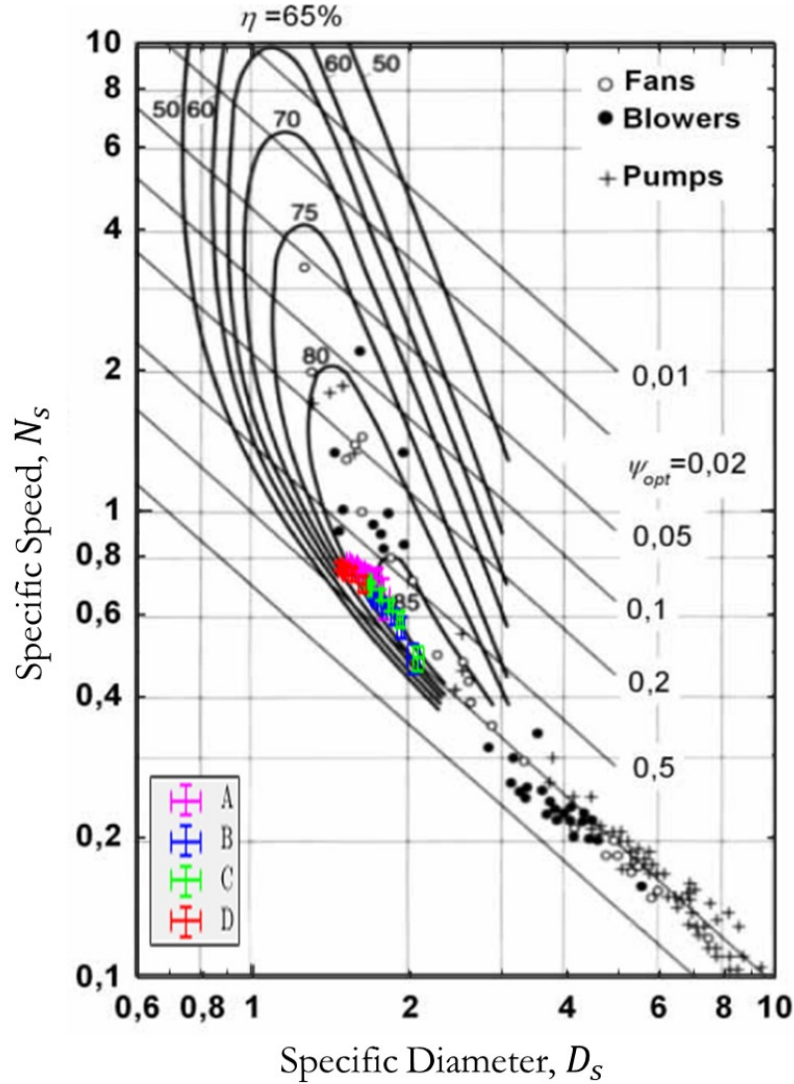


Figure 82. Original Cordier Diagram overlaid with measured compressor performance from each engine [8].

stems from diffuser performance. In the literature, centrifugal compressor performance is typically discussed in terms only of the impeller since the compression and diffusion processes are aerodynamically and thermodynamically unique. Figure 83 is annotated to identify the diffuser used by each engine. From this it is apparent that the two engines with airfoil diffusers were measured to have higher compressor efficiency than the two engines with wedge diffusers. There was not enough data present to isolate compressor impeller performance from diffuser performance. Therefore, no

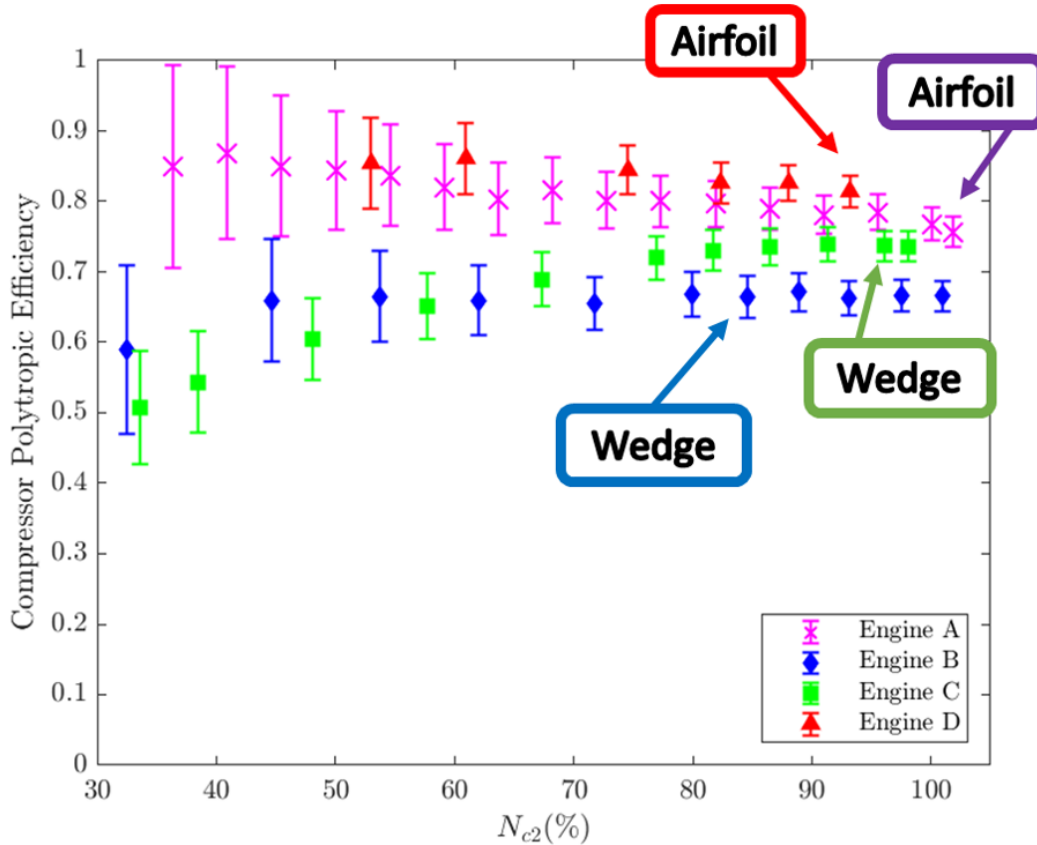


Figure 83. Compressor polytopic efficiency with annotations indicating diffuser type.

conclusions can be drawn quantitatively attributing the difference in performance to the diffuser. However, it allows a hypothesis regarding diffusers to be drafted to guide future research. From the data presented in this work, it seems that flow expanding through an airfoil diffuser experiences a smaller decrease in total pressure than does flow through a wedge diffuser. This would make the airfoil diffuser a more suitable choice for a turbojet compressor than a wedge diffuser. As a rule of thumb, wedge diffusers have a higher total-to-static pressure recovery: a desirable attribute for a turbojet since increasing static pressure increases combustion efficiency. However, wedge diffusers have the smallest stability margins. If the flowrate through the diffuser is too high, instabilities develop within the diffuser and high total pressure losses are incurred. This may be the cause for the significant reduction in efficiency from

the expected values. So while these microturbine engine designers may be utilizing wedge diffusers in an attempt to increase efficiency, the additional 10-15% decrease in compressor efficiency due to instabilities seems to be undermining their efforts.

In addition to the efficiency, the overall pressure ratio, OPR, developed by the compressor is used to describe compressor performance. Results for OPR throughout the operating range of each engine are presented in Figure 84. Instead of presenting OPR as a function of % design speed, it is presented as a function of compressor tip speed, U_t . This is due to the importance that the tip speed at the compressor exit plays in compression, shown by Equation 70.

$$OPR = \left(1 + \frac{\epsilon U_t^2}{g_c c_p T_{t1}} \right)^{\frac{e_c \gamma}{\gamma - 1}} \quad (70)$$

The other key variables in this equation are the polytropic efficiency, e_c , and the compressor slip factor, ϵ . Presenting OPR data in this form illustrates that a trade-off can be made between compressor geometry (slip-factor) and compressor efficiency in order to develop a desired pressure ratio. Several empirical correlations for slip factor were presented in Section 2.4.4. While the details in these correlations differ, they all reflect that increasing impeller blade count increases slip factor (indicating a decrease in compressor slip).

From the Euler Pump Equation, it is known that the work done by the compressor is a function of tip speed alone. Therefore, Figure 84 indicates the combined effect of ϵ and e_c on developing a pressure rise for a given amount of work. Figure 84 shows that the compressors of Engines A, B, and D all perform similarly with respect to this transition from work to pressure gain. Consulting Figure 83, it is apparent that the compressor of Engine B is 10-15% less efficient than those of Engines A and D, both of which have airfoil diffusers and 12 impeller blades. Engine B is able to achieve a similar relationship between OPR and U_t by increasing the number of impeller

blades to 16 which increases the slip factor, ϵ . This offsets Engine B's relatively low efficiency, e_c . If future research confirms that the diffuser is responsible for decreasing compressor efficiency, these engines demonstrate a method of overcoming that poor diffuser design by increasing blade count.

In order to verify these conclusions more data would be needed. The total pressure at the impeller exit would be needed to quantify the pressure drop in the diffuser and the slip experienced by the impeller. Employing the empirical correlations discussed in Section 2.4.4 provide a means of predicting impeller performance and allows some preliminary predictions to be developed. For this analysis, the correlation, $\epsilon = 1 - 2/n$ was used to determine slip factor. The results of this analysis are shown in Figure 85.

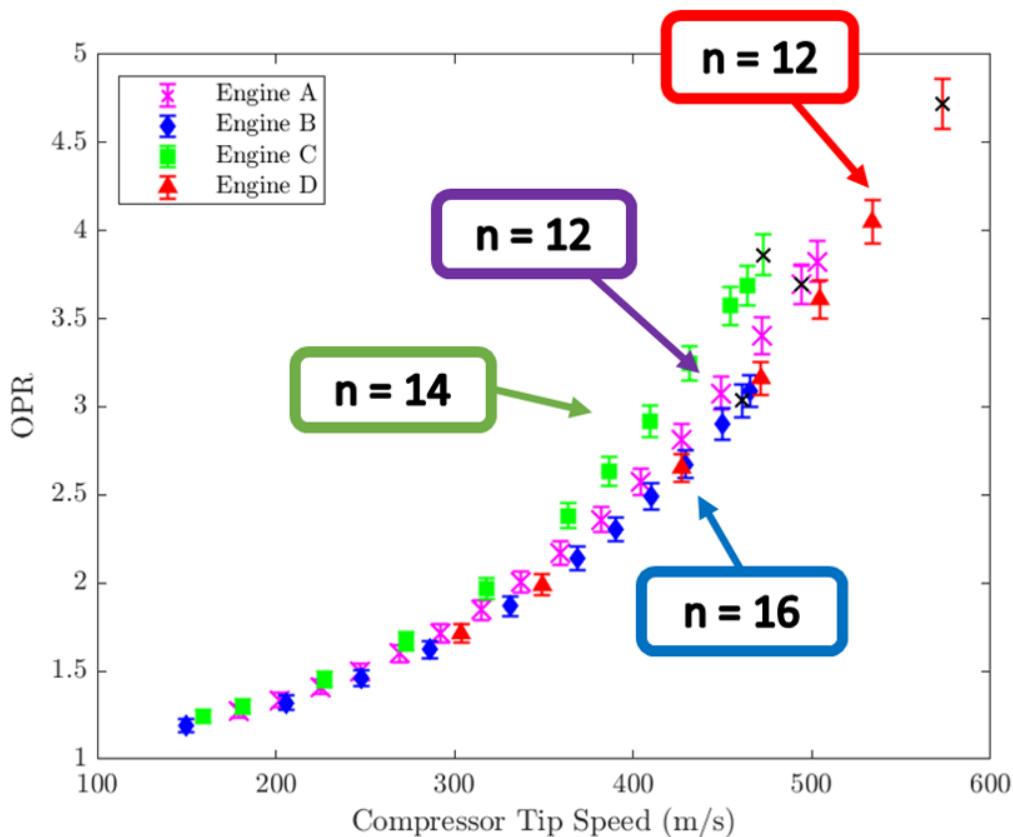


Figure 84. Compressor Overall Pressure Ratio with annotations indicating number of blades (including splitters).

Three data sets are plotted for each engine. The first is the theoretical maximum for compressor performance at the measured efficiency; this corresponds to $\epsilon = 1$. The next is the predicted pressure ratio at the compressor exit accounting for compressor slip. The third is the measured pressure ratio which includes losses developed during expansion through the diffuser. From these graphs, it seems that Engines A, B, and C have significant pressure drop through the diffuser. On the other hand, Engine D seems to have very little pressure drop through the diffuser. While Engines A and D are both categorized as airfoil diffusers, there is a significant gap in manufacturing and design quality that is apparent simply from visual inspection of both diffusers. Airfoil diffusers are effective when they utilize the lift force generated by the airfoil

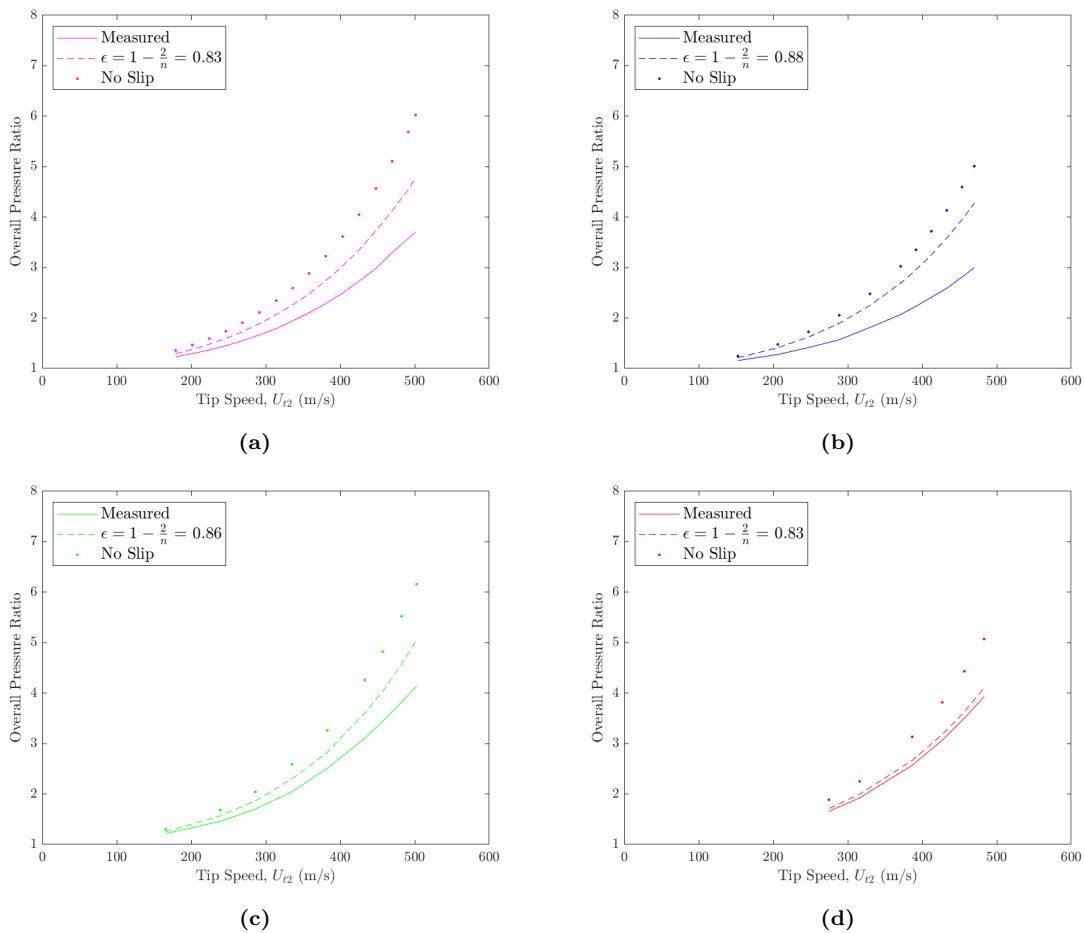


Figure 85. Prediction of diffuser pressure drop via empirical slip factor correlation.

to control the flow. Engine D utilizes smooth airfoil shapes throughout its diffuser. Engine A did not seem to have as effective a design. From visual inspection, it seemed that the cascades employed in Engine A were designed to physically re-route the flow rather than take advantage of the airfoil shape. Consequently, it seems that one could increase the OPR of Engines A, B, and C by 25-40% by replacing their diffuser designs with a well manufactured airfoil diffuser like Engine D. These results are preliminary and qualitative, but they offer strong motivation for future work to be focused on more accurately determining diffuser performance experimentally.

4.2.2 Combustor.

The combustor is a crucial engine component for microturbine turbojets and is also the most difficult component to instrument. Point measurements taken downstream of the combustor are not always indicative of the overall station properties. As stated in Section 3.4.3, a single thermocouple was used to measure temperature at the turbine inlet. The turbine inlet refers to Station 4 shown in Fig. 4 and indicates both the combustor exit and the turbine inlet. The temperature at this station varies significantly both spatially and temporally. Figure 86 shows the thermocouple data from two separate tests. Figure 86a shows fairly clean data, while the data in Figure 86b is much noisier. For context, each of these data plots shows a full engine test in which engine speed was increased incrementally until the engine reached full speed. Each increment increased speed by 5-10 kRPM and was allowed to settle into a steady state speed for 30-60 seconds. The red points indicate five seconds of data used to determine the average temperature at a given engine speed.

These data sets were collected with similar experimental setups. As was done in previous sections, data was sampled over 5-10 seconds and averaged to produce a time-averaged measurement for a given engine speed. Uncertainty in this measurement can

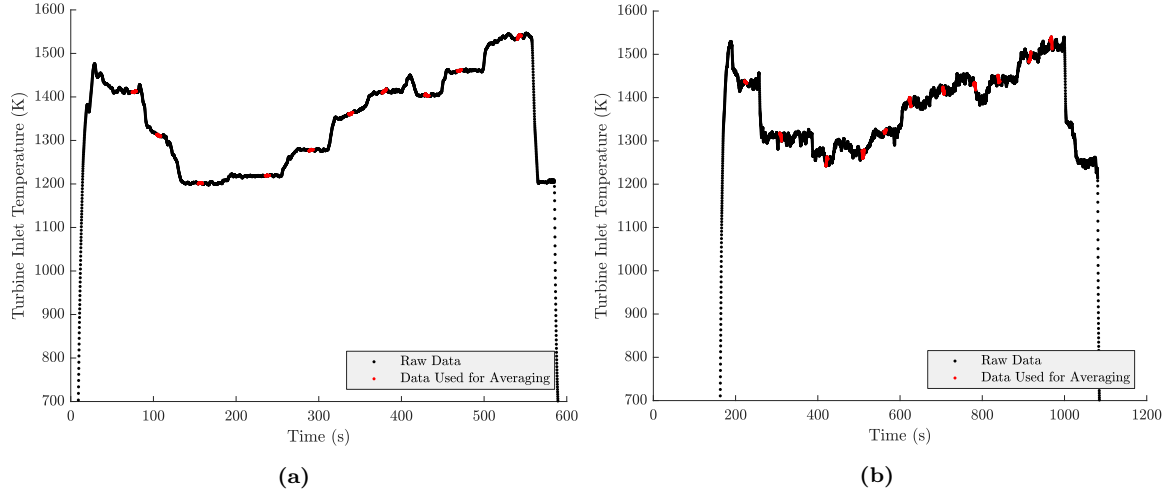


Figure 86. Stability of thermocouple measurements at turbine inlet.

be attributed to both instrument accuracy and to transient thermal behavior. Figure 87a shows the thermocouple readings at the turbine inlet for five tests of Engine B with error bars representing the accuracy of the K-Type thermocouple used. Figure 87b shows the same data set with error bars representing two standard deviations of the sampled data. In both cases, it was found that the temperature readings varied by significantly more than the measurement uncertainty. Readings were found to be accurate to $\pm 50\text{K}$ of the mean value sampled at this location. This large variation is indicative of the complicated aerodynamics and thermodynamics that lead to combustion instabilities that caused the engine to settle into a variety of thermal profiles at the turbine inlet.

Figure 88 overlays lines of constant combustion efficiency over the thermocouple data presented in Figure 87. These lines, defined by Equation 71, immediately highlight an issue with using a single thermocouple to determine turbine inlet temperature. Many of the data points in Figure 88 are above the 100% combustion efficiency line.

$$h_{t4} = \frac{f\eta_b h_{pr} + h_{t3}}{1 + f} \quad (71)$$

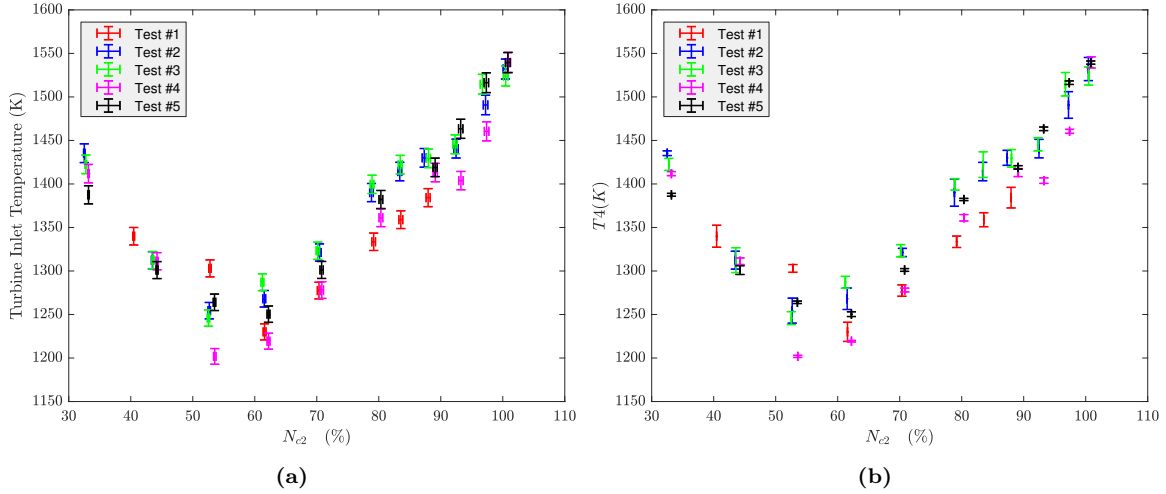


Figure 87. Uncertainty of thermocouple measurements at turbine inlet: (a) error bars indicate thermocouple accuracy, (b) error bars indicate 2 standard deviations of the five second data sample average to determine temperature at each engine speed.

Based on the location of markers relative to the lines of combustion efficiency, it is clear that the thermocouple was in a hot spot of the flow. Without using enough instruments to generate a profile of the temperature at the combustor exit, it is impossible to accurately determine the average exit temperature at Station 4.

In order to investigate spatial variation of temperature, the casing of Engine C was modified differently than the other engines. Access holes were bored so that multiple thermocouples could be placed in the nozzle guide vanes simultaneously. The results from one test of Engine C are presented in Figure 89. The probes were placed at similar depths but offset by approximately 30° . As shown by Figure 89, a consistent 200K difference between the two locations existed throughout the entire operating range of the engine. This represents up to a 20% drop in temperature across only 30° . From this data, it is readily apparent that many thermocouple measurements would be required to resolve the overall temperature at the turbine inlet. Proceeding with the engine analysis, a combustion efficiency of $\eta_b = 95\%$ will be assumed, and the turbine inlet temperature will be determined using the same method used to produce the lines of constant combustion efficiency in Figures 88 and 89.

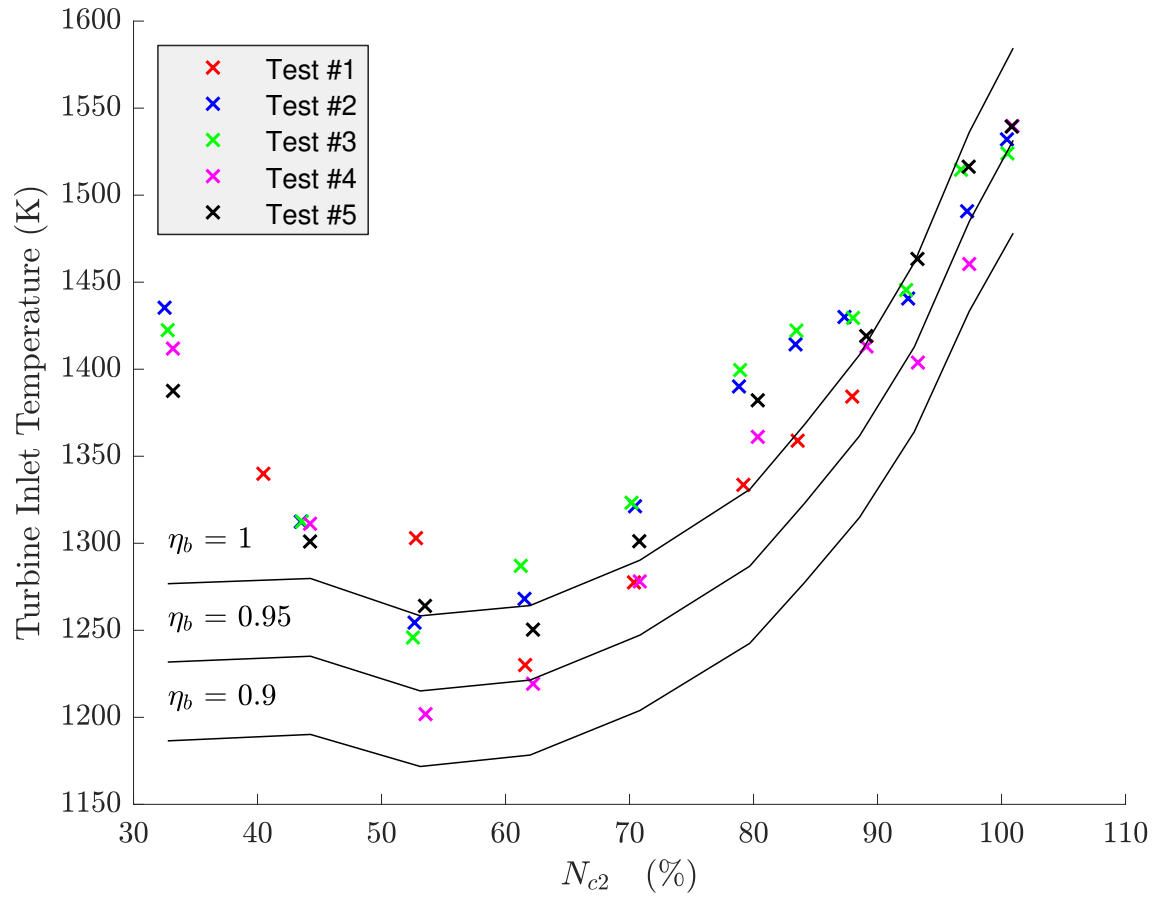


Figure 88. Turbine Inlet Temperature for Engine B measured over multiple experimental tests at same probe location.

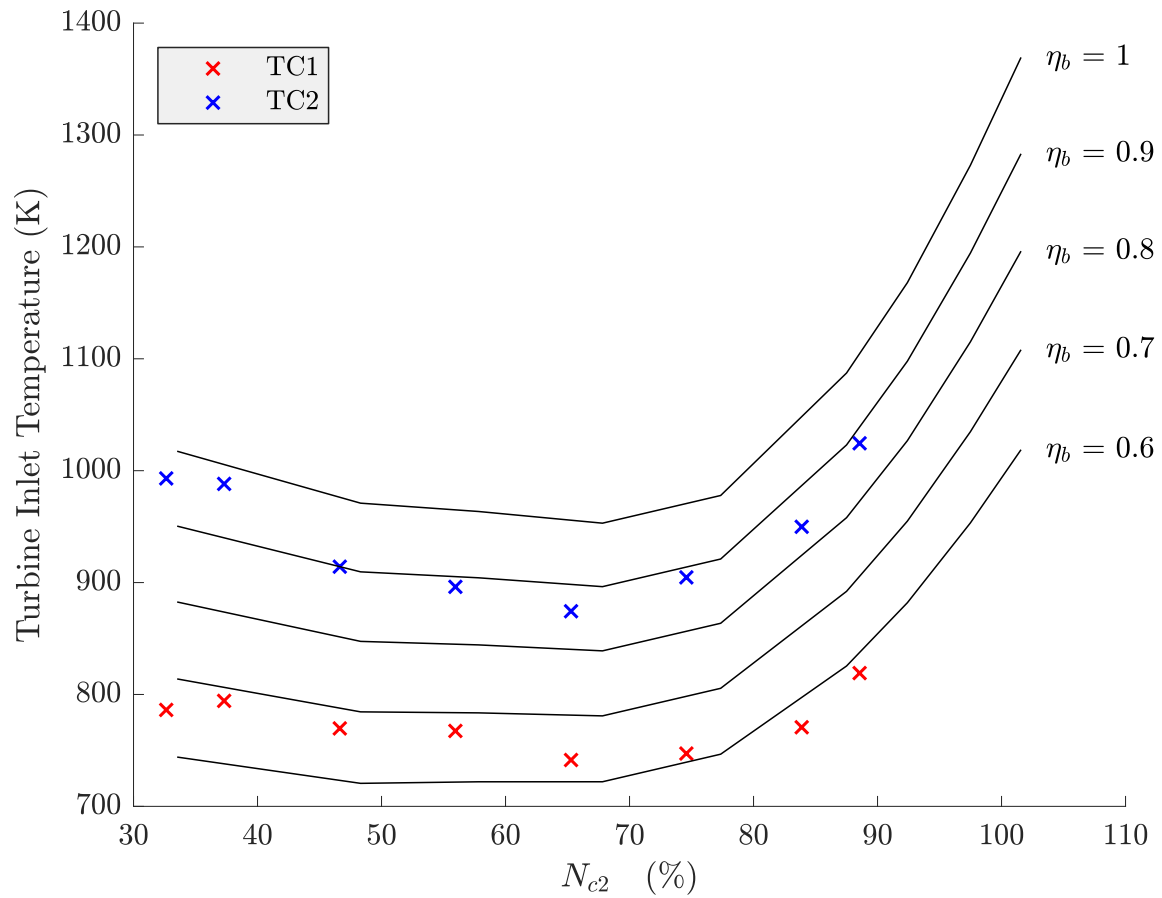


Figure 89. Turbine Inlet Temperature for Engine C measured over at two probe locations simultaneously.

4.2.3 Turbine.

As was the case for the combustor, distortions in the flow complicate experimental evaluations of the turbine. Using the method outlined in the previous section for determining the turbine inlet temperature, a turbine operating line was created for each engine. These operating lines are compared in Figure 90. When flow through a passageway reaches Mach 1, the flow is said to be choked. One characteristic of choked flow is that corrected mass flow rate becomes constant. Knowing that both the NGV geometry and the corrected mass flow rate through this station are constant constrains engine performance by determining the mass flowrate through the engine. In Figure 76 of Section 4.1, it was determined that specific thrust was fairly constant between engines and that mass air flow rate varied significantly and was the principle driver in determining thrust. This motivates further investigation into determining the factors that affect mass flow rate through these engines.

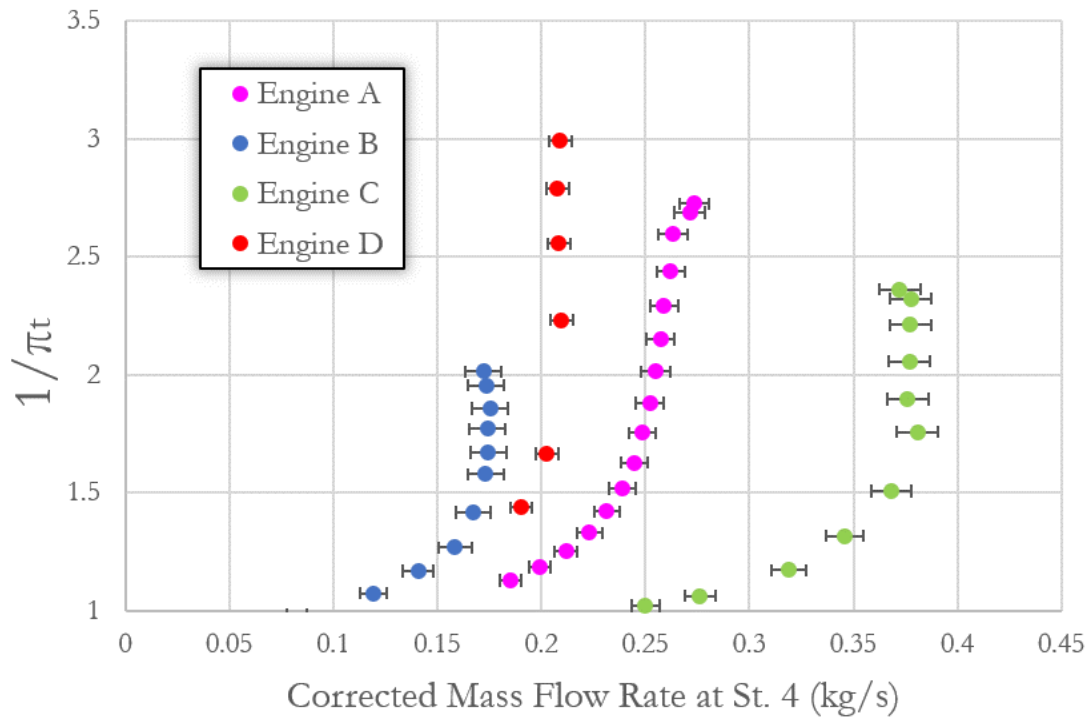


Figure 90. Turbine flow maps indicating choked nozzle guide vanes.

It is helpful to introduce the Mass Flow Parameter, MFP, at this stage of the analysis. MFP is defined by Equation 72 and can be written as a function of Mach Number and gas properties[24]:

$$\text{MFP} \equiv \frac{\dot{m}\sqrt{T_t}}{P_t A} \quad (72)$$

$$\text{MFP} = \sqrt{\frac{\gamma g_c}{R}} M \left(1 + \frac{\gamma - 1}{2} M^2 \right)^{(\gamma+1)/[2(\gamma-1)]} \quad (73)$$

since it is known from Figure 90 that $M = 1$, the MFP at the throat of each engine's NGV can be determined by assuming gas properties of the combustion products: $R = 0.290 \frac{\text{kJ}}{\text{kg-K}}$ and $\gamma = 1.3$. Recalling corrected mass flowrate to be defined as Equation 74:

$$\dot{m}_c \equiv \frac{\dot{m}\sqrt{T_t}}{P_t} \left(\frac{P_{ref}}{\sqrt{T_{ref}}} \right) \quad (74)$$

Equations 72 and 74 can be re-written to show that corrected mass flowrate varies linearly with throat area for choked flow. This relationship is given by Equation 75 and is illustrated by Figure 91.

$$\dot{m}_c = \text{MFP}(A) \left(\frac{P_{ref}}{\sqrt{T_{ref}}} \right) \quad (75)$$

MFP, P_{ref} , and T_{ref} are all constants. As shown by Figure 91, the corrected mass flow rate through the engine is fairly insensitive to gas properties and is primarily dependent on the turbine throat area. Therefore, the differences in corrected mass flow rate for the choked turbines shown in Figure 90 are due solely to differences in the NGV throat area. According to Equation 74, the relationship between true mass flow rate and corrected mass flow rate is a function of total temperature and total pressure. This allows the wide range of thrust performance to be traced back to three parameters: (1) NGV throat area, (2) compressor pressure ratio, and (3) combustor

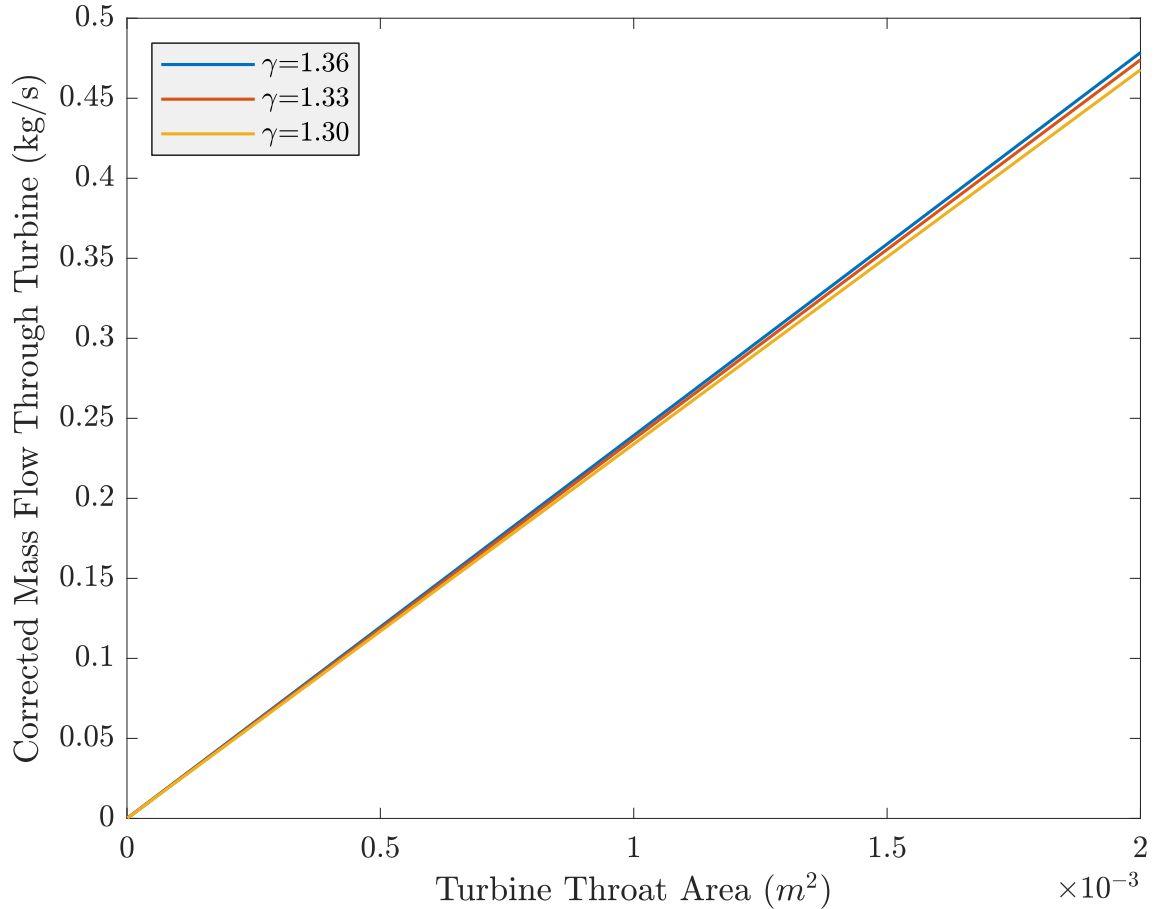


Figure 91. Relationship between corrected mass flow rate and choked turbine

temperature. Figure 92 illustrates how varying total pressure, total temperature, and NGV throat area affects mass flow rate through the engine. Three combustor exit total pressures are plotted, indicated by the three colors. Within the design space of a given exit pressure, six lines of constant total exit temperature are plotted. The top line for a given pressure represents a turbine inlet temperature of 1000K. The bottom line for a given pressure represents a turbine inlet temperature of 1500K. The lines in between mark 100K increments between the two extremes. The ranges of total temperature, total pressure, and corrected mass flow rate used for this design space were based on the ranges of data seen throughout the engines tested. The dashed vertical lines represent the corrected mass flow rate (and therefore effective turbine

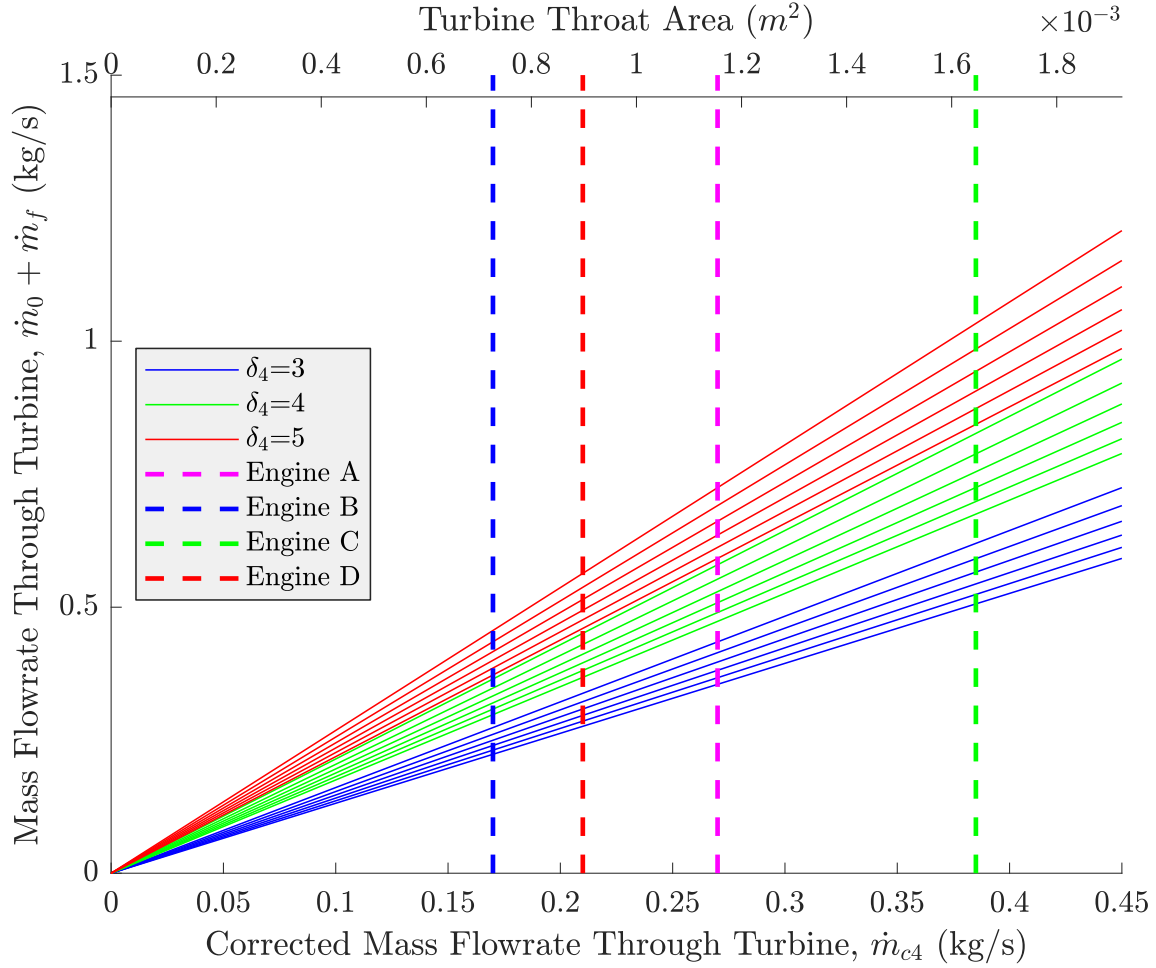


Figure 92. Relationship between mass flow rate and corrected mass flow rate for various turbine inlet total pressures and total temperatures.

throat area) during the choked condition. By changing temperature or pressure, one can move up or down a dashed line. By changing NGV geometry, one can move a dashed line horizontally.

Based on the engines tested, the highest mass air flow rate seen by any engine was 0.56 kg/s, seen by Engine B which was characterized by $\pi_c = 4$, $\dot{m}_0 = 0.56$ kg/s and a turbine inlet temperature of approximately 1200K. From Figure 90, it can be inferred that Engine C has the largest turbine throat area because it has the highest corrected mass flow rate and all engines have choked turbines. It was established by Figure 92 and Equation 74 that for a given \dot{m}_c , \dot{m} increases proportionally with the

total pressure at Station 4. Since Engine D and C have comparable turbine inlet temperatures, it can be inferred that by increasing the OPR of Engine C by 15% to the OPR measured in Engine D, the mass flowrate and therefore the thrust will increase by 15%. This would lead to an overall performance of 337 N of thrust with a mass flow rate of 0.64 kg/s. Now that the role of the combustor and NGV in engine sizing has been demonstrated, the discussion will transition to determining turbine efficiency.

Work extracted from the flow by the turbine is reintroduced to the flow upstream of the combustor via the compressor. The compressor is typically the more inefficient turbomachinery component since it works against a positive pressure gradient, while the turbine works with the pressure gradient. This typically leads to relatively high turbine efficiency values. For engines this size, values of $e_t \geq 0.80$ were anticipated. Fig 93 presents measured turbine polytropic efficiency values across the operating regime of each engine.

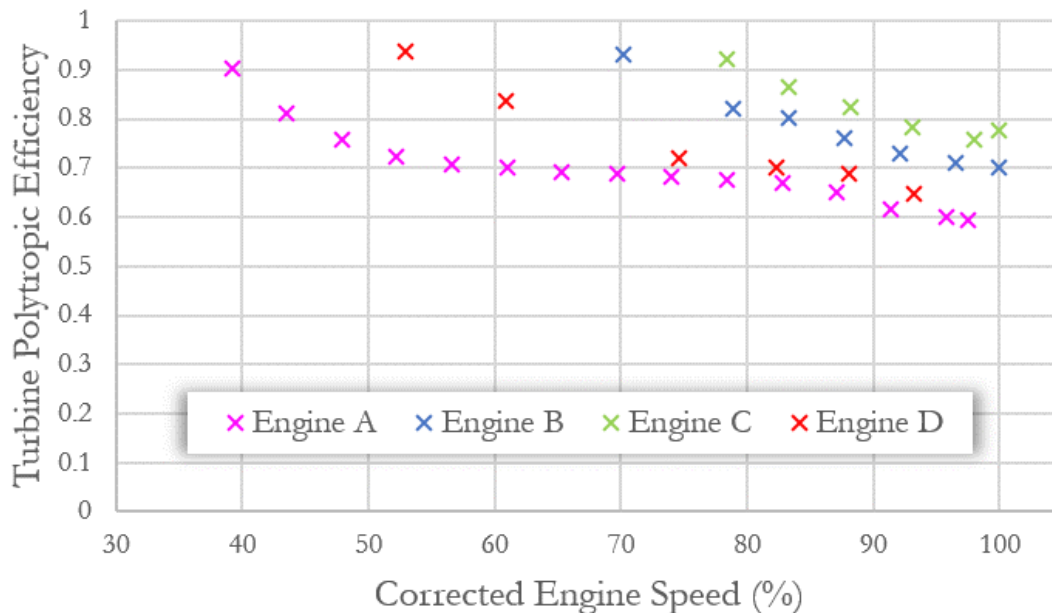


Figure 93. Turbine polytropic efficiency based on measurements of nozzle exit total pressure and temperature, fuel fraction, and the total pressure at Station 3.

The data in Figure 93 indicates much lower turbine efficiency than anticipated. It is believed that this is due to the non-uniformity of the flow at the turbine inlet and exit. For this analysis of turbine performance, the turbine inlet temperature was found using Equation 71 and empirically-derived tables to determine temperature based on enthalpy and fuel fraction. The turbine inlet pressure was assumed to be 90% of the compressor exit pressure. The turbine exit enthalpy was found by balancing compressor and turbine work, Equation 76 with an assumed mechanical efficiency of 98%. Finally, the total pressure at the turbine exit was determined to be 105% of the total pressure at the nozzle exit. Though the flow through the nozzle should be isentropic, the additional 5% was intended to account for viscous losses in the nozzle.

$$h_{t5} = h_{t4} - \frac{h_{t3} - h_{t2}}{\eta_m} \quad (76)$$

It was thought that the efficiency values calculated using this method were lower than expected due, once again, to the non-uniformity of the flow biasing the total pressure measurement at the nozzle exit. To alleviate this issue, an effective total pressure at the nozzle exit was calculated based on the specific thrust of the engine using the following equations:

$$F = (1 + f)\dot{m}_0 V_9 \quad \longrightarrow \quad V_9 = \left(\frac{1}{(1 + f)} \right) F / \dot{m}_0 \quad (77)$$

$$\dot{m}_9 = \rho_9 A_9 V_9 \quad \longrightarrow \quad \rho_9 = \frac{(1 + f)\dot{m}_0}{A_9 V_9} \quad (78)$$

$$P_{t9} = P_9 + \frac{1}{2}\rho_9 V_9^2 = \left(\frac{P_9}{P_0} \right) P_0 + \frac{1}{2} \left(\frac{(1 + f)\dot{m}_0}{A_9} \right) V_9 \quad (79)$$

$$P_{t5} = \frac{1}{\pi_n} P_{t9} \quad \longrightarrow \quad \boxed{P_{t5} = \frac{1}{\pi_n} \left[\left(\frac{P_9}{P_0} \right) P_0 + \frac{1}{2} \left(\frac{\dot{m}_0}{A_9} \right) \left(\frac{F}{\dot{m}_0} \right) \right]} \quad (80)$$

Equation 80 provides an effective total pressure at Station 5 based on the thrust and mass flowrate of the engine. For calculating the turbine efficiency, it was assumed that $P_9/P_0 = 1$. Through this analysis, the turbine polytropic efficiency at the design point was estimated to be 0.77, 0.74, 0.71, and 0.70 for engines A,B,C, and D, respectively. This method of turbine analysis produced efficiency values that were still lower than expected. Comparing these results to the results shown in Figure 93, no trend can be drawn between the two design point efficiency values, calling into question the accuracy of both methods. While the first method of determining turbine efficiency is troubled by flow non-uniformity, both methods require several assumptions to calculate a value. The uncertainty introduced by these assumptions compound and make it difficult to get accurate turbine efficiency measurements.

The results presented in this section provide a range of potential performance for the components found in commercial microturbine turbojets and highlight several gaps in experimental methodology for these engines. From the compressor analysis, it was determined that achievable OPR's ranged from 3.0 to 4.6 with compressor efficiency values between 65-80%. The diffuser was identified as a critical compressor component for determining efficiency and the need for more detailed diffuser experimentation was recognized for strong conclusions to be drawn regarding the efficiency decrement associated with an airfoil versus a wedge diffuser. The performance of the combustor and turbine proved to be more difficult to measure than the compressor. Turbine inlet temperatures were found to range between 1100-1500K, though the measurement techniques for this property were uncertain due to thermal distortions at the turbine inlet and uncertainty regarding combustion efficiency. The upper end of this range was much hotter than what was expected to be achievable for these engines, motivating further investigation into the effectiveness of the simple cooling methods employed. Finally, analysis of the turbine indicated that the flow was choked

for each engine. This is the first data collection that indicated choked flow for these engines, an expected result. It was recognized that the choking at the NGV throat controlled the mass flow rate through the engine and that an upper limit on mass flow rate for this class of engine could be predicted using this information.

This section has demonstrated the issues that arise when using a single point measurement to measure non-uniform flows. Future iterations of this work will require better techniques of resolve gas properties at the turbine inlet and exit. Ultimately, the goal of this research is to establish an understanding of the potential upper limit of performance for this class engine. The information presented in this section was used in Section 4.3 as the foundation for predicting the upper limit of modern commercial microturbine performance.

4.3 Performance Potential

In addition to experimentally testing commercial engines, this research also sought to determine the maximum performance achievable based on the components already in use in this class of engine. This upper limit on performance is referred to as the performance potential for the class of engine. Since the discussion has now shifted to predicting the upper performance limit of these engines, it is useful to introduce a military-grade engine at this point as a metric for comparison. The engine used for comparison is the Hamilton Sundstrand TJ-50, a turbojet of comparable size and thrust to Engine A but with an improved SFC. Performance claims of the HS TJ-50 are based on data published in Ref. [16]. This engine is a single shaft turbojet with a single-stage mixed flow compressor and single stage radial turbine. The shaft is cantilevered so that only one bearing is needed. That bearing is located towards the front of the engine, away from the hot combustion environment which typically reduces bearing performance. This engine claims a specific thrust of $664 \text{ N}/[\text{kg/s}]$

and a specific fuel consumption of 0.14 kg/[N-hr] [16]. It would be expected that the more expensive military-grade engine should exceed the upper performance limits of the commercial engines. That notion is tested in this section.

When designing an engine, it is common to employ a tool known as a carpet plot to identify how turbine inlet temperature and compressor pressure ratio affect the overall performance of the engine so that the target engine cycle can be identified. This tool requires engine properties such as component efficiencies and other losses to be known. This design tool can be used to compare the potential maximum performance of each of the four engines based on measured component efficiency. Since the carpet plot is dependent on engine efficiency, a unique carpet plot will be presented for each engine. The carpet plot for Engine A is presented in Figure 94. The star indicates measured engine performance and is plotted according to the measured specific thrust and specific fuel consumption. Based on these results, the OPR and TIT fall near expected values, reinforcing the accuracy and reliability of the carpet plot. Like the gold star, the *Mil.* marker indicates the specific thrust and specific fuel consumption of the military-grade TJ-50. Based on this carpet plot, in order for Engine A to achieve comparable performance to the military-grade engine, it would require an OPR of 7 and a TIT of 1400. Based on the data collected on commercial engines, the TIT is achievable, but a compressor pressure ratio in excess of 6 is not feasible for a single-stage, centrifugal compressor of this size.

Generating a carpet plot based on the performance of the other engines allows for similar analysis of each engine. The most notable carpet plot is that of Engine B, shown in Figure 95. Based on the low turbomachinery efficiency measured for this engine, military-grade performance is well outside the bounds of potential for this engine. OPR and TIT would need to be pushed well beyond the limitations of current technology in order to achieve similar performance to the HS TJ-50.

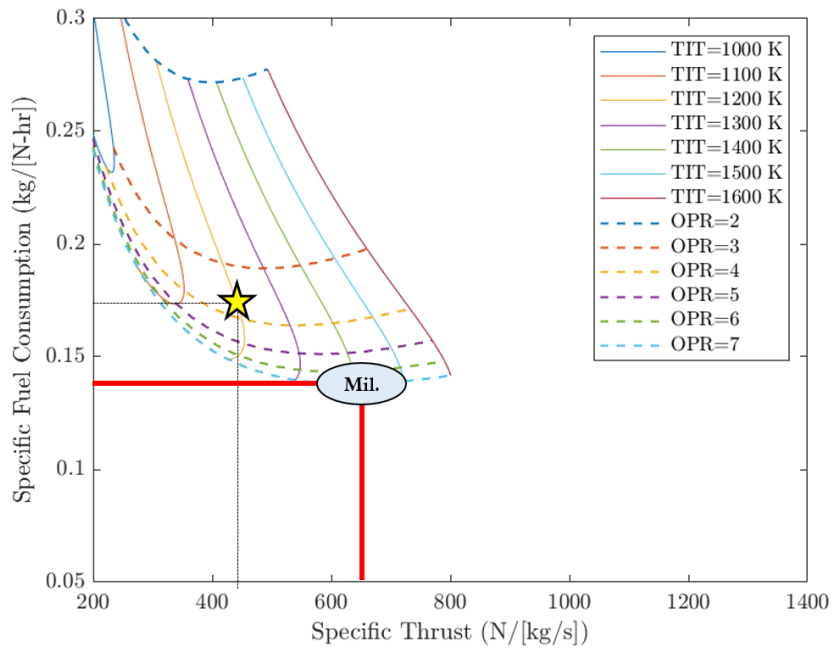


Figure 94. Carpet Plot of Engine A annotated with Military Performance Specifications.

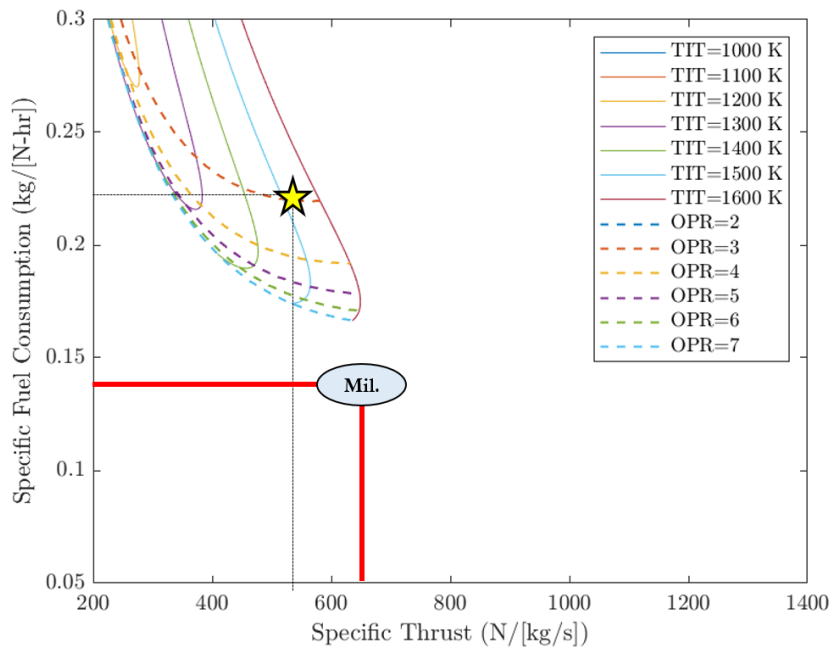


Figure 95. Carpet Plot of Engine B annotated with Military Performance Specifications.

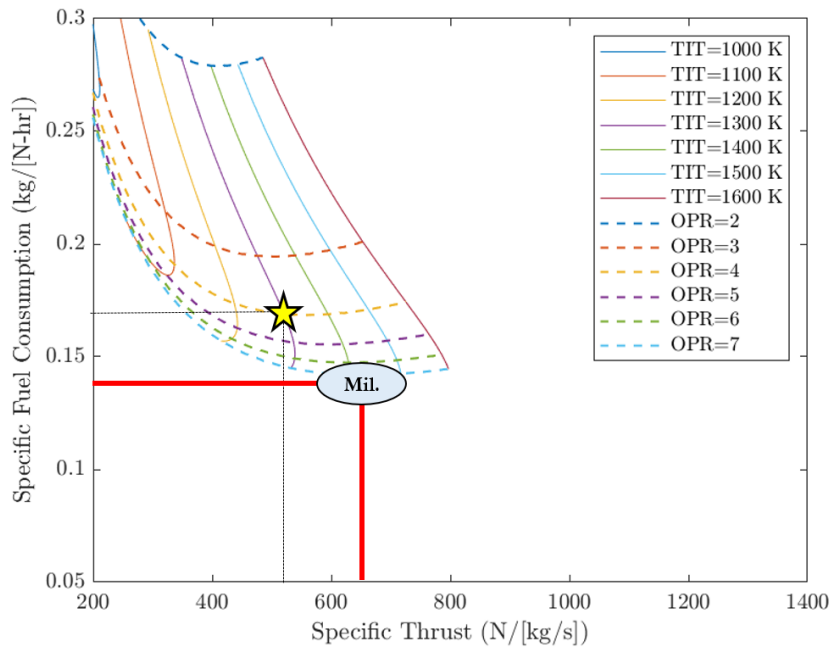


Figure 96. Carpet Plot of Engine C annotated with Military Performance Specifications.

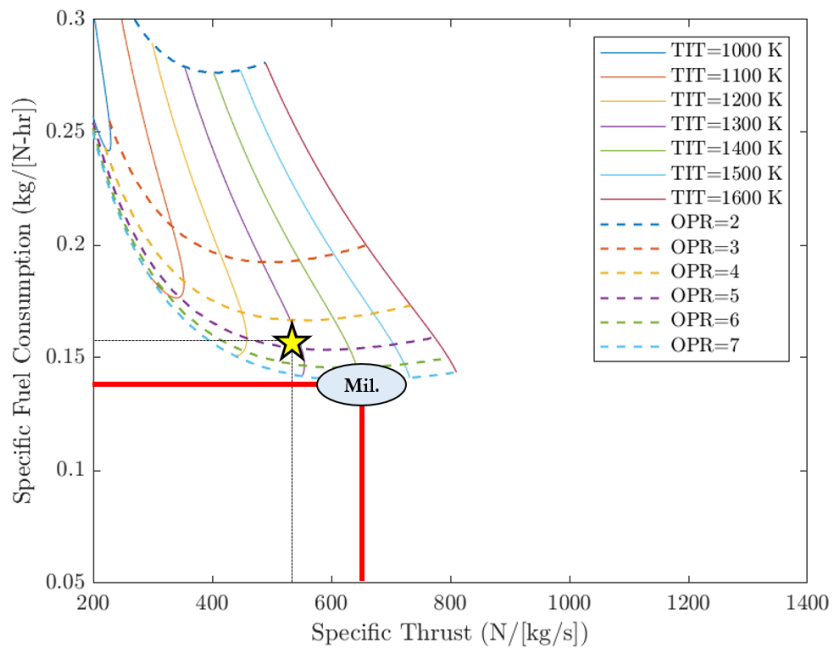


Figure 97. Carpet Plot of Engine D annotated with Military Performance Specifications.

The carpet plots of Engines C and D are shown in Figures 96 and 97. Based on Figures 94 and 96, it is easily visualized that Engines A and C have similarly component efficiency values (thus, similar carpet plot shapes), but they operate at different design points for TIT and OPR. The higher OPR is part of the reason why Engine C is able to process a higher mass air flow rate and produce more thrust. Considering Figure 97 it is seen that Engine D is the most efficient Engine because it has the lowest and further right carpet plot. Additionally, it became apparent that the military-grade performance may not be achievable by commercial engines because the commercial compressors were not able to produce the OPR of 6-7 that would be required to meet the SFC of the TJ-50.

Reviewing the performance of the commercial and military-grade engines, some notable conclusions can be drawn. A summary of engine performance is presented in Figure 98. First, it should be noted that the engines with the lowest specific fuel consumption were both reverse-flow engines. These engines had the highest OPRs which, as demonstrated by the carpet plots, reduces specific fuel consumption. Because of the architecture, these engines further reduce SFC by not wasting fuel for bearing lubrication. The military-grade engine has a specific thrust that is 23% higher than that of any commercial engine tested. The lowest commercial SFC was 0.148 with little room for improvement, while the military grade engine touted a published SFC of 0.14, a 7% improvement over the commercial engines.

Using the best efficiency values measured in any engine, a carpet plot can be generated that describes the design space for the maximum potential performance for a commercial turbojet, shown in Figure 99. The two 'x' marks on the carpet plot represent potential performance based on the best OPR and TIT measured in the commercial engines. Both 'x' marks are along the same line of an OPR of 4.6, but they are at different turbine inlet temperatures. The green 'x' indicates the performance

that would be possible if a TIT of 1200K was employed. The red ‘x’ indicates the performance that would be achieved if a TIT of 1500K was employed. While a TIT of 1500K seems higher than realistic for an uncooled turbine, the data was not dismissed because both thermocouple data and temperature predictions using Equation 71 indicated that the engine is operating at this TIT. Performance at both temperatures is shown due to the concerns regarding the engine life of a microturbine burning near 1500K. Regardless of the TIT selected, the maximum SFC for a commercial turbojet seems to be near 0.15 kg/[N-hr], similar to the performance achieved by Engine D.



Engine ID		A	B	C	D	H.S. TJ-50
Architecture		Standard TJ	Standard TJ	Standard TJ	Reverse Flow Std. Shaft	Reverse Flow Cantilever Shaft
F	N	200 ± 12	172 ± 10	293 ± 3	220 ± 12	253
\dot{m}_0	kg/s	0.423 ± 0.018	0.337 ± 0.015	0.555 ± 0.025	0.389 ± 0.018	0.381
F/\dot{m}_0	N/[kg/s]	473 ± 32	484 ± 32	530 ± 21	539 ± 38	664
\dot{m}_f	gpm	579 ± 20	699 ± 23	866 ± 24	559 ± 18	586
f	$\frac{\text{kg-fuel}}{\text{kg-air}}$	0.023	0.035	0.026	0.024	0.026
SFC	kg/[N-hr]	0.17	0.24	0.18	0.15	0.14
T/W		8.13	9.7	8.3	6.7	5.3
Compressor		<u>Centrifugal</u>	<u>Centrifugal</u>	<u>Centrifugal</u>	<u>Centrifugal</u>	<u>Mixed Flow</u>
		OPR = 3.6 $e_c = 0.75$	OPR = 3.0 $e_c = 0.65$	OPR = 4.0 $e_c = 0.78$	OPR = 4.6 $e_c = 0.80$	OPR = 5.2 $e_c \sim 0.7 - 0.75$
Turbine		<u>Axial</u>	<u>Axial</u>	<u>Axial</u>	<u>Radial</u>	<u>Radial</u>
		PR = 0.45 $e_t = 0.77$	PR = 0.57 $e_t = 0.74$	PR = 0.45 $e_t = 0.71$	PR = 0.41 $e_t = 0.70$	PR = N/A $e_t \sim 0.80 - 0.85$
TIT	K	1210 ± 30	1525 ± 50	1310 ± 40	1300 ± 40	1366

Figure 98. Overall performance comparison between the commercially available engines of this research and the military-grade HS TJ-50. Highlighted component performance values were used for determining the performance potential for commercially available engines.

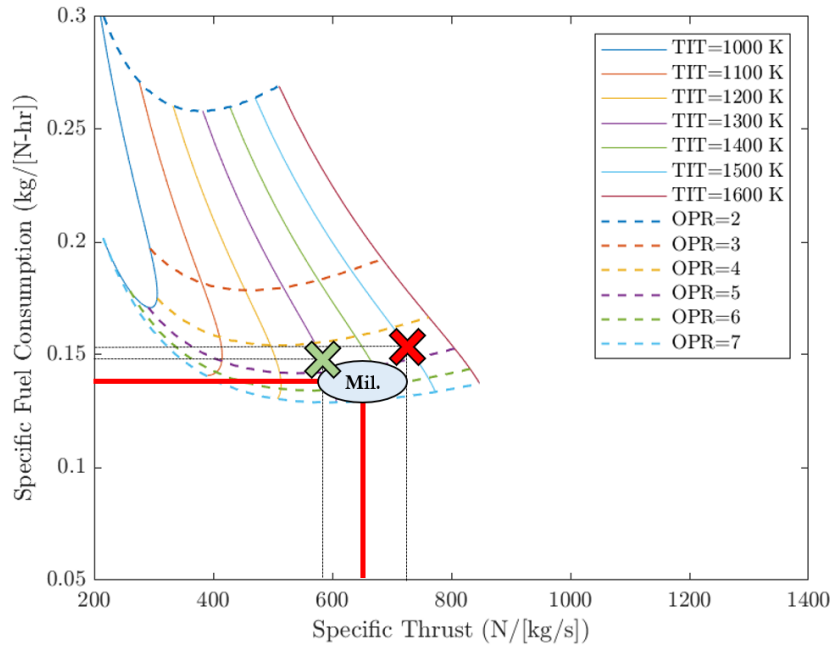


Figure 99. Carpet Plot of the potential performance of commercially available engines based on the best measured component performance of Engines A, B, C and D.

This is not surprising since Engine D produced an OPR of 4.6 and, according to Figure 99, SFC is relatively insensitive to TIT near the desired design point.

The distinction between Engine D and the predicted performance potential is found by considering the specific thrust of the engine. This theoretical engine has a higher specific thrust than the actual engines tested, near 600 rather than 450-550 N/[kg/s]. This, coupled with the potential maximum mass flow rate determined in Section 4.2.3, $\dot{m} = 0.65$ kg/s, suggests that a similarly sized engine could produce up to 390 N of thrust at an SFC of 0.15 kg/[N-hr].

However, carpet plot analysis revealed that comparable specific thrust was within range of achievable performance for a commercial engine. The defining performance metric was determined to be specific fuel consumption. It was found that the low specific fuel consumption of the military-grade engine would likely remain out of reach of the commercial engines based on the technology surveyed.

While it seems that military-grade fuel consumption rates are out of reach for these commercial engines, thrust performance of these engines could exceed that of the TJ-50. It should be noted now that sister engines of the TJ-50 have been made and a TJ-150, producing in excess of 660 N of thrust, has been produced with only slight increase in size from the TJ-50. The comparison of commercial engines to military-grade engines was not intended to be exhaustive. Rather, this comparison was intended to serve as a benchmark for the level of performance that is acceptable for military operations.

4.4 Effects of Instrumentation on Engine Performance

This supplemental research objective was motivated by the size of these engines and the ensuing concern that thermocouples and kiel tubes inserted into the engine would affect engine performance. Thrust and fuel consumption were used to quantify engine performance during these tests. A comparison of the plugged and the instrumented thrust results for Engine C is given in Figure 100. Plugged refers to an engine that has all the instruments removed and the tappings sealed off. The data presented

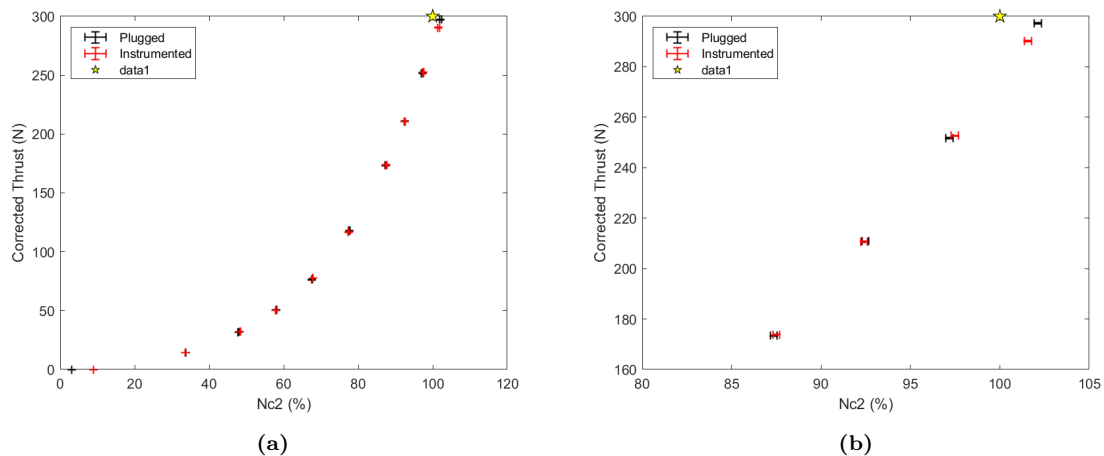


Figure 100. Effects of Instrumentation on Thrust: (a) Full Range of Operation, (b) Magnified View Near Design Point.

in Figure 100 shows that the engine performed similarly in both tests throughout the entire operating range. The plugged engine was able to reach a faster corrected speed than the instrumented engine, and consequently, was able to produce a higher maximum corrected thrust.

Comparing fuel flow rates yields a similar conclusion. As seen in Figure 101, the rate of fuel consumption for Engine C follows the same curve for both test cases. Again, the only difference occurred at the maximum engine speed, which was different for each test. The results presented in this section were sufficient evidence that the level of instrumentation used did not affect engine performance.

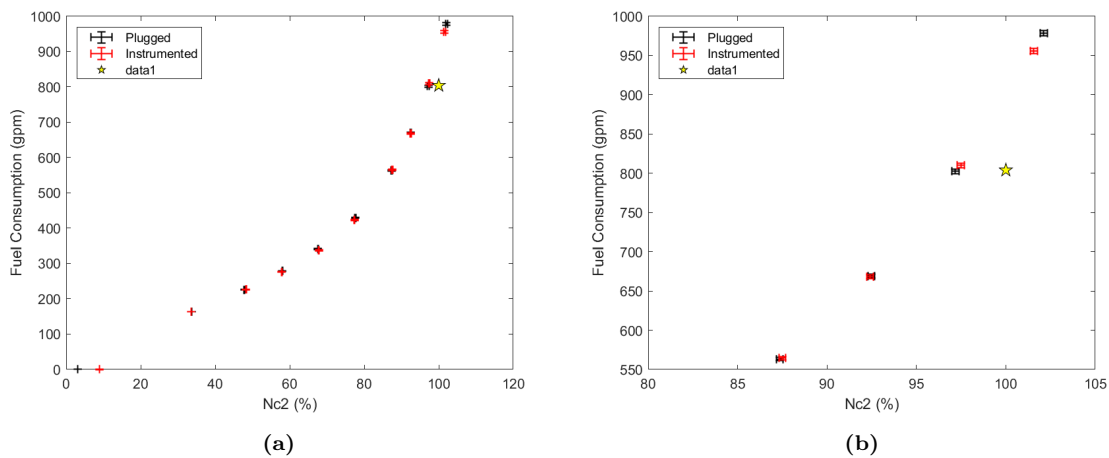


Figure 101. Effects of Instrumentation on Fuel Consumption: (a) Full Range of Operation, (b) Magnified View Near Design Point.

4.5 Same-Make, Same-Model Engine Performance Variability

Originally, when attempting to characterize the effects of instrumentation on engine performance, two separate engines of the same make and same model were used: one was instrumented, the other was not. The difference in performance between the two test cases was approximately 10%, so it was deemed that instrumentation did decrease engine performance. After isolating the test to a single engine as was done

in Section 4.4, it became apparent that the difference in performance was not due to the instrumentation but due to differences between the engines. Microturbines spin at speeds in excess of 100 kRPM. This corresponds to blade speeds in excess of 400 m/s. With such high velocities, differences in geometry due to manufacturing variations can have an impact on engine performance. Additionally, gas-turbine engines are sensitive to the balance of their turbomachinery. Each of the rotating components (shaft, compressor, and turbine) are balanced individually and also as an assembled unit. If this balance is off, it will cause gyroscopic forces that will increase bearing friction and can reduce engine performance. The objective for these tests was not to identify the sources of variation in performance between same-make, same-model engines. Rather, these tests were designed to indicate if variations in performance existed.

The original data used to determine the effects of instrumentation is presented in Figure 102. Engine B was used for this test. Core #1 was tested stock from the manufacturer. Core #2 was modified with instrumentation. Since the results presented in Section 4.4 indicated that instrumentation does not have an impact on engine performance, it is acceptable to compare the stock data from one engine to the instrumented data from a second engine. As seen in Figure 102a, engine performance begins to diverge as the engine accelerates past 70 % of the design speed. These tests were repeated, and both engines performed along their own unique thrust-speed curves. This indicated that each engine core did perform differently and that the unique performance of each engine was repeatable. As seen in Table 16, thrust performance at the maximum speed varied by over 8%. The results presented in Table 16 represent the mean data and do not consider measurement uncertainty.

While thrust measurements varied significantly between engines, the fuel consumption was nearly identical at each engine speed. This information reaffirms that

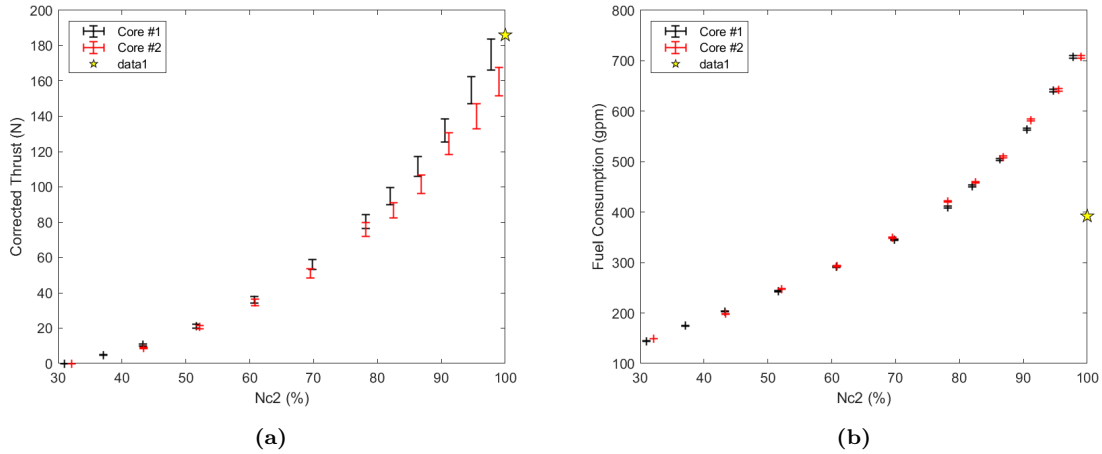


Figure 102. Performance variation in same-make, same-model engines (Engine B): (a) Corrected thrust, (b) Corrected fuel consumption.

the engines are performing differently. The variation in thrust cannot be attributed to differences in fuel flow. Comparing the specific fuel consumption for each engine again provides a clear contrast in performance. Figure 103 shows the specific fuel consumption over the full range of engine operation as well as a closer inspection of specific fuel consumption near the maximum speed. From these, it is clear that each engine performs differently throughout the entire range of operation. Again, consulting Table 16 shows nearly a 10% variation in performance between same-make,

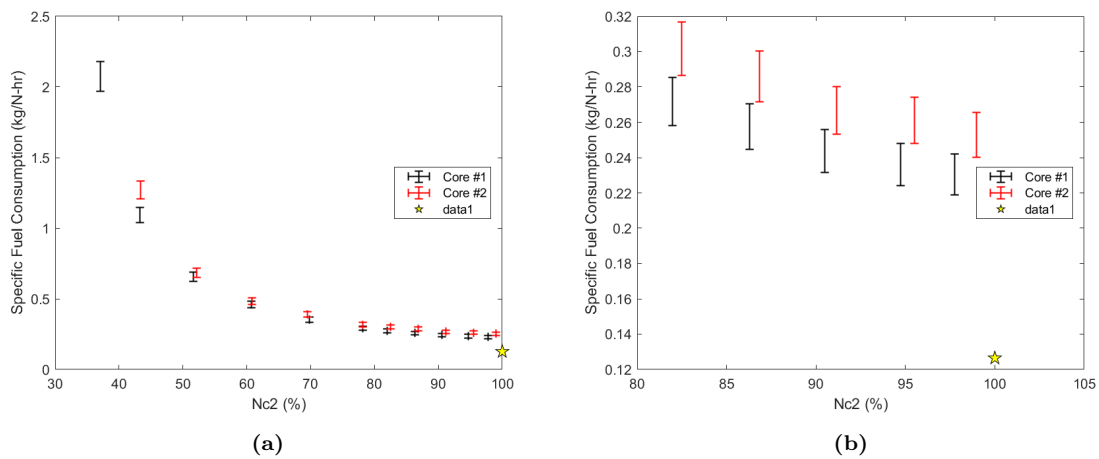


Figure 103. Performance Variation in Same-Make, Same-Model Engines: Specific Fuel Consumption: (a) Full Range of Operation, (b) Near Design Point.

Table 16. Performance comparison of same-make, same-model engines (Engine B).

	Core #1	Core #2	$\Delta\%$
F (N)	170	156	-8.42%
F _c (N)	175	160	-8.82%
\dot{m}_f (gpm)	667	665	-0.34%
\dot{m}_{fc2} (gpm)	708	708	+0.06%
S (kg/[N-hr])	0.235	0.256	+8.83%
S _c (kg/[N-hr])	0.231	0.253	+9.73%
N (kRPM)	113.5	114	N/A
N _{c2} (kRPM)	111.4	112.8	N/A

same-model engines. The manufacturer of Engine D qualifies their published thrust with uncertainty on a similar magnitude, indicating that this magnitude of variation is standard for within the industry.

The results shared in this section indicate that it is realistic to detect 10% variation in performance between microturbines of the same make and model. These performance variations can be attributed to variations in engine manufacturing and assembly. This information provides a potential estimate of the order of magnitude that can be expected for variations in performance for similar engines but cannot be used as more than a rule-of-thumb. In order to develop a more complete understanding of variations in engine performance, many engines of the same make and model would need to be tested to develop a useful statistical model.

V. Conclusions

The rapid growth of the UAV industry has developed a new class of commercially available microturbine turbojet engine. At an order of magnitude decrease in cost, these commercial engines provide a potential alternative to the expensive, special-order microturbine engines employed by the U.S. military. In order to determine the viability of using commercially available engines for military applications, four commercial turbojets were tested for overall and component-level performance. The results of these tests were compared against the Hamilton Sundstrand TJ-50 used to power the ADM-160 Miniature Air-Launched Decoy (MALD). Using this engine for comparison provided performance benchmarks (e.g. specific thrust, specific fuel consumption, T/W, etc.) for a comparably sized military-class turbojet. This comparison provided grounds for determining if the commercially available engines met the performance required for military applications.

In order to conduct the experiments necessary for this research, a thrust stand was needed. Research was conducted in AFRL's Small Engine Research Laboratory (SERL). This facility had a pre-existing thrust stand built for similar research. During testing, it was realized that one of the engines exceeded the thrust capacity of the pre-existing stand. This called for manufacture and installation of an entirely new thrust stand. The new thrust stand, which relied on rigid flexure supports instead of an air bearing system, had a higher thrust capacity and provided higher accuracy data. Time constraints prohibited retesting each engine, and only the largest engine was tested on the new stand.

5.1 Primary Research Objectives

The overall performance results presented in Section 4.1 indicated that none of the tested engines match the performance of the Hamilton Sundstrand TJ-50. In regard to most metrics, the military engine outperformed the commercially available engines tested. With respect to specific thrust, commercial engines produced 470-540 N/[kg/s] while the military-class engine was quoted at 664 N/[kg/s], 23% higher than the highest performing commercial engine. The lowest specific fuel consumption measured for a commercial engine was 7% higher than that of the military-class turbojet. Specific fuel consumption of the commercial engines tested ranged from 0.15-0.24 kg/[N-hr]. The H.S. TJ-50 claimed a specific fuel consumption of 0.14 kg/[N-hr]. Compared to the military-class engine, the commercial engines had comparable performance regarding thrust per frontal area (T/A). In terms of thrust to weight ratio (T/W), the commercially available engines outperformed the military-class engine touting. Thrust to weight ratios for the commercial engines ranged from $6.7 \leq T/W \leq 9.7$, while the H.S. TJ-50 had a published $T/W = 5.3$. This comparison requires some qualification. The Hamilton Sundstrand TJ-50 designated as the representative military-class engine has systems and capabilities that the commercial engines tested did not (i.e. high altitude starting). Although this skews the T/W metric, at a minimum, this comparison indicates that the commercial engines can almost double in weight in order to increase performance to meet military-performance benchmarks.

Results from the component-level testing were compared to the military-grade engine. These results are presented in Section 4.2. Overall pressure ratios of 3.0-4.6 were measured on the commercial engines. These measurements included the diffuser. It was noted that two styles of vaned diffuser were employed in these engines. Two engines utilized airfoil diffusers and two engines utilized wedge diffusers. It would

be beneficial for future work to isolate impeller and diffuser performance in order to establish a better understanding of each component. The military-class engine had a higher OPR of 5.2 which facilitates a higher specific thrust and specific fuel consumption than the commercial engines. This high OPR is achieved through a specially designed mixed flow compressor. The commercial engines rely on simpler centrifugal compressor impellers that are typically stock components from other contractors. This is a design trade-off made to reduce cost.

The results from component-level performance testing were used to determine the maximum potential performance of a commercially available engine, shown in Section 4.3. This analysis combined the highest performance metrics of each component into a single engine model and predicted performance. Since this study relied only on measured values, it provides a reliable estimate of the “best-case” performance that could be expected from modern commercially available turbojets. This analysis showed that without increasing OPR, commercially available engines will not be able to reach lower SFC values than that achieved by Engine D. However, by using maximum measured component efficiency values, specific thrust increased and by using the widest observed turbine throat area, the mass flow rate through the engine increased. It was shown that these changes would theoretically produce 390 N of thrust, a 30-38% increase, while maintaining a specific fuel consumption of just under 0.15 kg/[N-hr].

5.2 Supplemental Research Objectives

Microturbine engine evaluation is plagued by two significant limitations. The two supplemental research objectives were aimed to address these issues but were not intended to fully solve them. The first supplemental objective was to determine the effect of instrumentation on engine performance. This was motivated by a desire

to include more instruments to better resolve gas properties throughout the engine without altering engine performance. Gas turbine analysis commonly employs one dimensional models to predict performance. However, these engines are inherently three dimensional systems, and flow properties at a given axial location can vary significantly both circumferentially and radially. The small size of microturbines complicates engine instrumentation and makes it impractical to incorporate enough instruments to accurately resolve the thermal or pressure profile at a given engine station. To quantify the effects of internal thermocouples and Kiel tubes on engine performance, tests were conducted with and without instruments inserted into the engine. Variation in overall performance between instrumented and stock engine configurations was well below the measurement uncertainty of 5% of the thrust value. This provides incentive to include more internal instruments in the future in order to better resolve station thermal and pressure profiles.

The second supplemental objective was to determine the variation in performance between same-make, same-model engines. A 10% variation in performance was found between two engines of the same make and model. While two engines is not a large enough data set to develop a useful statistical model, this introduces a significant issue for the conclusions of this research. Adding 10% uncertainty on top of the measurement uncertainties of each result would make drawing certain conclusions difficult.

5.3 Future Work

First, instrumentation recommendations are made to facilitate better data collection in the future. The measurement techniques and instruments related to thrust, mass air flow and fuel flow rate were sufficient techniques and are recommended for future work. Methods for determining internal gas properties assumed one-dimensional

flow, but as shown in Chapter IV, significant variation occurred based on probe location between tests. Based on discussions with industry experts, it is common to employ up to four probes at a given axial location. This should be taken into consideration when developing future test configurations. Combination Kiel pressure-temperature probes are available at sizes useful for microturbines and may present a means of increasing the number of instruments in the engine without increasing the number of probes. Finally, combustor measurement techniques are still lacking. Increasing the number of thermocouples in the nozzle guide vane would improve the measurement, but the number of thermocouples required to fully resolve the properties at this station is prohibitively large. Infrared-based thermal imaging was attempted to resolve this issue, but calibration issues prevented this from being a useful technique for this work. Future work coupling data from thermocouples and IR-cameras may sufficiently resolve turbine thermal profiles.

Moving forward with microturbine aircraft engine research, several paths can be pursued. The first is to design an engine using commercially available components that achieves the theoretical performance potential predicted in Section 4.3. A first approach at this method can be conducted by widening the throat on the turbine nozzle guide vanes. This should increase mass air flow through the engine and increase thrust while maintaining the same specific fuel consumption. This would make the turbine choke closer to the max speed but would be a beneficial design trade-off for expendable turbojets intended to run primarily at maximum speed. This may not be a suitable design choice for vehicles not intending to spend the majority of the flight at full throttle.

To support longer range or loitering vehicles, a more detailed analysis of the compressor should be conducted. Incorporation of static pressure probes at the inlet and exit of the vaned diffuser should provide sufficient data to isolate diffuser per-

formance from compressor performance. This data would be useful in quantifying diffuser performance, especially total pressure loss. From this, more conclusive results can be reached regarding total pressure loss through different style diffusers: airfoil and wedge. Determining which diffuser style, airfoil or wedge, has the lowest total pressure loss would help guide future microturbine design. Such experiments would benefit from having compressor maps available for the impellers found in each engine. Development of a rig for creating compressor maps would be beneficial for future gas turbine studies at SERL. Such a rig should ensure that a common vaneless diffuser is used for testing each impeller to ensure that compressor maps are isolated from differences in diffuser design.

Finally, research regarding microturbine combustor and fuel distribution systems would be beneficial. After developing an adequate means of determining combustion efficiency and combustor exit thermal profile, better evaluation of combustor design should be conducted. Several design iterations of one engine from this study were inspected. The two significant differences in design were (1) the implementation of a new airfoil diffuser and (2) increase in the number of fuel distribution tubes. Determining sensitivity of pattern factor and other thermal distortion metrics to the number of fuel tubes would aid in improving engine life and increasing overall turbine inlet temperature. Additionally, quantification of the lubrication fuel used by standard-axial configurations would provide insight regarding the SFC benefits of employing the reverse-flow combustor which had no fuel lost to lubrication.

5.4 Concluding Remarks

The research presented in this document represents an ongoing effort by the Air Force Institute of Technology to support defense relevant research. The market for commercially available microturbine turbojets has developed in response to the rapidly growing unmanned aerial vehicles industry. The Air Force has the potential to leverage this market for cost-effective alternatives to special-order, military-grade turbojets used in UAVs and missiles. This research produced overall performance specifications for four commercially available engines in order to determine the capabilities of this class of engine. Component-level performance was evaluated in order to determine the potential overall performance that should be expected using technology currently employed in this class of engine. These results were compared to a comparable military-class engine. Based on the engines surveyed, the specific fuel consumption of the commercial engines was 7% higher than the military grade engine due to compressor limitations. Modern commercially available microturbine turbojets are capable of matching most military-grade engine performance metrics but not in the same design. Ultimately, the commercial microturbine engine market presents an excellent opportunity to drive down procurement costs, but seizing this opportunity will require prioritization of performance metrics and realistic assessment of mission needs.

Bibliography

1. ARIGA, I., KASAI, N., MASUDA, S., WATANABE, Y., AND WATANABE, I. The Effect of Inlet Distortion on the Performance Characteristics of a Centrifugal Compressor. *American Society of Mechanical Engineers 105* (1983), 223–230.
2. BALJE, O. *Turbomachines: A Guide to Design, Selection, and Theory*. John Wiley and Sons, New York, NY, 1981.
3. BASKHARONE, E. A. *Principles of Turbomachinery in Air-Breathing Engines*. Cambridge University Press, New York, NY, 2006.
4. BONHAM, C., BREND, M., SPENCER, A., TANIMIZU, K., AND WISE, D. Impact of Flow Unsteadiness on Steady-State Gas-Path Stagnation Temperature Measurements. *Journal of Engineering for Gas Turbines and Power 140* (2018), 122602:1–9.
5. BUSEMANN, A. Das Förderhöhenverhältnis radialer Kreiselpumpen mit logarithmisch-spiraligen Schaufeln. *ZAMM - Journal of Applied Mathematics and Mechanics / Zeitschrift für Angewandte Mathematik und Mechanik 8* (1928), 372–384.
6. CASEY, M. V., KRÄHENBÜHL, DANIEL, AND ZWYSSIG, CHRISTOF. The Design of Ultra-High-Speed Miniature Centrifugal Compressors. *Proceedings of the European Conference on Turbomachinery Fluid Dynamics and Thermodynamics ETC 10* (2013).
7. CHAURETTE, J. Pump Fundamentals. <https://www.pumpfundamentals.com/pump\glossary.htm>, 2019.

8. CORDIER, O. Ähnlichkeitsbedingungen für Strömungsmaschinen. *BWK Bd 6*, 10 (1953).
9. CROCKER, D. S., SMITH, C. E., AND MYERS, G. D. Gas Turbine Combustor Using Angled Dilution Jets. *In Proceedings of The American Society of Mechanical Engineers Turbo Expo: Power for Land, Sea, and Air 3* (1994), 94–GT–406.
10. CROWE, D. S., AND DEPAOLA, R. A. III. A Method to Compute Thermal Distortion in Non-Circular Ducts. *American Institute of Aeronautics and Astronautics* (2019), AIAA–2019–1449.
11. DEAN, R. *The Fluid Dynamic Design of Advanced Centrifugal Compressors: Lecture Notes*. Creare TN. Creare, Incorporated, 1974.
12. EPPLE, P., DURST, F., AND DELGADO, A. A Theoretical Derivation of the Cordier Diagram for Turbomachines. *Proceedings of the Institution of Mechanical Engineers, Part C: Journal of Mechanical Engineering Science* 225 (2011), 354 – 368.
13. GIERAS, M., AND STANKOWSKI, T. Computational Study of an Aerodynamic Flow Through a Micro-Turbine Engine Combustor. *The Journal of Power Technologies* 92 (2012), 68–79.
14. GOLDFEIN, D. L. *USAF’s Goldfein on Interoperability, Air Power, Multi-Domain Operations*. Defense and Aerospace Report, Interview at Dubai International Air Chiefs Conference.
15. GRANNAN, N. D., MCCLEARN, M. J., LITKE, P. J., HOKE, J., AND SCHAUER, F. Trends in JetCAT Microturbojet-Compressor Efficiency. *In Proceedings of 55th American Institute of Aeronautics and Astronautics Aerospace Sciences Meeting*, January (2017), AIAA 2017–0552.

16. HARRIS, M. M., JONES, A. C., AND ALEXANDER, E. J. Miniature Turbojet Development At Hamilton Sundstrand: The TJ-50, TJ-120 and TJ-30 Turbojets. *2nd American Institute of Aeronautics and Astronautics "Unmanned Unlimited" Systems, Technologies, and Operations* (2003), AIAA 2003-6568.
17. JAPIKSE, D. *Centrifugal Compressor Design and Performance*. Concepts ETI, Inc., Wilder, VT, 1996.
18. JAPIKSE, D., AND BAINES, N. C. *Introduction to Turbomachinery*. Concepts ETI, Inc., Wilder, VT, 1994.
19. KIEL, G. Total-Head Meter With Small Sensitivity to Yaw. *National Advisory Committee for Aeronautics: Technical Memorandum 775* (1935).
20. KIM, S. Y., PARK, M., AND CHO, S. Performance Analysis of a 50kW Turbo-generator Gas Turbine Engine. *The American Society of Mechanical Engineers* (1998), 98-GT-209.
21. KRUGER, C. H., AND VINCETTI, W. G. *Physical Gas Dynamics, Second Edition*. Krieger Publishing Company, Malabar, FL, 1967.
22. LOGAN, E. J. *Turbomachinery: Basic Theory and Applications, Second Edition, Revised and Expanded*. Marcel Dekker, INC., New York, New York, 1993.
23. LOU, F., AND KEY, N. L. The Design Space for the Final-Stage Centrifugal Compressor in Aero Engines. *American Institute of Aeronautics and Astronautics SciTech 2019 Forum*, January (2019), AIAA-2019-0944.
24. MATTINGLY, J. D., AND BOYER, K. M. *Elements of Propulsion: Gas Turbines and Rockets, Second Edition*. 2016.

25. MATTINGLY, J. D., HEISER, W. M., BOYER, K. M., HAVEN, B. A., AND PRATT, D. T. *Aircraft Engine Design, Third Edition*. Reston, VA, 2016.
26. MICHAEL, H. Auxiliary Air Inlet Door and Duct Coupling For Jet Aircraft Air Inlet Ducts. *US Patent Office*. Patent No. 2788184; Filed Oct. 5th, 1953; Issued Apr. 9th, 1957.
27. MOFFAT, R. J. Describing the Uncertainties in Experimental Results. *Experimental Thermal and Fluid Science* (1988), 1:3–17.
28. MORAN, M. J., SHAPIRO, H. N., MUNSON, B. R., AND DEWITT, D. P. *Introduction to Thermal Systems Engineering: Thermodynamics, Fluid Mechanics, and Heat Transfer*. Hoboken, NJ, 2003.
29. NOORBAKHS, A., AND KIRSCH, P.M. Theoretical and Real Slip Factor in Centrifugal Pumps. *Von Karman Institute for Fluid Dynamics: Recent Progress in Pump Research 2*, December (1973), 135.
30. OMEGA ENGINEERING INC. Thermocouples. <https://www.omega.com/en-us/resources/thermocouples>, 2018.
31. OMEGA ENGINEERING INC. Thermocouple Response Time. <https://www.omega.com/en-us/resources/thermocouples-response-time>, 2019.
32. PAMPREEN, R. C. Small Turbomachinery Compressor and Fan Aerodynamics. *Journal of Engineering for Gas Turbines and Power* 95, 3 (1973), 251–256.
33. RODGERS, C. Efficiency of Centrifugal Compressor Impellers. *Advisory Group for Aerospace Research and Development* 282 (1980), 22:1–13.
34. RODGERS, C. The Performance of Centrifugal Compressor Channel Diffusers. *The American Society of Mechanical Engineers* (1982), 82–GT–10.

35. RODGERS, C. The Efficiencies of Single-Stage Centrifugal Compressors for Aircraft Applications. *In Proceedings of American Society of Mechanical Engineers 1991 International Gas Turbine and Aeroengine Congress and Exposition* (1991), 91–GT–077.
36. RODGERS, C. 25-5 Kwe Microturbine Design Aspects. *In Proceedings of American Society of Mechanical Engineers Turbo Expo 2000: Power for Land, Sea, and Air* (2000).
37. RUNYAN, R., RYND, J. JR., AND SEELY, J. Thrust Stand Design Principles. *American Institute of Aeronautics and Astronautics 17th Aerospace Ground Testing Conference* (1992), AIAA–92–3976.
38. SOCIETY OF AUTOMOTIVE ENGINEERS. ARD50015: Methods to Compute Thermal Distortion. *Society of Automotive Engineers Standards* (1991).
39. SOROKES, J. M. Selecting a Centrifugal Compressor. *American Institute of Chemical Engineers: Chemical Engineering Progress* 109, 6 (2013), 44–51.
40. SPARROW, E. Error Estimates in Temperature Measurement. *In Measurement Techniques in Heat Transfer*. 1970, pp. 1–32.
41. TURNS, S. R. *An Introduction to Combustion Concepts and Applications, Third Edition*. McGraw Hill Education, 2012.
42. US DEPARTMENT OF ENERGY. Combined Heat and Power Technology Fact Sheet Series: Microturbines.
43. VAN DEN BRAEMBUSSCHE, R. A. Micro Gas Turbines—A Short Survey of Design Problems. *Micro Gas Turbines - Educational Notes RTO-EN-AVT-131, Paper 1* (2005), 1–18.

44. WALSH, P. P., AND FLETCHER, P. *Gas Turbine Performance*. Blackwell Science Ltd and American Society of Mechanical Engineers, 1998.
45. WARSHAW, K. Microturbine Propulsion for UAVs. *Society of Automotive Engineers Tech Briefs: Aerospace and Defense Technology* (2019), 16–17.
46. WHITFIELD, A. Slip Factor of a Centrifugal Compressor and Its Variation With Flow Rate. *Proceedings of the Institute of Mechanical Engineers* 188, 8 (1974), 415–421.
47. WIESNER, F. J. A Review of Slip Factors for Centrifugal Impellers. *American Society of Mechanical Engineers: Journal of Engineering for Power* 89, 4 (10 1967), 558–566.
48. WILLIAMSON, R. C., AND STANFORTH, C. M. Measurement of Jet Engine Combustion Temperature by the Use of Thermocouples and Gas Analysis. *SAE Technical Paper Series 1* (2010), 1598–1616.
49. YADAV, R., AND MISRA, S. Evaluation of Slip Factor of Centrifugal Impellers. *Institution of Engineers(India), Journal, Mechanical Engineering Division* 53 (1973), 203–210.

REPORT DOCUMENTATION PAGE

Form Approved
OMB No. 0704-0188

The public reporting burden for this collection of information is estimated to average 1 hour per response, including the time for reviewing instructions, searching existing data sources, gathering and maintaining the data needed, and completing and reviewing the collection of information. Send comments regarding this burden estimate or any other aspect of this collection of information, including suggestions for reducing the burden, to Department of Defense, Washington Headquarters Services, Directorate for Information Operations and Reports (0704-0188), 1215 Jefferson Davis Highway, Suite 1204, Arlington, VA 22202-4302. Respondents should be aware that notwithstanding any other provision of law, no person shall be subject to any penalty for failing to comply with a collection of information if it does not display a currently valid OMB control number.
PLEASE DO NOT RETURN YOUR FORM TO THE ABOVE ADDRESS.

1. REPORT DATE (DD-MM-YYYY) 26-03-2020	2. REPORT TYPE Master's Thesis	3. DATES COVERED (From - To) July 2018 - March 2020
--	--	---

4. TITLE AND SUBTITLE Microturbine Turbojets: Experimental Evaluation of Commercially Available Engines	5a. CONTRACT NUMBER
	5b. GRANT NUMBER
	5c. PROGRAM ELEMENT NUMBER

6. AUTHOR(S) DePaola, Richard A. III, 2d Lt	5d. PROJECT NUMBER
	5e. TASK NUMBER
	5f. WORK UNIT NUMBER

7. PERFORMING ORGANIZATION NAME(S) AND ADDRESS(ES) Air Force Institute of Technology Graduate School of Engineering and Management (AFIT/EN) 2950 Hobson Way Wright-Patterson AFB OH 45433-7765	8. PERFORMING ORGANIZATION REPORT NUMBER AFIT-ENY-MS-20-M-259
--	---

9. SPONSORING/MONITORING AGENCY NAME(S) AND ADDRESS(ES)	10. SPONSOR/MONITOR'S ACRONYM(S) AFRL/RQTC
	11. SPONSOR/MONITOR'S REPORT NUMBER(S)

12. DISTRIBUTION/AVAILABILITY STATEMENT
All information contained in this presentation is Distribution A. Approved for public release: Distribution Unlimited.

13. SUPPLEMENTARY NOTES

14. ABSTRACT
This research assessed the performance of commercial microturbine turbojets and was the first industry-wide investigation into this class of engine by AFRL's SERL. Four commercial engines of the same thrust class were evaluated for overall and component-level performance. In addition to providing an evaluation of existing systems, the maximum performance for a commercial turbojet was predicted based on component evaluations. This analysis indicated that a commercial turbojet could have comparable thrust performance to a similarly sized military-grade engine, but it is unlikely that commercial engines can achieve the SFC of military engines without upgrading the compressors found in commercial microturbines.

15. SUBJECT TERMS
(1) Small Gas Turbine Engines, (2) Commercial Microturbines, (3) Microturbines, (4) UAV Propulsion (5) Turbojet

16. SECURITY CLASSIFICATION OF:			17. LIMITATION OF ABSTRACT	18. NUMBER OF PAGES	19a. NAME OF RESPONSIBLE PERSON	
a. REPORT	b. ABSTRACT	c. THIS PAGE			Dr. Fred Schauer, AFIT/ENY	
U	U	U	UU	190	19b. TELEPHONE NUMBER (Include area code) (937) 255-6565, x4204 fschauer@afit.edu	

INSTRUCTIONS FOR COMPLETING SF 298

1. REPORT DATE. Full publication date, including day, month, if available. Must cite at least the year and be Year 2000 compliant, e.g. 30-06-1998; xx-06-1998; xx-xx-1998.

2. REPORT TYPE. State the type of report, such as final, technical, interim, memorandum, master's thesis, progress, quarterly, research, special, group study, etc.

3. DATE COVERED. Indicate the time during which the work was performed and the report was written, e.g., Jun 1997 - Jun 1998; 1-10 Jun 1996; May - Nov 1998; Nov 1998.

4. TITLE. Enter title and subtitle with volume number and part number, if applicable. On classified documents, enter the title classification in parentheses.

5a. CONTRACT NUMBER. Enter all contract numbers as they appear in the report, e.g. F33315-86-C-5169.

5b. GRANT NUMBER. Enter all grant numbers as they appear in the report. e.g. AFOSR-82-1234.

5c. PROGRAM ELEMENT NUMBER. Enter all program element numbers as they appear in the report, e.g. 61101A.

5e. TASK NUMBER. Enter all task numbers as they appear in the report, e.g. 05; RF0330201; T4112.

5f. WORK UNIT NUMBER. Enter all work unit numbers as they appear in the report, e.g. 001; AFAPL30480105.

6. AUTHOR(S). Enter name(s) of person(s) responsible for writing the report, performing the research, or credited with the content of the report. The form of entry is the last name, first name, middle initial, and additional qualifiers separated by commas, e.g. Smith, Richard, J, Jr.

7. PERFORMING ORGANIZATION NAME(S) AND ADDRESS(ES). Self-explanatory.

8. PERFORMING ORGANIZATION REPORT NUMBER. Enter all unique alphanumeric report numbers assigned by the performing organization, e.g. BRL-1234; AFWL-TR-85-4017-Vol-21-PT-2.

9. SPONSORING/MONITORING AGENCY NAME(S) AND ADDRESS(ES). Enter the name and address of the organization(s) financially responsible for and monitoring the work.

10. SPONSOR/MONITOR'S ACRONYM(S). Enter, if available, e.g. BRL, ARDEC, NADC.

11. SPONSOR/MONITOR'S REPORT NUMBER(S). Enter report number as assigned by the sponsoring/monitoring agency, if available, e.g. BRL-TR-829; -215.

12. DISTRIBUTION/AVAILABILITY STATEMENT. Use agency-mandated availability statements to indicate the public availability or distribution limitations of the report. If additional limitations/ restrictions or special markings are indicated, follow agency authorization procedures, e.g. RD/FRD, PROPIN, ITAR, etc. Include copyright information.

13. SUPPLEMENTARY NOTES. Enter information not included elsewhere such as: prepared in cooperation with; translation of; report supersedes; old edition number, etc.

14. ABSTRACT. A brief (approximately 200 words) factual summary of the most significant information.

15. SUBJECT TERMS. Key words or phrases identifying major concepts in the report.

16. SECURITY CLASSIFICATION. Enter security classification in accordance with security classification regulations, e.g. U, C, S, etc. If this form contains classified information, stamp classification level on the top and bottom of this page.

17. LIMITATION OF ABSTRACT. This block must be completed to assign a distribution limitation to the abstract. Enter UU (Unclassified Unlimited) or SAR (Same as Report). An entry in this block is necessary if the abstract is to be limited.